Experimental Investigation and Mechanistic Modelling of Dilute Bubbly Bulk Boiling

Von der Fakultät 4: Energie-, Verfahrens- und Biotechnik der Universität Stuttgart zur Erlangung der Würde eines Doktor-Ingenieurs (Dr.-Ing.) genehmigte Abhandlung

Vorgelegt von

Josip Kutnjak

aus Stuttgart

Hauptberichter: Prof. Dr.-Ing. habil. Eckart Laurien
Mitberichter: Prof. Dr.-Ing. habil. Klaus Spindler

Tag der mündlichen Prüfung: 27.06.2013

Institut für Kernenergetik und Energiesysteme der Universität Stuttgart

2013

Danksagung

An dieser Stelle möchte ich mich bedanken:

Herrn Prof. Laurien dafür, dass die Arbeit ermöglicht wurde und Ihr ein roter Faden gegeben wurde. Herrn Dr. Kulenovic für seine Anleitung und die Weiterentwicklung meiner schriftlichen Ausdrucksweise in Deutsch und Englisch. Allen Kollegen vom IKE für die angenehme kollegiale Atmosphäre und anregende Gespräche und natürlich auch die eine oder andere Feier. Den Kollegen aus der Werkstatt, Herrn Öztürk, Herrn Pein und Herrn Marques ohne die kein Prüfstand von mir betrieben worden wäre. Meinen beiden Studenten Herrn Singh und Frau Kern für Ihre Mitarbeit in meinen Forschungen. Meinem Freund und Mitbewohner Herrn Lapins dessen Leidenschaft mich immer wieder inspiriert hat. Außerdem allen anderen Freunden und Bekannten dafür, dass Sie mich ein bisschen zu dem gemacht haben, der ich heute bin.

Und insbesondere meiner Familie, meinen Eltern Steffi und Martin, meinem Bruder Anđelko und Anne für Ihre bedingungslose Unterstützung und Ihr Vertrauen in meine Fähigkeiten.

Herzlichen Dank allen.

Zusammenfassung

Bei Verdampfungsvorgängen ist die geometrische Gestalt des entstehenden Dampfs nicht durch die Thermodynamik beschrieben. Entstehende Dampfblasen sind zunächst sphärisch und verformen sich mit zunehmender Größe. Der Wärme- und Massentransport erfolgt über die Phasengrenzfläche. Die Interaktion von Kräften zwischen Dampfblasen und umgebender Flüssigkeit sind von Blasengröße und Form abhängig. Entsprechend ist es notwendig für eine vollständige thermofluiddynamische Beschreibung auch die Blasengestalt zu beschreiben. In dieser Arbeit ist das Verhalten der Blasenanzahldichte, also der Blasenanzahl bezogen auf das betrachtete Volumen, abseits von Heizflächen betrachtet worden. Es sind demzufolge Siedevorgänge innerhalb von gesättigten Flüssigkeitsvolumen betrachtet worden. Diese Fragestellung ist im Rahmen von nuklearen Sicherheitsbetrachtungen, wie dem Verlust der Kühlung im Brennelementlagerbecken wichtig zu beantworten.

Im Rahmen dieser Arbeit ist ein neuer Versuchsaufbau entstanden und untersucht worden. Der Versuchsaufbau besteht aus einem instrumentierten, hohen und schlanken Siedebehälter, dessen teilweise Transparenz der Beobachtung der Siedevorgänge dient. Die Beobachtung der Siedevorgänge dient der Identifikation von grundlegenden Wirkmechanismen und soll die Basis für ein neues Simulationsmodell bilden. Die Siedevorgänge sind mittels Videoaufnahmen aufgezeichnet worden und wurden anschließend mittels digitaler Bildbearbeitung ausgewertet. Die ermittelten Daten dienen der quantitativen Bewertung bei der Modellentwicklung und der Validierung.

Eine mechanistische Modellierung basiert auf der Ableitung von Wirkmechanismen aus einerseits der Beobachtung von Prozessen und andererseits aus der physikalischen Erklärung dieser. In diesem Zusammenhang wurden zwei wesentliche Mechanismen identifiziert; der Wachstums-/Schrumpf-Effekt der Dampfblasen und plötzliche Anstiege der Blasenanzahldichte. Der Wachstums-/Schrumpf-Effekt ist in Ansys CFX® durch die Berücksichtigung des Blaseninnendrucks mittels der Young-Laplace-Gleichung implementiert worden. Auf diese Weise besteht ein Wirkmechanismus, welcher die beobachtete Hysterese abbildet.

Die plötzlichen Anstiege der Blasenanzahldichte sind durch lokale Flüssigkeitsüberhitzungen erklärbar. Dabei ist eine lokale Überhitzung nur dann möglich, wenn der Wärme-/Massentransfer zwischen den Phasen langsamer erfolgt als die Reduktion der Sättigungstemperatur durch sinkenden hydrostatischen Druck bzw. wachsenden Blasendurchmesser. Durch die Überhitzung werden bis dahin nicht aktive Mikroblasen im Volumen aktiviert und es kommt zu einem schnellen Anstieg der Blasenanzahldichte. Dieser Effekt wird mittels einer algebraischen

Funktion realisiert, welche im Bereich der Sättigungstemperatur eine konstante Blasenanzahldichte besitzt und einen exponentiellen Anstieg der Blasenanzahldichte bei Überhitzung bewirkt.

Basierend auf der Modellierung einer lokalen und variablen Blasenanzahldichte wurden numerische Strömungssimulationen durchgeführt. Die Simulationsergebnisse zeigen, dass die Modellierung die genannten Mechanismen abbilden kann. Des weiteren sind die Modellparameter durch den Quervergleich mit den experimentell erfassten Daten bestimmt worden.

Abstract

During evaporation the geometric shape of the vapour is not described using thermodynamics. In bubbly flows the bubble shape is considered spheric with small diameters and changing into various shapes upon growth. The heat and mass transfer happens at the interfacial area. The forces acting on the bubbles depend on the bubble diameter and shape. In this work the prediction of the bubble diameter and/or bubble number density in bulk boiling was considered outside the vicinity of the heat input area. Thus the boiling effects that happened inside the nearly saturated bulk were under investigation. This situation is relevant for nuclear safety analysis concerning a stagnant coolant in the spent fuel pool.

In this research project a new experimental set-up to investigate was built. The experimental set-up consists of an instrumented, partly transparent, high and slender boiling container for visual observation. The direct visual observation of the boiling phenomena is necessary for the identification of basic mechanisms, which should be incorporated in the simulation model. The boiling process has been recorded by means of video images and subsequently was evaluated by digital image processing methods, and by that data concerning the characteristics of the boiling process were generated for the model development and validation.

Mechanistic modelling is based on the derivation of relevant mechanisms concluded from observation, which is in line with physical knowledge. In this context two mechanisms were identified; the growth/-shrink mechanism (GSM) of the vapour bubbles and sudden increases of the bubble number density. The GSM was implemented into the CFD-Code ANSYS-CFX using the CFX Expression Language (CEL) by calculation of the internal bubble pressure using the Young-Laplace-Equation. This way a hysteresis is realised as smaller bubbles have an increased internal pressure.

The sudden increases of the bubble number density are explainable by liquid super-heating. The liquid super-heating is only possible if the heat and mass transfer between the phases is slower than the saturation temperature reduction by hydrostatic pressure decreases along the height of the boiling container or due to bubble growth. By activation of the so far inactive micro-bubbles in the liquid bulk volume the bubble number density quickly increases. This effect is modelled by an algebraic function that uses a constant bubble number density in the vicinity of the saturation temperature and applies an exponentially increased bubble number density depending on the liquid super-heating.

Based on modelling a local and variable bubble number density numerical flow simulations were performed. The simulations showed that this approach is a suitable model to describe the

mechanisms found in the experiments. Model parameters were determined and verified by correlation with the experimental data.

Contents

“A life spent making mistakes is not only more honorable, but more useful than a life spent doing nothing.” - George Bernard Shaw

List of Figures

List of Tables

List of Symbols

	Latin Letters			**Greek Letters**
A	Area	α		Vapour/Phase fraction
a, b	Factors	Δ		Difference
A,B,C	Antoine equation constants	δ		Error
c_D	Drag coefficient	η		Dynamic viscosity
c_v	Heat capacity with constant volume	ϵ		Phase indicator
c_p	Heat capacity with constant pressure	Γ		Mass source/sink term
d	Diameter	ɣ		Surface tension
E,e	Energy	λ		Heat conductivity
E_{cc}	Eccentricity	ν		Kinematic viscosity
E_x	Expectation value	π		Pi
f	force/frequency	ρ		Density
G	Geysering event	σ		Standard deviation
g	Gravity	τ		Reynolds stress
h	Height/heat transfer coefficient	T	Θ	Temperature
J	Nucleation rate	ξ		Molecular volume
k_b	Boltzmann constant			
M	Momentum			**Indices**
m	Mass/scaling factor	b		Bubble
N	Count/Bubble number	BD		Becker/Döring (Authors)
n	Bubble number density	D		Drag
p	Pressure	dist		Distribution
P	Perimeter	e		Equilibrium
q	Heat flux	eq.		Equivalent
r	Radius	g		Gas
R	Roundness	HS		Hotspot
S	Superheat	ini		Initialisation
s	Distance	k		liquid/gas index
t	Time	l		Liquid
T	Temperature	loc		local
u,v,w	Velocities	m		Spatial directions
x,y,z	Coordinates	max		Maximum
Y(f)	Energy of frequency	mean		Mean value
		med		Median

	Indices (continued)
min	Minimum
n, n+1	Current, next timestep
norm.	normalised
ref	Reference
rel	Relativ
RM	Ranz/Marshall (Authors)
sat	Saturation
sau	Sauter diameter
sub	Sub-cooling
tot	total
w	Wall
width	Width
WL	Water level
ZS	Zeitoun/Shoukri (Authors)

	Dimensionless
Bo	Boiling number
Eo	Eotvos number
Ja	Jacob number
Pr	Prandtl number
Re	Reynolds number

1 Introduction

Phase changes are an omnipresent phenomenon widely used for extremely many applications. Cooking, weather forecast, energy conversion, processing techniques and many more examples show the relevance in every days life as well as in technical application.

The "VDI-Wärmeatlas" [1] (German Engineering Guidelines) is a standard in calculation of heat transfer problems. It describes boiling water inside a pot on a stove as the most important basic processing technique since the "invention" of fire. Especially in the case of high heat fluxes a satisfactory description is not possible, yet.

Water is one of the fluids that has been researched extensively and in thermal power plants water is a common liquid as it is easily available and its properties are well known and also advantageous. The most common working cycle using water and steam is the Clausius-Rankine-Process (see Fig. 1.1) [2]. It consists of an adiabatic and nearly isentropic compression of liquid water, followed by an isobaric heat input causing evaporation. Then the vapour is expanded adiabatically in the turbine and finally re-condensed at constant pressure. Evaporation and condensation are utilised and a lot of empiric knowledge is available to calculate the process cycle 1-dimensionally.

Inside a steam turbine the steam becomes sub-cooled in the last blade row and droplets are formed. These droplets do not follow the steam flow exactly but instead they collide with the blades causing serious abrasion [3]. Since this is a common and serious problem in turbine technology such condensation phenomena are under heavy investigation.

The evaporator uses a large surface to exchange the heat from a heat source. The larger the surface the lower the strain on the material, the smaller the surface the higher the impact on size and cost [5]. Despite this common application wall boiling is not well understood, yet.

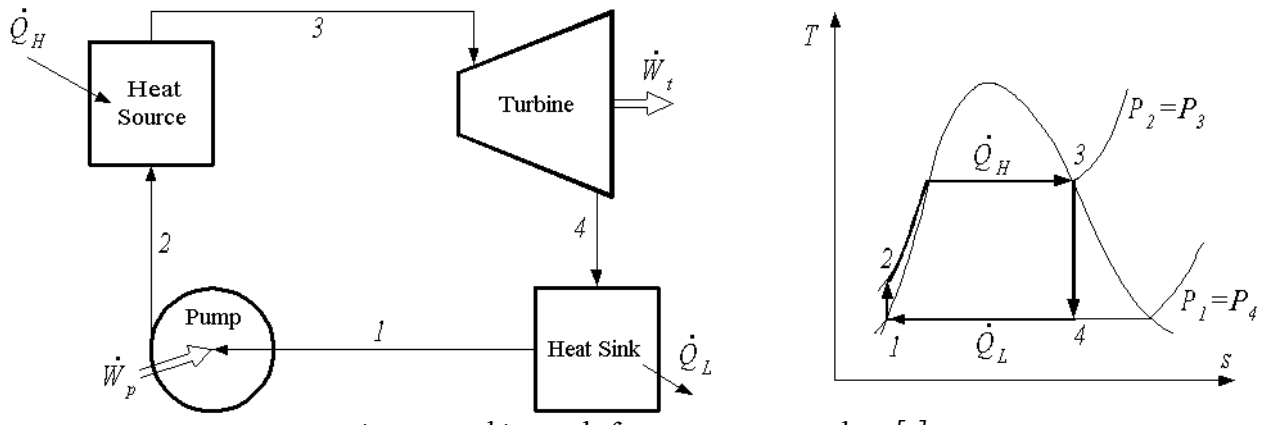

Fig. 1.1: Rankine cycle for a steam power plant [4]

Practicable models have been derived and are available for technical application. To avoid failure, a safety margin to the critical heat flux is a common safety analysis criterion [6]. When the critical heat flux is reached a burnout may happen and destroy the tubes. The critical heat flux depends on the flow structure and therefore better understanding of the flow is a promising approach to avoid failure whilst exploiting the materials capabilities and therefore keeping size and cost low.

A nuclear reactor core has very similar characteristics to the before mentioned evaporator in case of a boiling water type. Even in a pressurised water reactor local wall boiling occurs. In reactor cores the safety analysis needs to ensure undoubtedly that the fuel cladding has a safety margin to the critical heat flux. That is because the cladding are the second barrier that ensures the confinement of nuclear fission products [7].

Even though phase-changes are used extensively i.e. in energy conversion processes, the phase change mechanism is (or mechanisms are) not fully understood. By mechanism the general physical interactions during a process are first described descriptively. The accurate adaptation is done by model parameters is thus called mechanistic modelling. Several variations of boiling phenomena are of technical interest. The most commonly considered case is boiling at heated surfaces (wall boiling). The super-heating, where the temperature exceeds the saturation temperature locally, of the heated surface creates different types of boiling phenomena. The Nukiyama diagram (Fig. 1.2) shows the general impact on heat transfer at heated walls.

The phase change therefore is usually under constant pressure subjected to heat input. Some mechanistic models for this phenomenon exist and concentrate on the nucleation site density

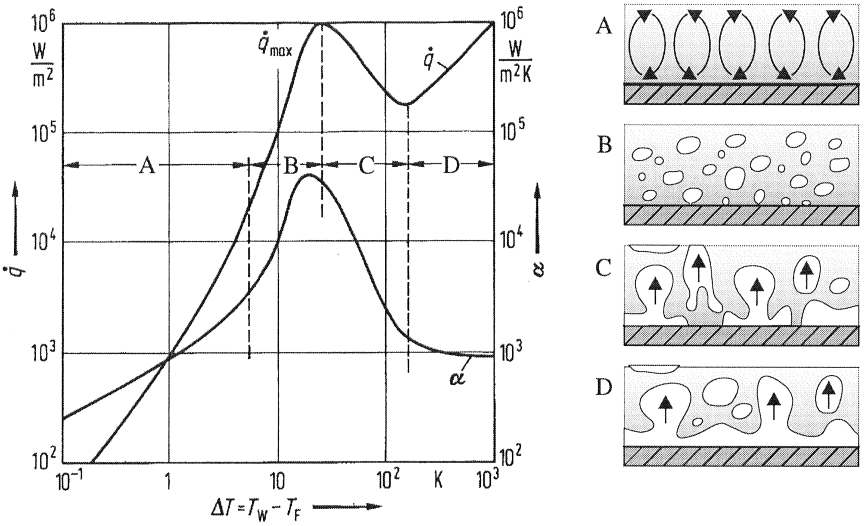

Fig. 1.2: Nukiyama diagram depicting the heat flux over the wall superheating and the corresponding boiling situations [8]

and a detachment frequency at a certain bubble size. The nucleation sites are usually fixed because of small gaseous inclusions in surface irregularities. These parameters can be measured for the surface [9][10]. As boiling is a highly unsteady process it can only be represented statistically. For example, Das and Kishor [11] describe a modelling technique to predict the heat transfer coefficient based on a fuzzy method. This way the prediction accuracy could be improved from ± 7 % to ± 0.5 %.

The precondition for boiling is an exceeded saturation that depends on the temperature and the pressure. Therefore another possibility to cause boiling is the reduction of the pressure below the saturation pressure, especially in pressurised systems. Compared to wall boiling the same questions may arise concerning the nucleation site density, but there is no measurable surface present. Several works concerning condensation have created experiments for establishing such a nucleation site density [12][13]. These are usually focussed on the physical term of the nucleus which is the first step towards a new phase. Extensive work was conducted in weather research [14].

Another aspect of concern to facilities may arise from phenomena like geysering. It is a two-phase instability originating from volumetrically evaporated liquid in high water columns. Geysering starts from the hotter portions of liquid being at the bottom of the column. The thermal layering is therefore unstable and natural, or forced, convection causes hot portions of water to convect upwards where super-heating causes evaporation that may oust the water column [15].

1.1 Motivation

Bulk boiling describes the evaporation of liquid inside the volume. Contrary to the expression pool boiling that is used for boiling processes at heated surfaces in water pools, bulk boiling shall denote boiling processes outside the vicinity of heated surfaces. Bulk boiling is of safety relevance but is not yet described satisfactory. Therefore the motivation is the development of an improved model for bulk boiling based on a mechanistic modelling that is derived from the physical phenomena observed in the newly built experimental set-up. The experimental set-up consists of a high water column with natural convection, which is comparable to i.e. a spent fuel pool. The fuel pool cooling system needs active components that are not available in case of a full station blackout As a full station blackout, so far, is a beyond design basis accident (BDBA) which has been out of the safety considerations of nuclear power plants. The accident in March 2011 caused by an earthquake and a tsunami in the Fukushima Daiichi nuclear power plant changed that mindset. A full station blackout is present if neither on-site nor off-site power is available for a

prolonged time period. The prediction of the boil-off behaviour and in this context the possibility of instabilities like geysering stemming from the evolution of the vapour fractions geometrical shape is of safety relevance. A nuclear spent fuel pool has a free surface and the water is contaminated to some extent. Therefore instabilities such as geysers need to be avoided, because even in early stages of a loss of cooling the contaminated water may be dispensed into the containment. This worsens the approachability for personnel to do repairs on the cooling system and is therefore of safety relevance. Another similar case is the loss of coolant during refuelling [16]. Here a pipe break happens after the plants shut-down inside the open reactor pressure vessel which quickly causes the remaining water inventory to boil.

As passive safety systems are favoured in future reactor types, natural convection as well as two-phase convection has become a focus of interest. A passive safety condenser consists of a large water pool in which a rod bundle is used to condense vapour from the primary circuit as it was investigated originally in the KERENA containment and is tested in the INKA facility [17]. The water pool is on the secondary side and there the water is heated at the rod bundle. In the beginning the water is at ambient temperature but the temperature keeps rising as the vapour is condensed. The density difference causes convection inside the pool, and in later stages two phase convection may be established. A work by Krepper et al [18] sought insight on the natural convection developing on the secondary side of a pool acting as temporary heat sink in case of a station blackout. The work focused on the single-phase convection established in the pool.

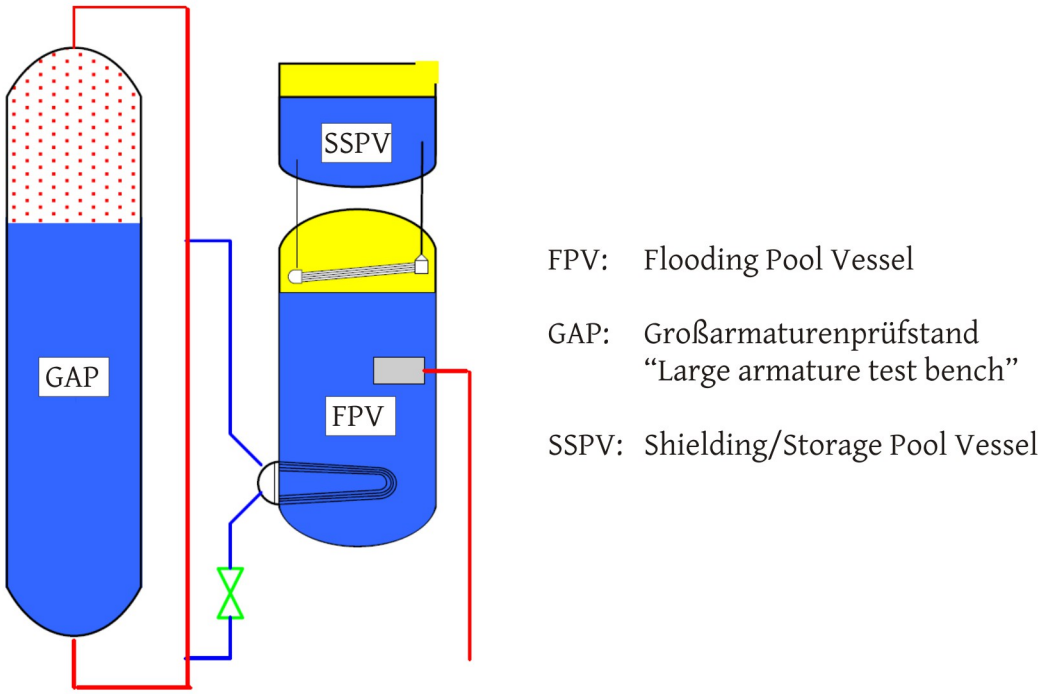

Fig. 1.3: INKA full scale conponent testing of the passive KERENA emergency cooling systems [17]

However, the water becomes saturated after some time and local vapour generation at the heat exchanger rods will happen. Hence the convection regime changes into two-phase convection.

Other recent works concerning passive containment cooling systems consider the overall coolability of gravity driven systems. In such systems the system is at low pressures and the core is surrounded by boiling water. Whilst boiling instabilities inside a closed reactor pressure vessel may be of no concern the evaporated steam is injected into water pools in which the steam condensates. The effectiveness of such loops determine pressure inside the containment [19][20].

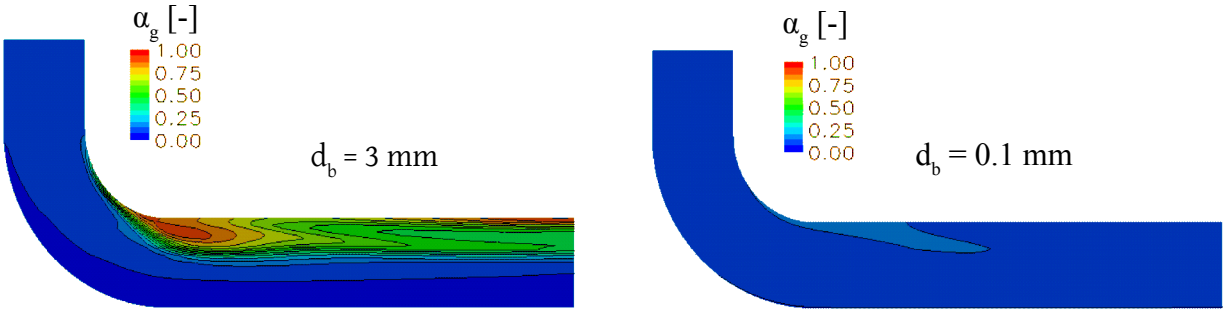

Fig. 1.4: Dependency of the calculated vapour fraction on the prescribed bubble diameter [21]

A preceding work by T. Giese [21] has investigated a drainage pipe from the upper reactor cavity of a German nuclear power plant (Neckarwestheim) that is connected to the cooling sump. During a Loss of Cooling Accident (LOCA) evaporated steam is condensed in the containment and the saturated water gathers in the upper reactor cavity. Obviously this contaminated water needs to be drained from there. The drainage pipes safety analysis, however, is based on a single phase flow estimation, but the water in the upper reactor cavity is supposed to be saturated, or at least close to being saturated. Caused by pressure losses as well as bends in the piping locally vapour pressure drops below saturation pressure. The creation of vapour causes blockage inside the piping. There is also the possibility of stratified layering and counter-current uprising of steam. All that may result in an insufficient flow rate that cannot drain the polluted water into the cooling sump. The results of computational fluid dynamics (CFD) calculations that were conducted during Gieses' work were dependent on user input, namely the imposed vapour bubble diameter (see Fig. 1.4). Depending on the bubble diameter all interactions between the phases are influenced. So the work by Giese demonstrates, that blockages caused by vapour generation need to be considered in the piping system. In this case, as well, the bubble diameter influences the result and needs further modelling.

All the previously mentioned phenomena (deep water pool, natural convection, bulk boiling) are bundled in the Generation III+ reactor design of the Economic Simplified Boiling Water Reactor (ESBWR) by GE Hitachi Nuclear. According to the manufacturer, this design is called

"Economic Simplified" because the number of active systems, namely pumps, is minimised. During operation of the 4500 MW_{th} reactor, the only active pump is the feed-water pump. In case of accidents for 72 hours no pumps are used at all.

In summary, bulk boiling is present when liquid becomes super-heated by decreasing pressure. This process can occur very fast and affect large portions of the liquid which is why it can greatly affect the flow, especially during instabilities. Compared to cavitation processes that are modelled by the Rayleigh-Plesset-model pool boiling is not dominated by the viscosity. Mixing processes as well as convection are consequences of vapour generation inside a volume and may effect the heat transfer mechanisms. Other relevant effects may be instabilities like geysering or flashing and piping blockage that may cause security/safety concerns for facilities. CFD calculations do have the potential to become an general safety analysis tool because the development aims for general application and therefore increases the safety of existing and future nuclear power plants.

1.1 State of the Art

This sub-chapter will first introduce a brief background concerning experimental techniques for two-phase flows and the phenomenon of initial phase changes (nucleation) as well as current simulation techniques for two-phase flows and relevant applications.

Two-phase measurement techniques

Fibre-optic void sensors can measure if, at the measuring point, liquid or gaseous fluid is present. This is achieved by the difference in refractive index between the gas phase and the liquid phase. The angle of reflection is larger in the liquid than it is in the gas phase. A glass fibre is cut with a certain angle and attached to a light source. Depending on the phase present at the tilted glass fibre cut, the light is reflected or not. Another type consists of a U-shape glass fibre that is conducting light. If gas is surrounding the strong bend the light will not reach the optical sensor. In a study of Chabot et al. [22] such sensors were used to measure the gas hold up, the bubble rise velocity, the bubble chord length and the bubble chord length distribution. In Chaumat et al. [23] it was shown that in industrial application the gas hold-up and bubble frequencies can be obtained with high certainty but problems with measuring the bubble velocity and diameter arise.

Another technique for two-phase measurements is to use the different electric conductivities of the liquid and the gas phase. This has first been realised using probes that use a rod and an electrically insulated surrounding sleeve. The probes tip would only conduct electricity when in contact with water, but not with vapour. Later from that technique the wire mesh sensor was

developed. It consists of crossed wires that only conduct when in contact with the liquid water phase. The crossing point are measured consecutively with a very high frequency which gives an instant distribution over the whole sensor. It is a intrusive technique but offers high resolution and high-frequency quasi-3D measurements. Prasser et al [24] have demonstrated that measurement of bubble sizes are feasible. After the technique was established a comparison with ultra-fast x-ray tomography [25] was performed. The mesh sensor delivers higher resolution but underestimates the gas fraction. Later Pietruske and Prasser [26] show that the sensor is capable to be used with high measuring frequency in environments that are subjected to high temperatures and pressures.

The ultra-fast x-ray tomography is currently being developed by Stürzel et al [27]. The goal is a high resolution 3D imaging with a image frequency of at least 1000 frames per second to measure two-phase flow whilst being totally non-intrusive. The basic idea is to steer an electron beam across a conical target surrounding the object to be scanned to create the x-ray beam. There are no moving parts which allows for very high frame rates. As the electron guns target is transparent for the induced x-rays a high resolution becomes possible as there is no axial offset between the focal spot path and the detector. Reconstruction artefacts are minimised because a full 360° detector ring is used. For static target measurements at 2000 frames per second the spatial resolution was found to be 1.2 mm or better.

Manera et al [28] compare a conductive needle probe to a wire-mesh sensor. The needle sensor and the wire mesh sensor showed good agreement. It is concluded that the wire mesh sensor offers more possibilities of full reconstruction of i.e. the inter-facial area density though it remains very intrusive. The needle probe however cannot detect all bubbles and is therefore not as valid for gathering statistical data.

A study on bubble creation at heated walls done by Gerardi et al [29] shows a combined measurement of the heated surface. The heated surface is a 0.7 μm layer of Indium-Tin-Oxide on a 0.4 mm thick sapphire substrate. The emerging bubbles are recorded using a high speed camera and additionally a high-speed infra-red camera. That way the bubble and the surface temperature can be observed simultaneously without intrusion. Hence time resolved data for the bubble radius, the micro-layer radius and the dry-out radius are measured and comply with former data and models. In their experiments it was established that the quench heat flux is a dominant contribution to the heat flux within their set-up.

Giese [21] measured in his work how thermal cavitation increases the pressure loss through a pipe with gravity driven flow. The work included CFD simulations using the Euler-Euler model to calculate the pressure loss through a pipe bend with cavitation. It was concluded that the

obligatory fixed description of the bubble diameter determinates the calculated pressure loss.

Many measurements involve non-invasive optical methods including object recognition and tracking methods. Rong investigated subcooled nucleate boiling in a vertical annular channel with an inserted heater rod using high speed video recordings [30]. The focus was on bubble departure frequencies and lift-off diameters, as well as bubble growth rates and velocities after lift-off. Another study has been conducted by Zaruba that used a rectangular water column of 1.5 m height [31]. At the center of the bottom of that column air was injected and the bubbles were observed using a high speed camera. The work shows recorded bubbles being identified by using the proper digital image processing and tracking. The velocity distributions of the dispersed phase were measured and the turbulent diffusion coefficients of the gaseous phase were calculated using the experimental results.

Another measurement technique is the use of a high frequency neutron radiography. Mishima et al [32] review the status of development and the application of a steady thermal neutron beam with high frame rate. The method is possible to be used with metal tubes and the void fraction may be integrated over the depth.

A video investigation of boiling was performed by Luke et al [33]. The investigation focuses on bubble formation and heat transfer on heated surfaces. The measurement technique is very similar to the one used later in this work. Automatic detection of the nucleation sites on a heated surface is combined with subsequent tracing of departing bubbles. This way statistical analysis of the nucleation sites position and activity is possible. The goal was to observe nucleation sites that are influenced mutually. It was detected that adjacent nucleation sites influence each other if they are active at the same time. The nucleation site densities vary greatly for the same boundary conditions. The model assumption of stable nucleation sites with constant frequency and departure diameter is therefore to be checked critically.

Maurus et al [34] have done an experimental investigation on nucleate boiling on a copper strip in a rectangular channel. Video processing is used in an automated way to measure a big number of cycles and the results are then given in a statistical way mostly by distribution functions. This way the information loss by spatial or temporal averaging is avoided. It seems unreasonable that boiling processes are of deterministic nature, which is why probabilities are a more suited way of description.

Guo et al [35] present a multi-scale edge detection based on a wavelet transform with a Gaussian filter. It is compared to a common canny detector algorithm [36]. It can be seen that the canny operator cannot distinguish between two bubbles being close to another and the detection of the

bubble shape is worse than with the wavelet analysis. It is suggested to be used for multiphase measurements.

A study concerning the frequency of flashing phenomena was conducted at the KA research centre (Forschungszentrum Karlsruhe) with a 6 m high water column being heated from the bottom [37]. The set-up was used with and without forced convection with different heating inputs and water levels. It was stated that there was a flashing frequency found, but below a water level of 2.5 m the mode changes to a different pattern.

Okawa [38] conducted a visual investigation of sub-cooled water flow boiling situation at low pressure and flow rate. The heated wall used is a hydrophobic surface. With high sub-cooling the evaporation and condensation rate was nearly equal which is why the void fraction stayed relatively constant. With lower sub-cooling the bubbles begin to slide along the walls an coalescence happens. Then a rapid increase in vapour fraction was observed. This point of net vapour generation (PNVG) is important to predict for accurate vapour fraction prediction. The triggering mechanism to this process is investigated. The mechanism consists of bubble coalescence forming larger sliding bubbles that incorporate smaller bubbles along the wall upon convecting upwards.

Nucleation and Phase Stability

The phenomenon that liquids can be heated beyond saturation temperature is well-known for a long time. The first general description for phase changes was given by Gibbs. Volmer and Weber [39] first defined the term nucleus clearly by picking up Gibbs works. Another common knowledge is the well known relation given by Thompson for the pressure inside a bubble being increased due to capillary forces. Volmer and Weber show that for a bubble in equilibrium an infinitesimally small work is required to destabilise this characteristic bubble. Therefore the work necessary to create that bubble is a measure for stability. To calculate this the change in Gibbs free energy can be used. The term critical nucleus is defined by a nucleus being in equilibrium with the super-heated system. The next question upon definition of a measure for stability is, how often due to natural thermal fluctuations a nucleus is created. For this means the collision theory is applied in the case of droplets forming in vapour. The work to form a critical nucleus is the activation energy. If it could be shown that a proportional number of nuclei grows to macroscopic size the theory would be analogue to the Arrhenius equation for chemical reactions. Unfortunately this proportionality is unknown in quantity and eligibility. Further it was shown that upon the existence of a wet-able wall the probability of homogeneous nucleation is extremely low. Another finding is that higher magnitudes of super-heating are impossible upon existence of substances that decrease surface tension. Based on Volmers definition for a nucleus

Farkas [40] investigated the before mentioned proportionality factor. It is assumed that consecutively molecules collide with the nucleus and some are incorporated into the nucleus. This causes a fluctuating nucleus size. Since attachment and detachment of single molecules in general are not equal the fluctuation has to obey a rule. A similarity to Brownian motion is stated. Becker and Döring [41] later published a paper that supported the classical nucleation theory by picking up Farkas work. The differential equations established by Farkas created new and partly unclear constants. Becker and Döring showed a complete algebraic description of the problem and calculated the proportionality using gas-kinetics. They considered an analogy to electrical resistance to illustrate their approach. Consequently the nucleation rate could be calculated using an algebraic formula based on thermodynamic properties.

Much of that knowledge was later published by M. Volmer [42]. Zeldovich [43] concluded the classical nucleation theory with the focus on cavitation of liquids. Contrary to the previous authors he considered vapour bubbles in liquid. Contrary to Becker and Döring, the velocity of nucleation is dominated by the viscosity of the fluid instead of the evaporation velocity as the subject was cavitation. Again it was stated that the creation and activation of nuclei are due to Brownian motion. Then Zeldovich stated that nucleation itself is of no interest. What is of interest is the creation of a macroscopical new phase that actually changes the surrounding's temperature. To the point of nucleation the consideration is a canonical ensemble and hence not changing the old phases temperature. A recent extension is given by ter Horst, Bedeaux and Kjelstrup [44].

In his book Metastable Liquids [45] Skripov concentrated on one-component systems and on evaporation. Besides consideration of the nucleation theory the interesting concept of the spinodal derived from the Van der Waals equation was presented. In the two-phase area of a p-v-

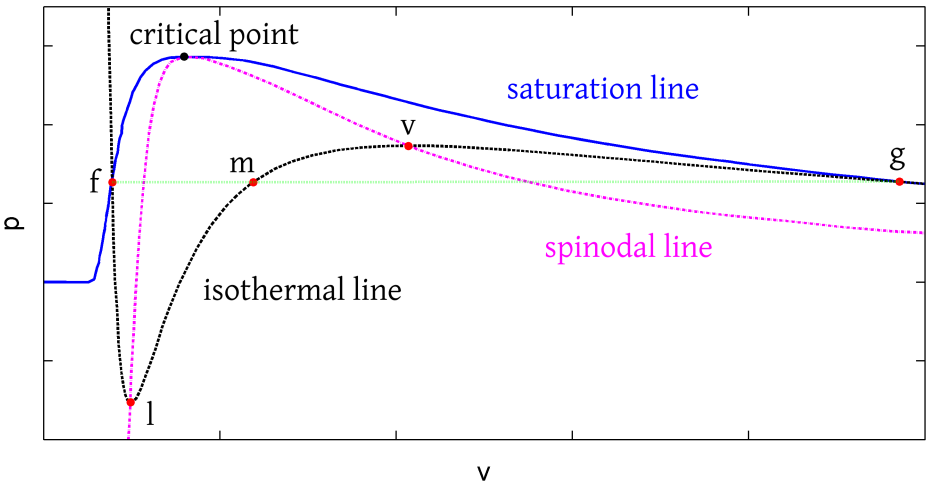

Fig. 1.5: Illustrated concept of the spinodal line

diagram the equilibrium state of coexistent phases is considered by the horizontal (green) line given. Using the Van der Waals fluid definition the state moves along a “s-shaped” line (see Fig. 1.5 - black line: flmvg) through the two phase area instead of a horizontal straight line. By interconnection of the minima and maxima of the isothermal curves the two-phase area is divided into two metastable and an unstable area. The metastable areas mark the superheated liquid and the sub-cooled gas that may remain stable for a certain period of time upon crossing the saturation line. At least for low superheat it is reasonable to extrapolate the liquids properties. The line 'fl' marks the superheated liquid. The line 'lmv' is the unstable area in which volume and pressure increase simultaneously. The line 'gv' shows the metastable area of the gas entering the two-phase area.

An expansive overview concerning the topic of nucleation is given by D. Kashchiev [46], whose works are very influential on that research topic. Nearly all major contributions concerning nucleation are gathered and summarised. Subsequently many types of experiments were designed to ascertain nucleation rates. As there are many works that experimentally investigated nucleation only a few major ones shall be mentioned here. An interesting work reviewing theoretical and experimental aspects of nucleation was given by Blander and Katz in 1975 [47]. The focus was on super-heating of fluids and in consequence the possible violent explosion that might impose hazard to its environment. The homogeneous supersaturation limit may be up to 90 % of the liquids critical temperature. Heterogeneous nucleation is likely to happen at lower supersaturation because of the catalytic effect of surfaces which poses a threat as contact vapour explosions might happen. Less super-heating may lead to less extreme events such as geysers. Boiling may occur over a range of temperatures and not at any particular temperature.

Experimental investigations directly measuring nucleation rates were conducted by several authors for various substances. Miller et al. [13] used an expansion cloud chamber to investigate homogeneous nucleation rates for water over a wide range of temperature and nucleation rates from 10^{6}-10^{12} drops per m^{-3} s^{-1}. Later Viisanen et al. [48] used the nucleation pulse technique to measure nucleation rates from 10^{11}-10^{15} per m^{-3} s^{-1}. The data analysis had qualitative agreement in the range of overlap with Millers results. Comparison to classical theory showed at some points exact agreement, but a different temperature dependency in the theory. They concluded that there is serious disagreement between their measurements and the theory. Wölk and Strey [12] summarized several authors measurements of nucleation rates in light and heavy water ranging from $1x10^{6}$-$6x10^{21}$ per cubic metre and second. Based on these collected measurements they introduced an empirically corrected function for homogeneous nucleation rates in water correcting the Becker/Döring theory with an additional factor. Unfortunately the calculated rates

for water very often did not match the experimental findings. The discrepancy between theory and experiment alternated by being accurate and off by several orders of magnitude. In weather research there is even a distinction between 'real' and 'apparent' nucleation rate [14].

Summarising the theoretical and experimental works concerning bubble nucleation, it can be said that they offer insight into the physics but cannot yet deliver the step towards macroscopical application. The process of nucleation itself happens on a microscopical scale and omits the following growth process of the created nuclei to the macroscopical scale. If the number of nuclei is calculated correctly, it still remains unclear if the number of macroscopical bubbles matches. The number might actually change during growth due to unconsidered mechanisms.

Computational Fluid Dynamics (CFD) Simulation

In nuclear industry many specialised codes for thermal-hydraulics are available. These codes are very fast compared to CFD codes and offer quick-turn results obtained by simplified modelling. A common drawback is the extensive modelling needed for a specific safety analysis. Hence CFD aims to be applicable in a general way and therefore becoming a powerful tool for safety analysis. Several authors did apply CFD to problems usually calculated by dedicated codes.

Computational Fluid Dynamics (CFD) are nowadays a common and accepted simulation tool in fluid mechanics. CFD simulations are based on the Navier-Stokes equations, which are a full set of conservative equations for momentum, mass and energy including friction losses. As this set of equations can usually only be solved numerically the calculation domain needs to be discretised. Mostly Reynolds Averaged Navier-Stokes Equations (RANS) are utilised as they are least costly. The lower effort results by not resolving small eddies but modelling them by introducing additional viscosity as it is modelled in turbulence models. Using these RANS equations as base several formulations for multiphase flow are available. Some of the most influential authors are M. Ishii [49], R.I. Nigmatulin [50] and D.A. Drew [51]. This work will be using the time averaged Euler-Euler formulation that is comprised by two sets of standard RANS equations simulated in the same space that was introduced by D.A. Drew. The two inter-penetrating simulated fluids, of which one is continuous and the other is dispersed, are coupled by exchange terms for momentum, mass and energy. For coupling, numerous models are available for the various interactions. In bubbly flows there are several forces present. In case of phase changes additionally mass- and energy transfer rates need to be modelled.

Sokolichin et al [52] compare the Euler-Euler and Euler-Lagrange methods by calculation of two-dimensional test problems. A transient simulation of a locally aerated bubble column is set up using an upwind and second order Euler-Euler scheme, and correspondingly, an second order

Euler-Lagrange set-up. Both second order simulations deliver quantitative agreement, but the upwind scheme used with the Euler-Euler description does not. The upwind schemes inherent diffusivity produces incomparable results. Concerning computation times the Euler-Lagrange method is less costly for small bubble numbers but less well performing with high bubble numbers. Above 10 % gaseous fraction both methods are unable to deliver reliable results without additional modelling of bubble-bubble interactions.

Another paper by Farzpourmachiani uses an Euler-Lagrange formulation to perform 3-D unsteady 3-D simulations in a rectangular column to consider bubble interactions [53]. It was confirmed that with slender and high water columns a highly dynamic flow pattern with multiple staggered vortices prevails, whereas in wider configurations the 'cooling tower' flow pattern with a single vortice prevails.

Ekateina et al [54] investigated in their paper bubble creation and development during rapid de-pressurisation. An Euler-Langrange approach was used as mathematical formulation. The heterogeneous nucleation theory utilises a log-normal nucleus size distribution. Using this size distribution all nuclei in this distribution being bigger than the critical radius in homogeneous nucleation will grow. Additionally a wall boiling model is incorporated. The simulations considered flashing inside a nozzle and concludes that the wall boiling model combined with the pool boiling model are necessary for good agreement with experimental data. The heterogeneous model in essence increases the bubble number according to a log-normal function depending on the super-heating.

In his Ph.D.-thesis M. Heusch [55] demonstrated an approach considering the bubble nucleation using the Boltzmann-theory. The whole process of bubble nucleation and growth is considered a thermally activated chemical reaction. The basic number of bubbles is the number of particles known to be in the fluid. As stated earlier, any particle might act as an catalyst to nucleation. By minimising the Gibbs' free energy, the probabilities for changes from an inactive to an active nucleus are calculated. Hence, locally, a changing number of activated nuclei is present. The size changes are then calculated using a simplified Rayleigh equation as cavitation is modelled. The calculation still uses the preset of the minimal bubble diameter which, again, greatly influences the result. Overall satisfying simulations concerning cavitation in the valves of Anti-lock Braking Systems were conducted.

Based on the study by Giese an investigation by E. Laurien [56] calculated thermal cavitation in pipe bends by varying the constant bubble diameter or the constant bubble number density and concluded that CFD can calculate correct pressure losses but again prescription of bubble size or bubble number density determinate what the result is. However, it is stated that using a number

density seems more physical as bubble size change are possible from initially small nuclei.

Further insight into the dependency on the bubble diameter description is given by a sensitivity study conducted recently by Asher et al. [57]. Many models use a certain number of tune-able or experimentally based parameters and in the study the uncertainties are quantified by systematically computing the global sensitivities of the outputs to the model parameters. The DEBORA benchmark has been calculated using Star CD. One of the models considered was the equation given by Tolubinsky and Konstanczuk [58]

$$d_w = d_{ref} \exp\left(\frac{-\Delta T_{sub}}{\Delta T_{ref}}\right) \tag{1.1}$$

that calculates the bubble departure size d_w in water depending on the local sub-cooling ΔT_{sub}. The constants d_{ref} = 1,4 mm and ΔT_{ref} = 45 K are semi-empiric factors determined by the authors. It is a necessity to calculate the diameter to get the evaporative heat flux and evaporative area fraction. As a result of a multiple parameter variation the prescribed parameter d_{ref} has the greatest influence on the result and is hence important to model correctly.

Tu and Yeoh [59] show that reactor safety considerations using RELAP5 and CATHARE cannot predict void fraction distributions under low-pressure conditions. Because of that they use a more general tool, namely Ansys CFX®. However in Ansys CFX® most validation was done under higher pressures and in summary under low-pressure conditions the boiling models used in Ansys CFX® need to be modified as well. The original bubble size model used was originally shown by Anglart and Nylund [60] proposed

$$d_w = \frac{d_1(\Theta - \Theta_0) + d_0(\Theta_1 - \Theta)}{\Theta_1 - \Theta_0} \tag{1.2}$$

and use the parameters minimum bubble diameter d_0 = 1.5x10^{-4} m at Θ_0 = 13.5 K and maximum bubble diameter d_1 = 1.5x10^{-3} m at Θ_1 = 0 K. The diameter changes linearly between d_0 and d_1 and does not change outside the range of 0 K to 13.5 K sub-cooling. They replaced that model by the one by Zeitoun and Shoukri [61] being

$$\rho_{ZS} = \frac{\rho_l}{\rho_g} \tag{1.3}$$

$$\frac{d_{b,sau}}{\sqrt{\left(\frac{\sigma}{g\cdot\Delta\rho}\right)}}=\frac{0.0683\cdot(\rho_{ZS})^{1.326}}{Re^{0.324}\cdot\left(Ja+\frac{149.2(\rho_{ZS})^{1.326}}{Bo^{0.487}\cdot Re^{1.6}}\right)} \tag{1.4}$$

with the parameters $d_{b,sau}$ being the mean Sauter diameter, g the gravitational acceleration, Re the flow Reynolds number, Bo the boiling number and Ja the Jacob number. The calculation results were compared to several experimental investigations and showed that the RELAP model delivers the worst results. The old model is off in some aspects and the the latest model delivers the most fitting results. Again the bubble diameter is only considered in the near wall region as it focused on the heat transfer. The same authors considered [62] flow instabilities caused in a rod bundle due to void generation. During accidents like a LOCA, static flow instabilities may occur in narrow cooling channels due to steam formation. Their concern was with the pressure loss along the channel due to vapour appearance. With increasing vapour fraction single channels may become blocked and the flow may be diverted towards neighbouring channels destabilising the system and possibly causing an excursive or Ledinegg instability. Three stages of the instability are defined: the incipient boiling, the significant voiding and the onset of flow instability. The study shows that it is feasible using CFX 4.4 to predict these three stages using the flow velocity and the void fraction distribution. The two-fluid model demonstrates that it can predict the phenomenon.

A simulation approach that is presented by van Sint Annaland et al. [63] consists of a multi-level simulation that moves from a detailed simulation to a large-scale continuum simulation in several steps. First, single bubble deformations are simulated using i.e. the front tracking method to calculate the deformation of single bubbles. In this method an unstructured dynamic mesh represents the interface explicitly by interconnected marker points. Due to the lagrangian representation of the interface no reconstruction is necessary. This even allows for direct calculation of the surface tension. This offers insight into the bubble-liquid interactions. Based on the result an Euler-Lagrange simulation is performed with the knowledge of single bubble behaviour from the previous calculation step. The calculation broadens the application to interactions between distinct bubbles. Again based on these calculations an Euler-Euler calculation incorporates all the previous results that were obtained and performed an industrial scale simulation. Finally a large eddy simulation (LES) is compared to the Euler-Euler simulation. Bothe et al. [64] calculates the mass transfer between gas and liquid phase using a volume-of-fluid method (VOF). Single bubbles rising in fluid are simulated including their deformation as well.

Bubble Modelling

For modelling the shape of bubbles several closures are available. The so-called particle model

describes the bubble diameter by the input of either the bubble diameter or the bubble number density. As the vapour fraction is a calculation result either the bubble number or bubble diameter can be calculated. Based on the bubble diameter the interactions are modelled. In the case of a constant bubble diameter the bubbles can only multiply and with constant bubble number, they can only change size.

In Ansys CFX® an extended Multi-Size Group (MUSIG) approach is implemented. Two or more bubble size groups are defined and simulated in an Euler-Euler simulation. Every group therefore requires a respective set of momentum equations. Interactions between the size groups are modelled by coalescence and break-up models that determine the number of bubbles that are transferred from one group to the other. In a paper by Krepper et al. successfully calculated the air distribution of poly-dispersed bubbles in vertical pipes [65]. Further development of the MUSIG model accounts for phase changes. Again into a vertical pipe vapour is injected and the condensation is simulated using the MUSIG model with satisfying accuracy [66]. As the computational cost of the method is very high later optimisation aggregate several size groups together and uses a single momentum equation for this aggregation of size groups.

Another concept is to use a transport equation for the inter-facial area as it was presented by Hibiki and Ishii [67]. The inter-facial area concentration is calculated by the rates of change ind the area concentration caused by bubble break-up, coalescence, phase change and bubble expansion. Bubble coalescence is caused by random collisions and induced by the liquid phases' turbulence. The break-up rate is calculated based on random eddy collisions with a bubble and a break-up efficiency parameter. The model is sensitive to the initial bubble size, that has to be assumed. The paper concentrates on air in water, so bubble growth and phase-changes are not considered in detail.

Morel et al. [68] investigated several multi-size bubbly flow models by comparing the respective results with experimental data. The first model, in fact, is a single-size model using the Sauter mean diameter. Two other models assumed a bubble size distribution of which one was log-normal and the other uses a quadratic law. The forth model is the previously mentioned MUSIG model. All these models were used with the CFD Code NEPTUNE_CFD and the results compared to experiments conducted in the MTLOOP of the Helmholtz- Dresden Rossendorf (HZDR). The conclusion was that every model has strengths and weaknesses but the MUSIG model has the potential to overcome its current limitations, while the prescription of a bubble size distribution generally neglects coalescence and break-up behaviour.

In 1980, Mitrovic and Stephan [69] established a relation for bubbles at equilibrium radius based on the Thomson-Helmhotz-equations. It is criticised that often correlations for the inner pressure

of bubbles are based on the surface tension correlation derived from a consideration of a planar phase boundary. They conclude with a correlation that is valid for spherical bubbles over a wide range of temperatures. For small super-heatings the Young-Laplace-equation is sufficiently valid.

One of the first correlations for evaporation from (water) drops was given by Ranz and Marshall [70]. It is considered valid for Reynolds numbers between 0 and 200. The evaporation from drops considered, is a heat transfer by conduction and convection into a decrease causing evaporation. Besides a theoretical consideration the evaporation from drops has been measured. The drops have been attached to a feed capillary keeping the decrease at constant size. That decrease was exposed to an air stream of varying temperature and velocity. Then by measuring the needed capillary feed the evaporation rate was ascertained. For drops without relative velocity with the surrounding fluid the mass exchange rate became constant and minimal. In essence this is evaporation from liquid water to hot air. Hence the airs capability to absorb vapour may be of influence. Still, the correlation is often applied as a standard model.

Hughmark later extended the range for the correlation based on empirical studies [71] for a wider range of Reynolds numbers. For different Reynolds numbers the flow around a spheric bubble changes. First the flow is symmetrical, then it develops a weak toroidal vortex at the rear stagnation point. This vortex increasingly gains strength the higher the flow velocity. At a Reynolds number of 450 the separation does not advance further but the wake becomes unstable. Further increasing Reynolds numbers increases the wakes' oscillation frequency, too. The point when the wake becomes oscillating the exponential law describing the mass transfer changes slope. This is incorporated into Hughmarks' correlation and extends the validity of the original Ranz-Marshall equation.

Usually due to internal mixing processes the inner temperature of a vapour bubble is considered homogeneous and entirely at saturation temperature. That means that an internal temperature gradient is omitted. That way no heat transfer correlation from the centre of the bubble to the phase boundary needs to be considered. This is called the single resistance model [72] and was proposed because of the strong convection observed inside bubbles with moving surfaces [73].

A doctoral thesis by Gaudlitz [74] investigated the shape and trajectory of gas bubbles rising in liquid numerically. A direct numerical simulation for a single bubble rising in liquid is used with a hybrid particle level set method (HPLS) for inter-facial area description. As the level set method has problems with mass conservation, it is combined with marker particles to track the interface. It can be shown that the method can simulate single and a limited number of bubbles including break-up and coalescence. However for higher bubble Reynolds numbers the method needs

adaptive meshing to be effectively calculated as the eddy structures size decreases.

A recent numerical investigation by Chen et al. [75] concerning bubble pairs rising one behind another shows that the bubble pair moves faster than a single bubble. The trailing bubble moves faster that the leading bubble. Therefore the bubbles collide and coalesce. After coalescence, the bubble shows velocity and shape oscillations. This effect was observed in experiments and was reproduced by their simulation method.

Another work by Ramirez-Munoz et al [76] describes the same effect of two spherical gas bubbles rising aligned along a line. A bubble Reynolds number between 50 and 200 was investigated and a semi-analytical was model proposed that depends on a reference liquid velocity. The separation distance between bubbles is calculated as well. Ultimately, the error in predicting the trailing bubbles drag is between 10 % and 70 %, which is in the same range as analytical predictions. However the simple modelling allow for flexible application to many drag situations as bubbles, drops and solid spheres can be adapted using the right drag expression.

In the same field of investigation, the drag forces among bubble swarms Roghair et al [77] emphasise the importance of correct drag modelling. Along a bubble swarm the drag is changed by interactions between the bubbles. They employ an advanced front tracking model that can simulate up to 50% gas hold-up. The drag correlation presented is valid for different bubble diameters for medium to high Reynolds numbers and was implemented in a larger scale model. The effect of the correlation was investigated in Lau et al. [78]. It was implemented in an Euler-Lagrange model. The simulation set-up was done for a water/air system for which experimental data was available. The new drag correlation is found to deliver better results than the single bubble drag model. The liquid velocities and fluctuations were predicted better and it is stated that still better closure terms are need for accurate bubble velocity predictions. These predictions are important as the local gas fraction hereby is determined.

Göz et al. [79] simulate bi-disperse bubble swarms using a front tracking direct numerical simulation approach. The goal was to evaluate the dependency of the mean rise and fluctuation velocities of the bubble populations and the induced liquid turbulence on the size ratio, deformability and total volume fraction of small and large bubbles. It is concluded that bubbles may behave very different in presence of other size classes, than they do in mono-dispersed systems. Neither bubble interactions nor Reynolds stresses are non-isotropic. Another contribution made by Lehr and Mewes [80], states that in two-phase flow momentum, energy and mass transport processes occur obviously through the interface between the phases. This is why the interfacial area density is the key parameter when modelling such processes. The local interfacial area can be calculated using the local bubble size distribution. Common approaches describe the

interfacial area density globally. Local approaches describe the area density depending on bubble size distributions and models for bubble break-up and coalescence. Their model derives a transport equation for the mean bubble diameter in bubbly flow. Calculations with dispersed nitrogen and continuous water show good agreement with results presented in literature.

Natural Convection

Concerning the simulation of natural convection situations quite some work is being conducted as well. Rodriguez et al [81] performed an investigation of an initially stagnant fluid in a vertical cylinder which is submitted to heat losses. The laminar natural convection developing is checked for its long term behaviour and a correlation is given for the long term heat losses. The goal is to improve thermal energy storages by minimisation of losses. A dimensional analysis is executed and the main values represented are the Rayleigh number, the aspect ratio of the cylinder and the overall heat loss coefficient that stems from the insulation. By usage of the dimensionless parameters a long-term global heat transfer coefficient is derived that predicts the loss with a maximum relative error of 12 %.

Two phase natural convection has been calculated and compared with PIV measurements in Ghandi et al [82]. Herein inside a PTFE (Polytetrafluorethylene) tube there is a condensing vapour flow that can be varied in pressure, and hence in temperature. The tube is located inside a 0.6 x 0.6 x 0.8 m^3 water volume and positioned vertically. The tube acts as a constant temperature heating on the water. Depending on the temperature of the heater tube single or two-phase convection develops and is measured by a PIV system as well as by 16 thermocouples. Another value is the amount of steam condensed for the estimation of heat input. The single phase temperature distribution inside the tank shows very good agreement between experiment and simulation. Even in the two-phase situation where vapour is generated at the rod is in good agreement. The sub-cooling of the water is very high and the water level only 0.5 m, so that pool boiling effects do not occur.

In the ESBWR design by GE Hitachi natural circulation boiling system behaviour needs to be analysed. The nuclear core neutronics depend on the mass flow rate and vapour fraction through the core. The mass flow rate depends on the core power the composition of vapour and water. A study concerning the sensitivity on the mass flow rate on the core power was performed by Espinosa-Paredes et al. [83]. Another study by Kozmenkov [84] validated the RELAP5 codes' ability to predict flashing-induced instabilities using experimental data from the CIRCUS test facility.

Critical Heat Flux (CHF)

Krepper et al. [18] described several CFD approaches to model sub-cooled boiling and the

respective capabilities to model fuel assemblies. Although sub-cooled boiling is used in many industrial applications because of its effective heat transfer mechanism, it is limited by the critical heat flux. A sudden decrease in heat transfer causes rapid heater temperature excursion that may cause damage. Nuclear fuel bundles are limited in the permissible heat flux to avoid such damages. By applying CFD methods to the problem, fuel assembly safety analysis may be facilitated. The only currently available CFD method to model significant vapour fractions is the Euler-Euler formulation. For bubble diameter the Kurul and Podowski model as shown in (1.2) is used with the parameters $d_0 = 1\text{x}10^{-4}$ m at $\Theta_0 = 13.5$ K and $d_1 = 2\text{x}10^{-3}$ m at $\Theta_1 = 5$ K. The calculated results point out that specific experiments for CFD validation need to be designed for improvements. The results were quantitatively correct and predict the right tendencies in parametric studies. It is important to emphasise that the bubble sizes in the bulk liquid are correlated to the local sub-cooling.

Byung Soo Shin et al. [85][86] experimentally investigated the critical heat flux (CHF) for a nuclear rod bundle experimentally set-up by a heater rod and later performed comparative CFD calculations. The used formulation is an Euler-Euler-model that was used to investigate the effect of guiding vanes on the CHF. The calculations have shown a good agreement of the averaged void fraction. The guiding vanes have caused a decrease in vapour fraction near the heating rods which enhances the CHF. It is not discussed how the shape of the vapour is modelled. The vapour fractions are in the range of 0 - 70 % but there is no information given on how the bubbles or slugs are shaped. It seems unreasonable to discuss how well momentum interactions are calculated, if the geometrical distribution is unknown.

Recently, Le Corre published two papers [87][88] dedicated to wall boiling that reviews the flow regimes of the critical heat flux under sub-cooled boiling conditions. The first paper reviews the current modelling status in literature and shows visualisation of different boiling conditions. Based on this, a mechanistic model is created and applied to the CFD code Ansys CFX®. Calculations are performed but the behaviour of the bubbles apart from the wall are not considered.

Chandraker et al. [89] investigate the critical heat flux that depends on the flow pattern of the system. The investigation of the influence of the flow pattern on the CHF is important to understand the basis of the mechanisms. It is suggested to create models for CHF dependent on the local flow pattern.

Cavitation

Brennens' book “Cavitation and Bubble Dynamics” [90] first defines the difference between

boiling and cavitation to be difference in the thermodynamic way to reach super-heating. While boiling is reached by heat input, cavitation originates from de-pressurisation. An important statement is that micro-bubbles being present as contaminant are potential nucleation sites. The concept of the spinodal is shown as well as a short summary of the classical nucleation theory. A holographic measurement of the cavitation number density distribution gathered from three authors [91][92][93] is shown. It is interesting that the distribution functions are nearly linear in the logarithmic diagram. It is to be noted that the cavitation numbers measured in different water tunnels around the world show very different results. Apart from that the Rayleigh-Plesset equation is introduced which is commonly used when modelling cavitation. As dissolved gases are present in every liquid these are partially present in the cavitation bubble. Therefore the bubbles pressure term changes because of the partial pressure of the dissolved gas.

In thermally controlled growth, after the first critical time of initial bubble creation is exceeded, the driving term and the thermal term become dominant. Prosperetti and Plesset in 1978 [94] published a paper about thermally driven bubble growth. Their law is only valid for bubbles that grow an order of magnitude from their initial radius, which is still in a microscopic range.

Summary

In summary the problem that is at hand is a flow problem involving multiple phases and phase changes.

Experimentally, it becomes clear that the possibilities are limited to date but advanced techniques did gain a lot of insight in the past years and promising techniques are currently being developed. This work will use conventional techniques such as temperature and pressure sensors as well as imaging and digital image processing that will be evaluated with a high level of automation to get statistically valid results. Therefore the modelling needs to be mechanistic based on the observed processes during the experiments. The statistics are then used to support the mechanisms quantitative validity when compared to simulations.

To date, several ways of simulation are available. Among which computational fluid dynamics are considered to be the most general. Methods that involve few modelling are very expensive and limited concerning the problem at hand. These direct numerical simulations have been used to model single bubbles and their interactions with the surrounding liquid. The methods involve up to multiple bubbles and simulate most known physical phenomena. They are suited to consider detailed bubble behaviour involving deformation, pressure fields, mass- and heat transfer among the simulated interface. Even in these simulations a certain amount of modelling is necessary. To simulate higher bubble numbers and more complex geometries at all and with a

reasonable amount of resources more modelling is necessary. To simulate a bigger number of bubbles often Euler-Lagrangian formulations of the Reynolds averaged Navier-Stokes (RANS) equations are used. A discrete number of bubbles is simulated in the same volume as a continuous fluid described by the Euler formulation. Each single bubble is subjected to forces from the liquid or gravity and moves accordingly. The bubbles are usually considered spherical and the forces are then modelled accordingly. The heat- and mass transfer needs to be modelled as well. With increasing bubble number the effort becomes higher. The third and most abstract modelling is the Euler-Euler formulation in which the bubbles are considered to be continuous as well. That means that only the fraction of each liquid is locally known and the bubble diameter and shape are assumed for the calculation of forces, heat- and mass transfer. Hence, an even higher amount of modelling becomes necessary. The models for forces between the phases are comprised of lift, drag, wall lubrication and turbulent dispersion forces. It was shown that single bubble and multiple bubble behaviour differs and the modelling of the forces is under development as well.

The initial creation of an interface is known as nucleation. This so called nucleations description suffers because the physical knowledge is still incomplete. Therefore modelling is a difficult task that may be achieved in the near future. From an engineering point of view nucleation may be irrelevant in most cases that involve volume boiling as nuclei are present in most technical applications. After nucleation the mass- and heat transfer needs to be considered among an interface as bubbles are already present. That is done using several models of which the single resistance model is often used. As PIV techniques showed that inside of moving bubbles there is strong mixing the temperature gradient inside of bubbles is often considered negligible. The interface is supposed to be at saturation temperature which depends on the internal bubble pressure. The bubble pressure is a function of the surface shape and tension. However modelling often assumes spherical shape. The heat transfer from the liquid into the bubble has a heat transfer coefficient that is mostly modelled by the Ranz-Marshall correlation. Any heat transfer directly causes a mass transfer using the evaporation enthalpy to determine the amount of mass transferred. Upon higher vapour fractions bubble-bubble interactions are important as bubbles may coalesce or bigger bubbles may break up into smaller bubbles again. These bubble-bubble interactions change the bubble size and number without necessarily involving mass or heat

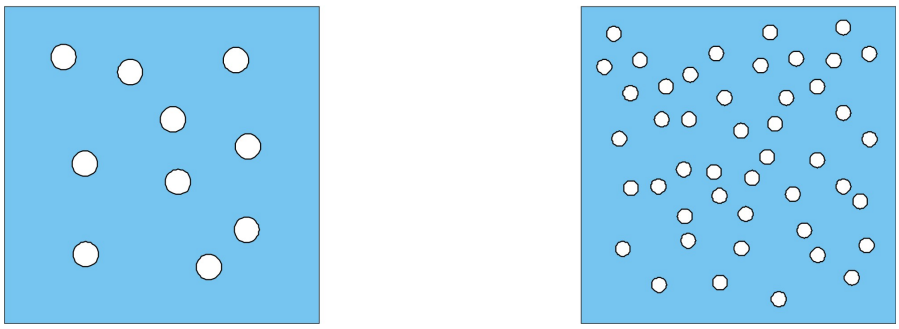

Fig. 1.6: Different possible gas configuration for the same vapour fraction

transfer as they may happen in a system like water/air as well.

CFD is currently under development to become a general tool for nuclear power plant safety analysis. Especially in two-phase flow simulations repeatedly the composition of varying bubble sizes and their interaction with the liquid flow are dependent on user input. As it was shown by i.e. Giese and Laurien the bubble diameter influences the results in CFD greatly. This is because the interfacial area is not only dependent on the vapour fraction, but on whether there are many small or only a few big bubbles present (see Fig. 1.6). The bubble diameter, as well, affects the interaction forces and therefore affects the two-phase natural convection. By development of a model that is able to predict the bubble diameter CFD can be used as a safety analysis tool and create more reliable predictions that allow safety analysis studies in safety relevant cases.

1.2 Aim of this Study

CFD is currently under development to become a general tool for nuclear power plant safety analysis. However in two-phase flow simulations often the composition of varying bubble sizes and their interaction with the liquid flow are influenced by the bubble diameter. This was shown in Gieses' work [21] and again more recently in Ashers' work [57]. There exist various models for the bubble diameter, like the constant bubble diameter or bubble number density approach, the assumption of a bubble size distribution, or the more sophisticated models of inter-facial area transport and the MUSIG model. The first three models lack the ability to be extended towards bubble interactions as break-up and coalescence. The latter two models are complicated or their computational cost is high.

In this study the investigation of a newly built experimental boiling set-up that consists of a high slender container is performed. The goal of the experiment is to visually observe what kind of boiling phenomena happen inside the volume. The observed phenomena are analysed and mechanisms of the physical processes are identified. Based on the mechanisms a model for CFD simulations shall be derived and implemented into the commercial code Ansys CFX®. The modelling shall be simple, descriptive, feasible with CFD methods and introduce only low additional computational cost. Simulations are performed and two aspects are considered. First the qualitative mechanism shall be re-produced and second viable model parameters for a comparative quantitative behaviour shall be found. As the model is based on similar experimental conditions as i.e. a spent fuel pool or passive emergency cooling systems it can be used to assess the nuclear power plants safety in case of accidents.

2 Experimental Set-up and Measurement Techniques

The used test set-up has been newly build for observation of the relevant boiling processes and successive theoretical modelling. The following section will describe the safety analysis of the boiling container and the used measurement equipment and techniques. The whole set-up is depicted in Fig. 2.1.

2.1 Design and Operation

The experimental set-up is based on a boiling container with a rectangular cross-section of

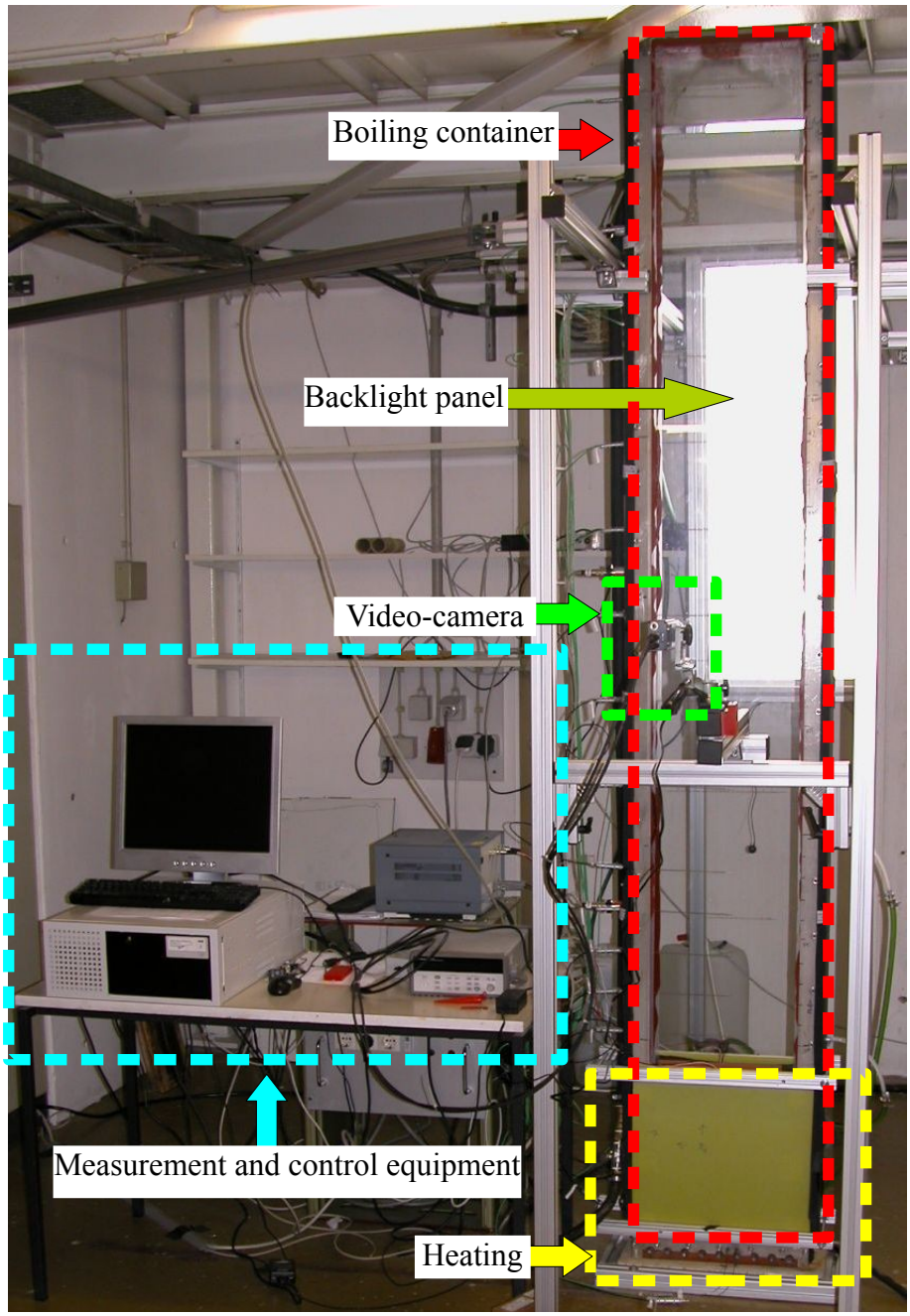

Fig. 2.1: Image of the experimental set-up

390 mm x 97 mm and a maximum filling level of up to 2750 mm. The main frame is build from stainless steel to withstand the corrosive characteristics of the used de-mineralised water. Iron corrosion could cause impurities inside the water by oxide particles which could subsequently affect boiling. An initial consideration of using plates made from Polymethylmethacrylate (PMMA) was discarded as the glass transition temperature is at 105 °C, so glass plates (borosilicate) were chosen instead. The glass plates are surrounded by a extruded U-profile silicone material. The profile is adhered to the glass plates using silicone glue. Silicone material (red) is used as sealant as it allows for appropriate operation temperatures and as well as it offers inert material properties. The glass plates are inserted on the front and back side of the main frame of the container and clamped by another stainless steel frame. That way a water-tight cuboid volume is realised. Compared to the SUCOT experimental set-up [37], which is built with several glass plates a single glass plate for an unobstructed visual access is used. Because of the large glass plates the mechanical strength is lower and therefore the experimental set-up is smaller than the SUCOT set-up although the height to width ratio is comparable.

The bottom heater block is made of copper because of its excellent heat conductivity which suppresses local hot spots as far as possible. To avoid unnecessary void generation the surface is polished (see Fig. 2.2). The heating power is delivered using nine equally spaced electrical heating cartridges inserted in the copper block delivering a maximum heat output of 1110 W each, which results in a maximum heat flux of 264 kW/m². Additionally the lower part of the container is heated by attaching two silicone heating foils to the outer surface of the glass plates (see yellow plates in Fig. 2.1). The heating foils cover an area of 300mm x 400 mm and generate up to 1500W each, resulting in a maximum heat flux of 12.5 kW/m². All heating devices use a closed control loop that keeps the heaters temperature constant. On top of the container a chimney stack is installed where a pressure relief flap is present to prevent damage to the glass plates in case of an internal pressure increase. The system is therefore open. Attached to the chimney a heat exchanger re-condensates the produced vapour. The re-condensed water is recirculated into the boiling container via a hosepipe that is attached to the side of the container 275 mm above the heating surface. As the cooling fluid at disposal in the laboratory is of unknown composition a closed water loop is installed with a second heat

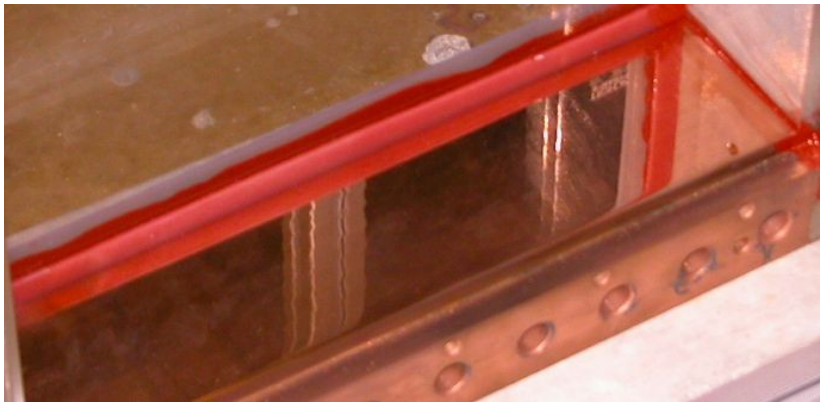

Fig. 2.2: Polished copper heater block

exchanger in between. In the secondary loop of the heat exchanger a flow meter and temperature sensors are installed at the inlet and at the outlet. The whole set-up including temperature and pressure measurement positions is illustrated in Fig. 2.3.

2.2 Description and Test of Measurement Equipment, Error Estimation

In the test set-up temperatures are measured at several positions in the bulk volume (see Fig. 2.3). The exact height of the temperature sensors is given by Tab. 2.2. Their position is centred in the cross section. Shielded temperature-sensors with a diameter of 1.5 mm are inserted from the sides of the container via clamp connections. The used temperature sensors T1 - T9 are four-wire resistance temperature detectors (RTD), hence the connecting wires resistances are compensated. The remaining sensors T10 - T17 are thermocouples of type K. The temperature sensors are attached to a Agilent 34970A using two plug-in boards offering 20 measuring channels (Type 34901A) and one multifunctional plug-in board (Type 34907A) for various functionality. From the data sheets of the measuring device the RTD sensors accuracy is ± 0.35 K [95] and the measurement chain of the data acquisition has an accuracy of ± 0.06 K [96], which results in an error of ± 0.41 K. The thermocouples nominally have a measuring error of ± 1.5 K [97] and additionally the data acquisition system adds another ± 1 K resulting in ± 2,5 K error. As these accuracies, especially of the thermocouples, are not acceptable the temperature measurement chain is calibrated for each channel using a metal-block calibrator system (Kelvimat) with a reference thermometer (Pt 1000) that has a systematic uncertainty of 0.011 K. The data acquisition system has a resolution of 0.1 K, which therefore is considered to be the achieved accuracy.

Pressures are measured at the positions P1 – P4 using absolute pressure transducers with floating piezo-resistive elements made by Keller (Type: PA(A)-35XHT, 0.8...1.3 bars, absolute pressure). The sensors are attached to the side wall of the container with the pressure membrane being in contact with the liquid column. The positions of h(y) (see Fig. 2.3) are given in Tab. 2.1.

Tab. 2.1: Positions of the pressure transducers

		P1	P2	P3	P4
h(y)	[m]	0.8	1.6	2.4	Ambient

The pressure transducers have an integrated temperature measurement and a microprocessor that compensates temperature changes in the piezo crystal as well as non-linearities, resulting in 0.1% of the total pressure range. Therefore, the absolute error is 50 Pa. The measured value is directly sent via an RS485 interface so that no additional error from analogue measurement needs

to be accounted for.

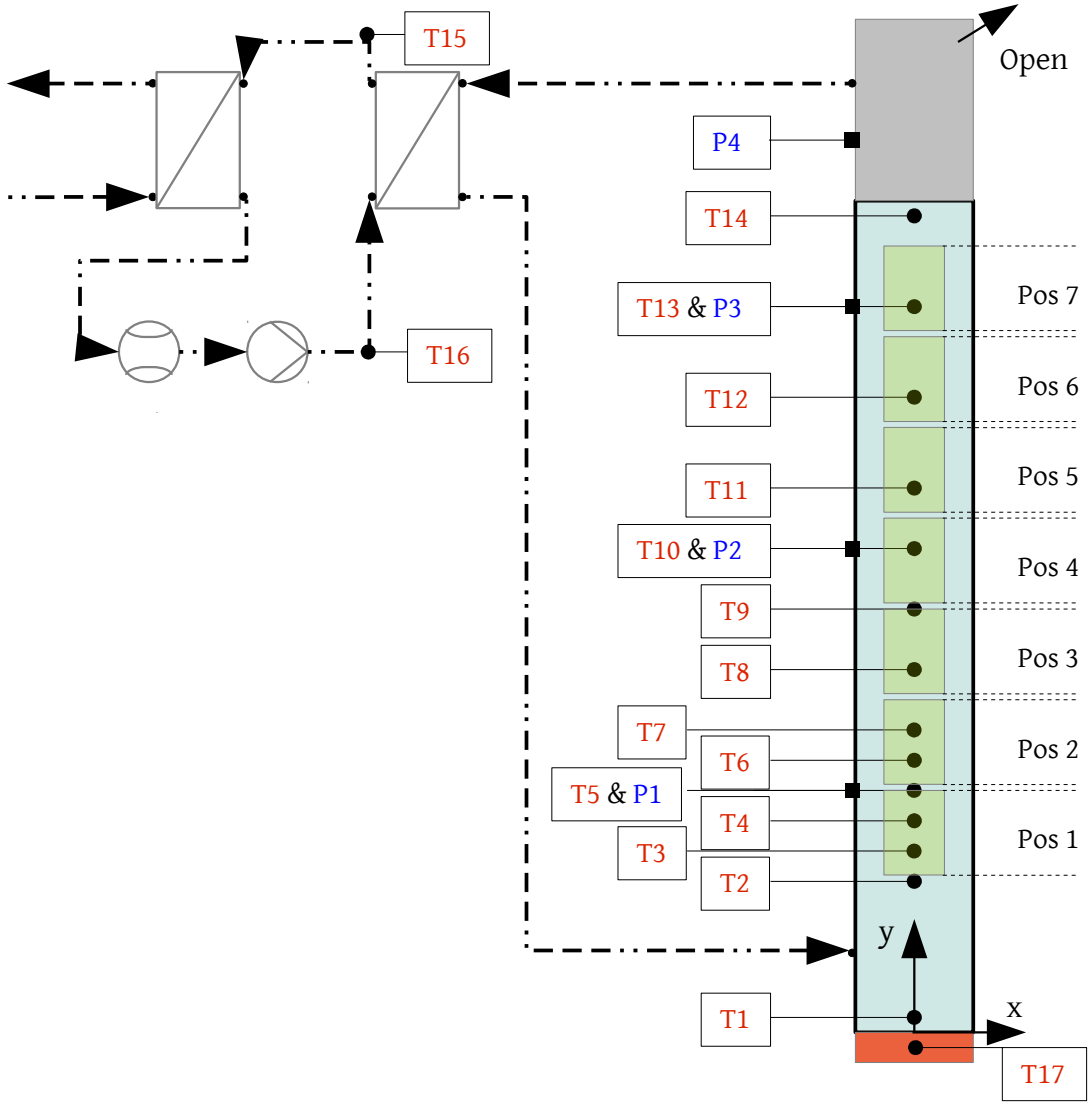

Fig. 2.3: Illustration of the experimental set-up including measurement positions

Tab. 2.2: Vertical temperature measuring positions above the heating surface

		T1	T2	T3	T4	T5	T6	T7	T8	T9	T10	T11	T12	T13	T14
h(y)	[m]	0.05	0.5	0.6	0.7	0.8	0.9	1.0	1.2	1.4	1.6	1.8	2.1	2.4	2.7
		RTD									Thermocouples				

2.3 Image Acquisition

One of the most significant features of the created set-up is the visual access that allows for non-intrusive video recording of the generated vapour bubbles inside the volume. Upon recording, the process is analysed using digital processing techniques that will be described in the following sub-chapter. The subsequent possibility of bubble tracing offers additional information concerning bubble velocities. Image processing has become a widespread tool in many industrial applications. Hence there is a lot of software available for image processing and that includes many advanced operations ready to be applied to the specific problem. In this work the MATLAB® Image Processing Toolbox is used. This simplifies the process of creating a program that offers object detection and characterisation. The possibilities to extract data are expansive and can be found in dedicated literature on image processing.

Fig. 2.4: Fire-wire camera used in the 1st and 2nd measurement campaign

For bubble observation the boiling process is recorded by two different video cameras. The first camera is an AVT Stingray F125b, which offers a maximum resolution of 1292x964 Pixel @ 30 frames per second (fps). The imaging sections used with this camera in the 1st measurement campaign are 200 x 280 mm and 60 x 83 mm in the 2nd measurement campaign. The camera is connected via a IEEE 1394a interface. The acquired 8 bit grey-scale images cause an uncompressed data rate of 36.6 Mb/s and therefore a 20 minutes recording needs 42.88 gigabyte of storage space. For storage these data are compressed using the lossless Lagarith codec which has a compression rate of approximately 0.5. The camera's input is stored on a 750 gigabyte RAID 1 disk array on the measuring computer. With this camera 1st and the 2nd measuring campaigns were recorded. The second camera used is an AVT GX1050C and it offers higher frame rates but a slightly lower resolution. The camera is connected via a gigabit ethernet connection and has a resolution of 1024 x 1024 pixels @ 72 fps. The resulting data rate is 72 Mb/s and would have exceeded the capabilities of a IEEE 1394a connection. This camera is used for the 3rd measurement campaign that aims for bubble tracking, which improves tracing because of the lower displacement of bubbles between two frames. The

Fig. 2.5: Gig-E camera used in the 3rd measurement campaign

recording strategy has been changed so all processes are done in the system's random access memory. Only the processed results are saved onto the hard disk drive.

2.3.1 Object Recognition

As already mentioned in the description of the test set-up the front and the back of the boiling container are made of glass. The optical arrangement is to provide sufficient lighting capabilities. There are two aspects of importance. First, the bubbles need to be detectable to a degree where they can clearly be distinguished from the background. Hence, an arrangement with good contrast is preferred. Second, the intensity should be high, because short shutter times can be achieved. This suppresses in-motion blur and additionally allows for high frame rates if needed.

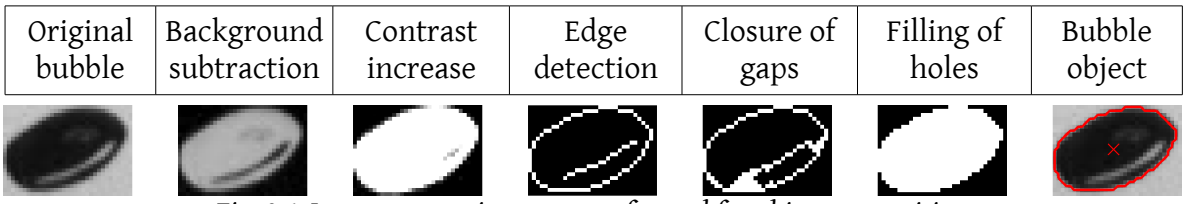

Fig. 2.6: Image processing steps performed for object recognition

Therefore, a diffuse transmitted-light arrangement was chosen using a LED panel with the dimensions 1200 x 450 mm that delivers 5400 lumen of light. That corresponds to 10000 lux lighting intensity. The possibility of using a large image section is necessary because the boiling process has not been expected to be fixed in one place. For the video recording, a trade-off between resolution and frame rate has to be made. The video recording results in a projected 2D silhouette view of the bubbles. Each image needs to be evaluated using the appropriate processing steps (see Fig. 2.6). The first step is to separate the moving bubbles from the static background. To achieve this a background image is created by averaging each pixel over a number of frames. By doing this, local and short changes in pixel brightness that are caused by a moving pixel are removed. The resulting background image is then subtracted from each image and the resulting image consists only of moving objects. These objects are not yet detectable as the image is still in grey-scale. First the image intensities are remapped so that light grey values are mapped to be white and dark grey values are mapped to be black. This increases the contrast of the image and is followed by a Canny edge detector originally proposed by John Canny [36] which additionally converts the image to binary format. After that, if holes or small gaps are found they are filled. Within this logical (binary) image, objects are identified using the 8-connected pixel method (Fig. 2.7) as described in the MATLAB® documentation [98]. Considering the image matrix given in Tab. 2.3 using the 4-connected pixel method would identify 2 objects

and the 8-connected pixel method identifies 1 object. The detected objects are will henceforth be denoted as blobs.

Tab. 2.3: Example image pixel matrix

0	0	0	0	0	0
0	1	1	0	0	0
0	1	1	0	0	0
0	0	0	1	1	0
0	0	0	1	1	0

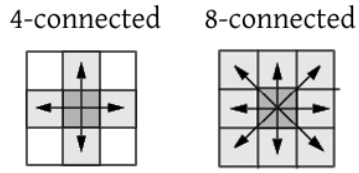

Fig. 2.7: Blob identification [98]

All these methods are presented as well i.e. in "Morphological Image Analysis" written by Soille [99], or alternatively in "The Image Processing Handbook" by Russ [100]. Now that the image objects are recognised, counting is trivial. However, these blobs represent the detected bubble and therefore the projected area basically is an arrangement of pixels. The position of the blob is known when the centre of each object is calculated. Each pixel represents a certain area and the size of the area is easily estimated by counting the number of a blobs pixels. Similarly, the perimeter is extractable i.e. by creating a traverse along the edge pixels of a bubble object. Using the area A and perimeter P of the blob the roundness R can be estimated using the following definition

$$R = \frac{P^2}{4\pi A} \quad . \tag{2.1}$$

Upon validation of a limiting value of roundness an equivalent diameter can be estimated. Further insight into bubble shape is given by using the eccentricity as second value. An ellipse that has the same semi-major axis as the object region is used for a scalar which is the ratio of the foci distance of the ellipse and its major axis length. Hence, the value 0 describes a perfect circle and 1 a line. The eccentricity value E_{cc} changes sharply upon small deviations from a perfect circle. Therefore the parameter offers a larger range of values that can be considered as reasonably round (see Fig. 2.8) and the eccentricity E_{cc} does not depend on the perimeter estimation as in the roundness definition.

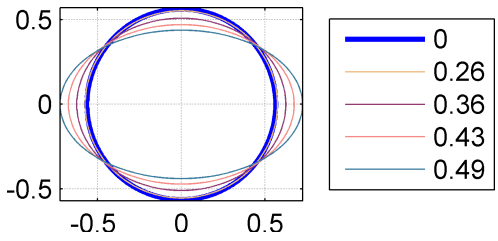

Fig. 2.8: Illustration of the changes in the eccentricity E_{cc}

$$E_{cc} = \sqrt{1 - \left(\frac{y}{x}\right)^2} \tag{2.2}$$

For this investigation the most important two quantities for modelling purposes are defined in Tab. 2.4.

Tab. 2.4: Most relevant bubble properties for modelling

Parameter	Unit
Bubble number density	[1/m³]
Equivalent bubble diameter	[mm]

The processed image data are saved and available for statistical evaluation. To extract transient data the available data are processed using a tracing mechanism that will be discussed in the following sub-section.

2.3.2 Object Tracing

Bubbles may begin being recognised anywhere and any-time inside the volume. They keep changing their size and shape constantly and, therefore, tracing becomes a difficult task. As the bubbles already went through detection the blobs are available as object data. Therefore the position of all bubbles detected in an image are available for tracing. The developed algorithm is basically a closest neighbour search algorithm that accounts for certain restrictions in the movement of the bubbles. The whole program flowchart is shown in Fig. 2.10. The bubbles inside the volume always move within an expected speed regime. This limits the displacement that is possible between two frames resulting in a circular search area.

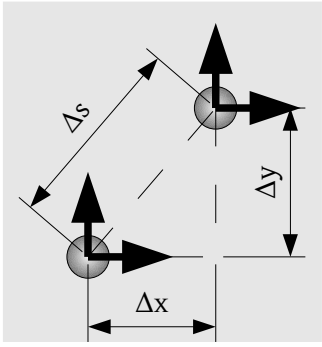

Fig. 2.9: Frame-to-Frame bubble displacement

$$y_{max} < \Delta s = \sqrt{\Delta x^2 + \Delta y^2} \tag{2.3}$$

There might be events of entrainment in a downward convection that pulls bubbles downwards but this has only been observed upon eruptions that induce such strong downward movement in the upper part of the volume. Therefore to make sure the newly considered bubble has moved upwards the following criterion applies.

$$0 < \Delta y < y_{max} \tag{2.4}$$

Bubbles keep moving along a line or along a meander-shaped trajectory. This limits the possible

lateral displacement from frame to frame. To incorporate this effect the search area is reduced further by additionally using a parabolic area. It has been defined in a way that the lateral displacement is half the vertical displacement. Therefore the following set of equation is used.

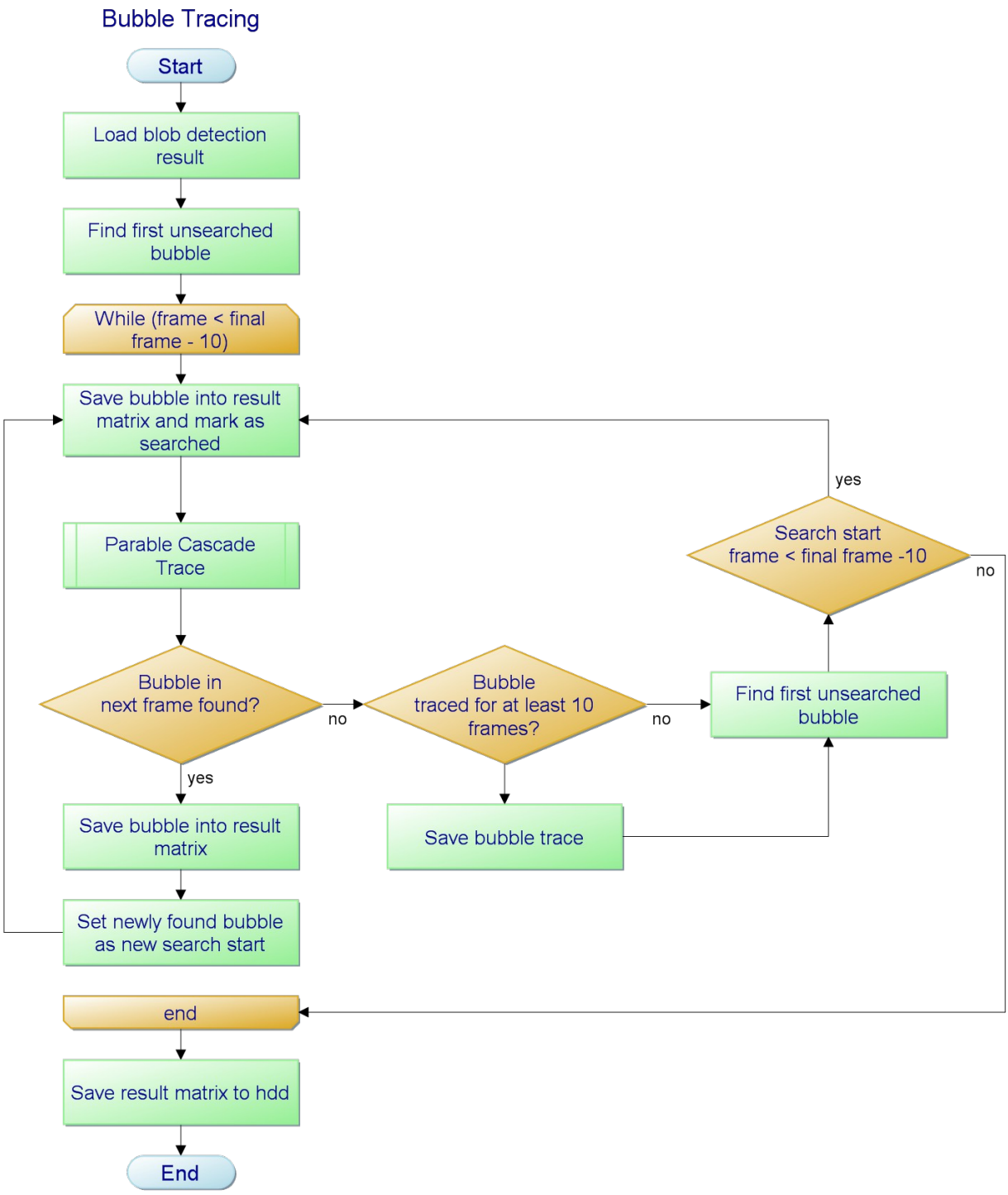

Fig. 2.10: Flowchart of the developed bubble tracing algorithm

$$m_{width} = max\left(2, \frac{1}{2}\sqrt{y_{max}}\right) \tag{2.5}$$

$$\Delta x < x_{max} = m_{width} \cdot \sqrt{\Delta y} \tag{2.6}$$

The search area for y_{max} = 5 is illustrated in Fig. 2.11. The growth rate is limited, but the shape can change drastically from frame to frame, hence these are weaker criteria under consideration. The area change has been limited to the factor 3.

$$0.33 < \frac{A_{n+1}}{A_n} < 3 \tag{2.7}$$

Starting from an arbitrary bubble in the first frame the smallest parabolic search area (y_{max} = 5) is probed for existing bubbles satisfying all criteria. Upon failure the search area is extended (y_{max} = y_{max} + 5) and probed again until either success or failure. If a matching bubble is found the same search algorithm uses the found bubble as new starting point for the search in the next frame.

Bubbles traced successfully are marked so that they are not probed again. The same process is repeated until full failure (y_{max} < 50) and the result is saved if the trace was successful for at least ten frames. The maximum tracing period is in the vicinity of approximately 3 seconds as the imaging section is passed in that time even by small bubbles. That would correspond to approximately 100 frames of tracing. After a successful trace, another algorithm determines the bubble object from which the next search starts from, by finding the first bubble in the earliest frame that was not marked as being traced.

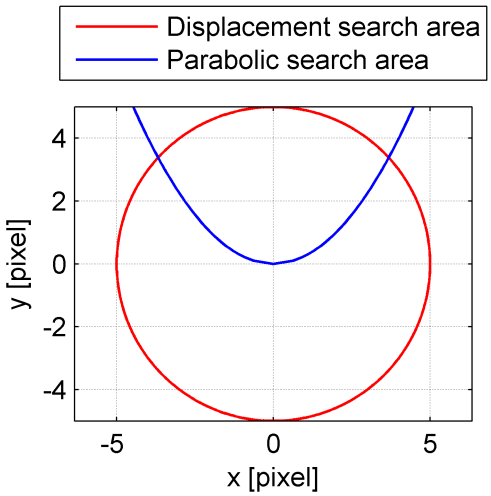

Fig. 2.11: Parabolic cascade search area for bubble tracing

2.4 Verification of Image Processing Techniques

The capabilities of the used software have been tested wherever possible. However a classical error estimation is not possible. The object recognition depends heavily on the contrast, hence on the sharpness of the gradient at the border of a bubble. This might cause errors in the estimation

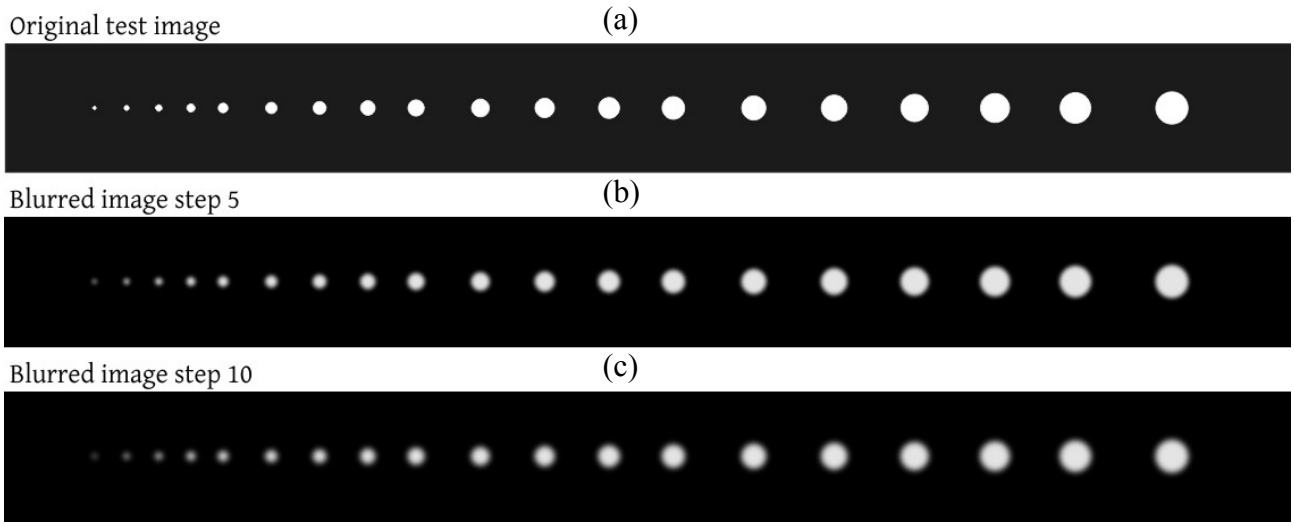

Fig. 2.12: Original testing image (a) and two blurring steps (b)(c) for the edge detection sensitivity testing

of the size. Therefore a testing image (see Fig. 2.12 (a)) is created by arranging perfectly round bubbles with a vector program. The created test image is submitted to the exact same image processing later used for the video recordings. The image is blurred using a Gaussian filter and the sizes are evaluated again. The result is plotted over the several steps of blurring. The relative error of the bubble diameter estimation is up to 52 % (Fig. 2.13), but the average absolute error in diameter estimation is +0.37 mm.

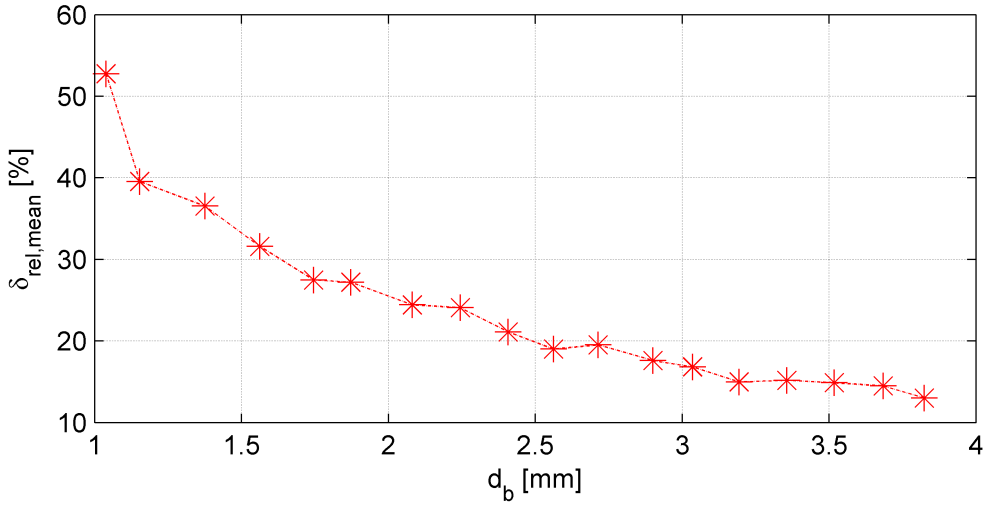

Fig. 2.13: Mean relative error in diameter estimation depending on the bubble diameter

In Fig. 2.14 the relative error of the diameter estimation is shown for 3 different diameters for the 10 steps of image blurring. It can be seen that only the smallest diameter rapidly reaches a high relative error of 52 %. Bigger bubble diameters are overestimated by ~20 % - 30 %, which is acceptable.

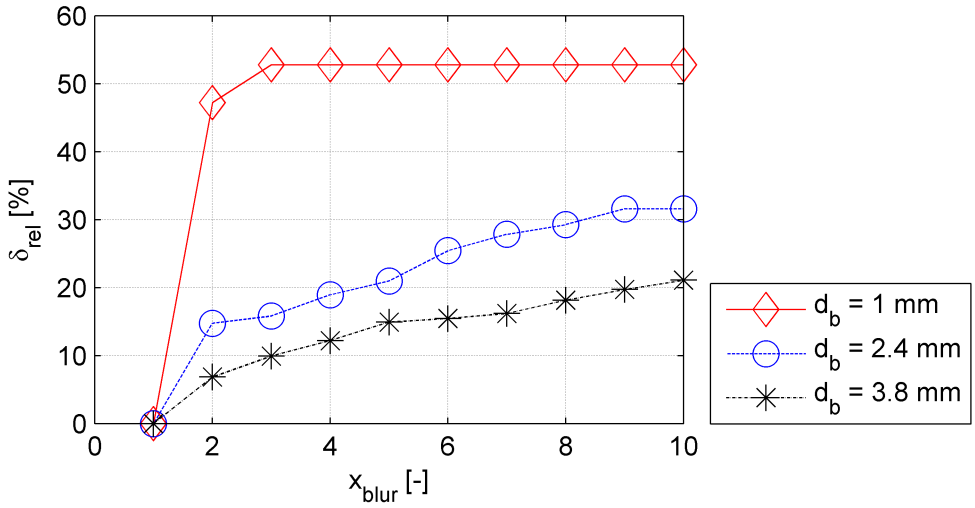

Fig. 2.14: Relative error in diameter estimation with increasing blur

The second aspect to be checked is the estimation of roundness for bubbles that consist only of few pixels. Its obvious that estimating a perimeter of a round bubble from only few square pixels should introduce errors. The estimated roundness R is shown in Fig. 2.15 for the bubbles over their respective size. The same has been done using the bubble eccentricity E_{cc} in Fig. 2.16. It becomes clear that the roundness estimation becomes faulty below approximately 200 pixels of bubble area. The eccentricity is valid down to approximately 100 pixels since the value 0.3 is a bubble that can be considered as round (see Fig. 2.8). In the case of 200 x 280 mm image section a 200 pixel object would correspond to an equivalent bubble diameter of 3.4 mm. In the smaller image section with 60 x 83 mm size the roundness can be estimated down to an equivalent bubble diameter of 0.95 mm. Analogously the eccentricity can be estimated from 1.7 mm diameter, respectively from 0.475 mm. Another test is made by estimating the bubble sizes of the test image with changing the value of the canny edge detection.

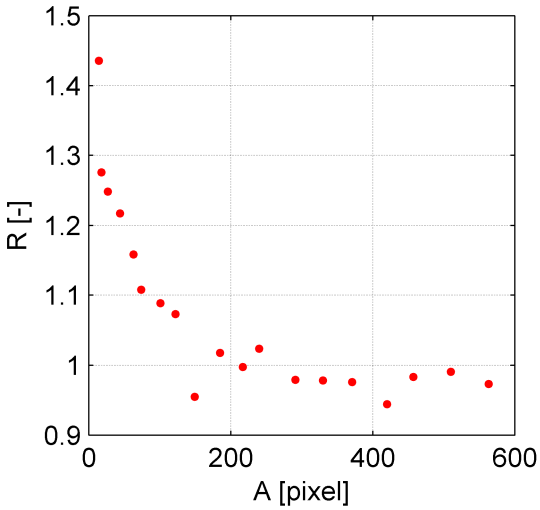

Fig. 2.15: Roundness estimation of perfectly round bubbles with decreasing resolution

The Canny edge detection was probed for sensitivity with the sharp test image and a strongly

blurred test image (see Fig. 2.12). For the sharp image the variation of the canny edge parameter between 0.1 and 0.3 did not show any changes in the result. This is why the test was redone using a blurred image. It can be seen in Fig. 3.1 that above the Canny parameter of 0.2 a relative error of up to 19.2 % has been found. Below that there is no deviation in bubble size detection because of the canny edge detection. The parameter has been set to 0.15 which means that there is no sensitivity regarding this parameter.

The tracing algorithm was tested by evaluation of the results of the bubble recognition. As explained in the previous section the trace was carried out and the results were visualised by reconstruction of the bubble track. Every bubble from the trace is drawn into an white image to visually check the trace. An example is shown in Fig. 2.17 in which additionally the bubble velocity and equivalent diameter is shown.

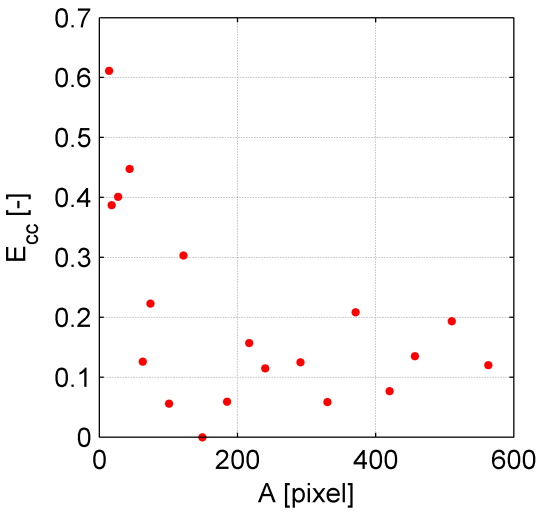

Fig. 2.16: Eccentricity estimation of perfectly round bubbles with decreasing resolution

Obviously the tracing depends on the quality of the bubble recognition which is why no separate testing case is considered. Because of the search algorithm method the only particular problem that still remains is that several bubble traces are aggregated in one trace result which is usually visible because of leaps between bubbles. The

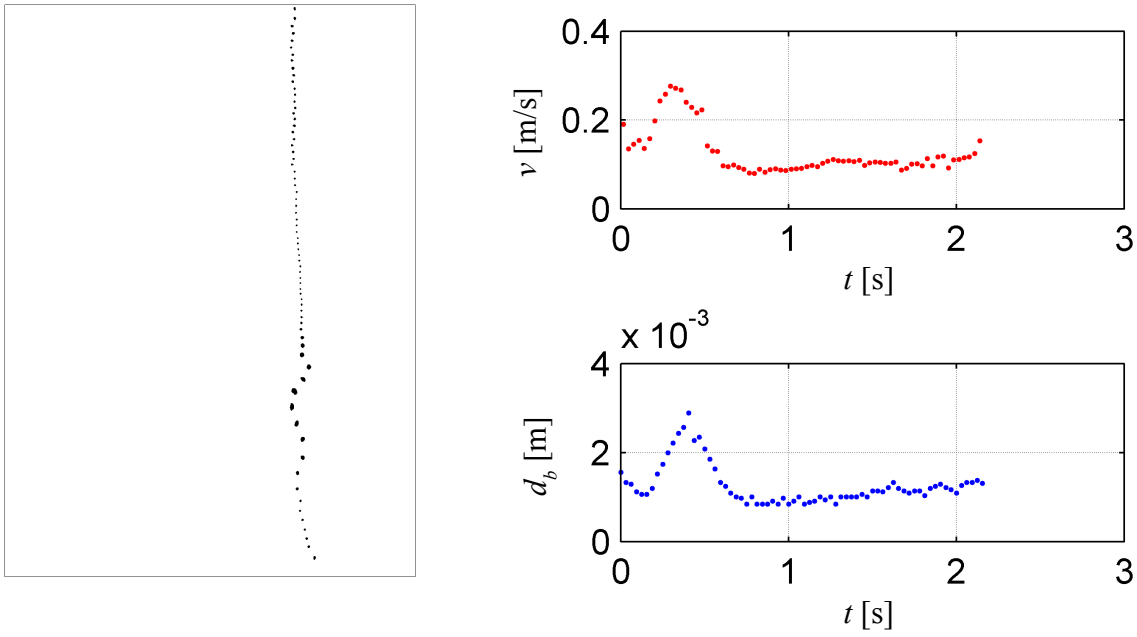

Fig. 2.17: Re-constructed bubble trace result and corresponding bubble velocity and diameter

result of a successful trace is shown in Fig. 2.17 along with the corresponding velocities and bubble diameters. Each velocity and diameter value is associated to the sequentially traced bubble. It can be that the bubble diameter and velocity changes directly concur.

3 Experimental Results

The following chapter will discuss and summarise the experimental data that are relevant and used for the theoretical modelling. The parameters that are of greatest interest with respect to modelling needs are the average bubble number density and its temporal behaviour as well as the average bubble sizes and distributions.

The heat-up time before experiments is approximately 6 hours. After that the temperature in the water is high enough for evaporation throughout the volume. A thermal equilibrium between heat input, evaporation and ambient heat losses is then established. The temperatures at the measuring point are then quasi-steady which means the average value does not change any more and the standard deviation is below 0.5 K. Another clear indicator that the experimental conditions are achieved are repeated events of vapour eruptions.

3.1 Description of Measurement Campaigns

1st Campaign:

The first campaign was aimed towards a general overview concerning the bubble number density and the bubble size distributions. Therefore the investigated area of bubble detection is chosen to be as large as possible. The image section was chosen to be 200 mm in width which is close to the maximum visible area. As the process is recorded with a 1292 x 928 pixel resolution the image section height resolves to 278.4 mm, which is consecutively measured for 20 minutes in seven positions. The smallest bubbles detected are in the millimetre range. This measurement campaign was done for the three different heater temperatures 118 °C, 119 °C and 120 °C. Below 118 °C heater temperature there are no geysering events, hence a minimum heat input is necessary. Above 120 °C heater temperature the heat input causes more violent geysering events, so that less often a dilute bulk boiling situation is present.

Tab. 3.1: Measuring matrix for 1st campaign

	Position	800 mm	1100 mm	1400 mm	1700 mm	2000 mm	2300 mm	2600 mm
Heater temperature	118 °C	each 1200 s						
	119 °C							
	120 °C							

2nd Campaign

The second campaign aims for a more detailed but less general look into the bubbles passing the investigated area. The image section is reduced to 60 x 83.5 mm². Obviously the different image sections are used for different bubble size scales. The smaller image section causes for far more bubbles to pass besides the considered section, which is why this is an additional measurement campaign meant to check the bubble size distribution at smaller bubble sizes down to 0.1 mm bubble radius. The heater temperature was not varied, but set to 119 °C.

Tab. 3.2: Measuring matrix for 2nd campaign

	Position	800 mm	1100 mm	1400 mm	1700 mm	2000 mm	2300 mm	2600 mm
Heater temperature	119 °C	each 1200 s						

3rd Campaign

The third measurement campaign has been conducted for bubble tracing. As before in the 2nd campaign, the heater temperature was not varied, but set to 119 °C. Since evaluation times are excessive the algorithm was changed to record 150 frames to the memory, which are then subsequently evaluated using the previously defined parable-cascade trace (see 2.3.2). Before a 1200 s long recording was recorded and analysed subsequently. The whole process is then repeated as long as the experiment is running (several hours). The camera was positioned arbitrarily as this is a random sample measurement. For each traced bubble in between two frames the displacement is calculated and the size is estimated as the average size in these two frames. This way a large dataset is created with data pairs of size and velocity. The bubbles are sorted into size groups and their size and speed are averaged over the size group. This data is then compared with the investigation Clift et al. [101] conducted to determine the terminal velocity of air bubbles in water.

3.2 Observed Boiling Effects

This sub-chapter discusses the visually observed qualitative phenomena. Detailed analysis on the respective effects will be performed in the following sub-chapters. First some snapshots of typical boiling situations are presented so that the diverse nature of the process becomes clear. Then the growth and re-collapse of a bubble is shown and finally a geysering event is shown.

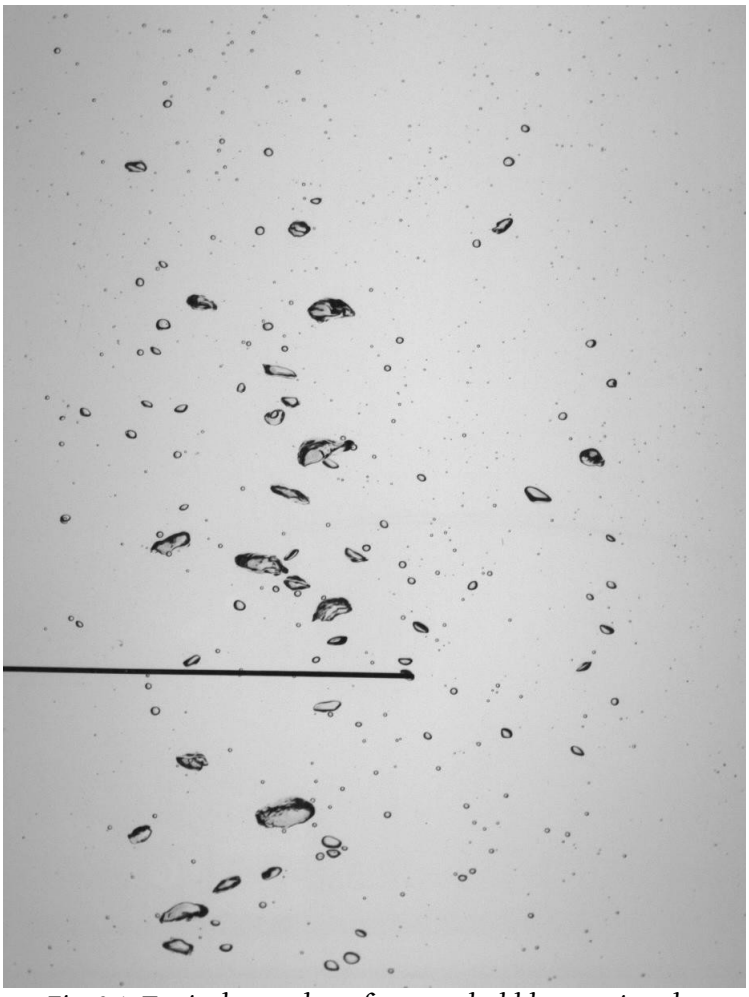

Fig. 3.1: Typical snapshot of vapour bubbles passing the imaging section

In Fig. 3.1 a typical snapshot of vapour bubbles passing the imaging section is shown. In Fig. 3.2 several other possible boiling situations are visible. The number and size of bubbles varies during

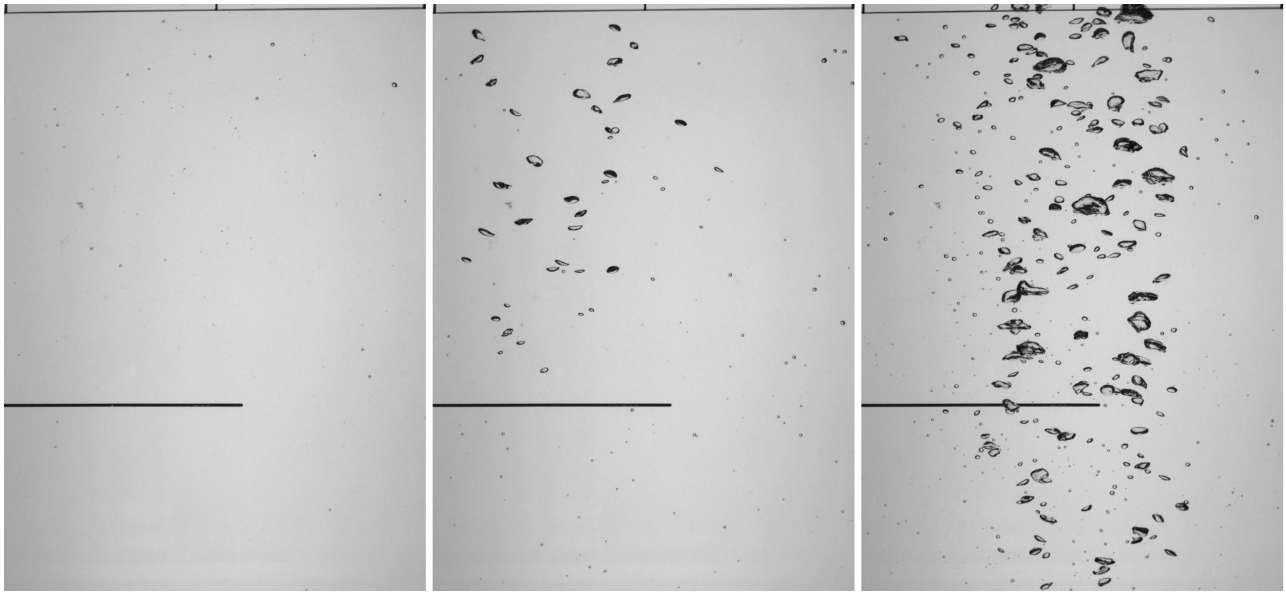

Fig. 3.2: Different possible boiling situations during operation

operation up to a geysering event that will be shown in an image series in Fig. 3.5.

A central mechanism that has been observed is shown in Fig. 3.3. Bubbles may grow spontaneously anywhere inside the volume upon a certain super-heating. The increased buoyancy causes quick upward movement of the bubble. Although the bubble moves into a region of lower pressure and, therefore, lower saturation temperature the bubble re-condensates. The only causal explanation for this is that the bubble runs ahead of a hot water portion and instead encounters a relatively cold water portion that causes re-condensation. The re-condensation heats the water above the hot water portion causing subsequent bubbles to intrude further into the still sub-cooled liquid. At the same time the rising bubbles cause a drag that pulls the hot water portion upwards. When the sub-cooled layer is heated to saturation, a path is created for the following bubbles. Then instabilities such as geysering events may occur. This is considered to be the most basic mechanism to consider.

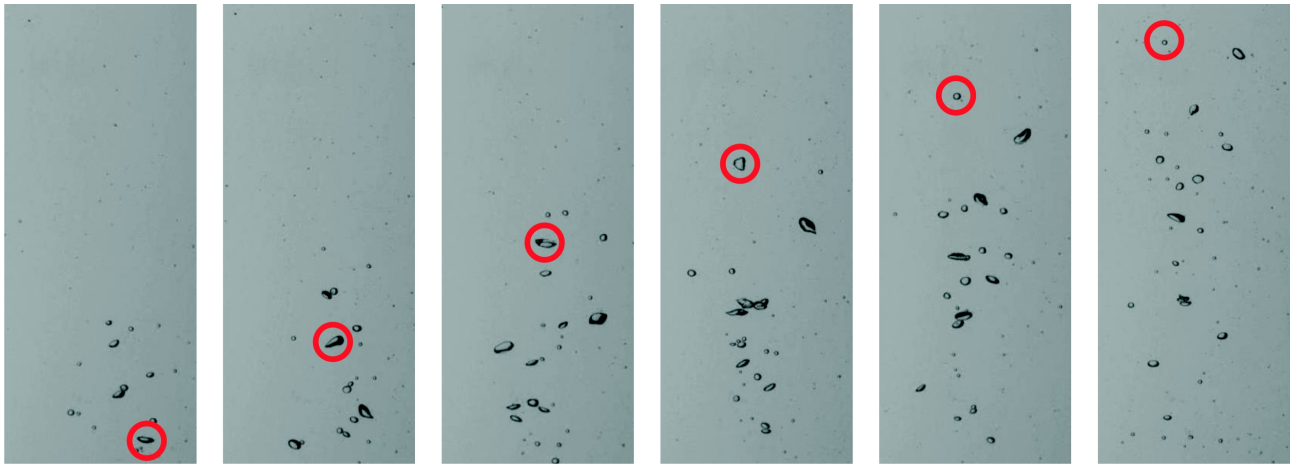

Fig. 3.3: Manual trace of a bubble growing and re-shrinking inside the water volume

This effect has as well been found in the bubble trace conducted shown in Fig. 3.4. On the left the traced bubble is shown. This image is created by overlaying approximately 55 image frames that only contain this traced bubble. Correspondingly the two diagrams shown on the right side show the transient development of the bubble size and bubble velocity during this trace. It can be seen that the bubble grows and re-shrinks in the time interval from t = 0.3 s to t = 0.4 s and again grows starting from t = 1.5 s.

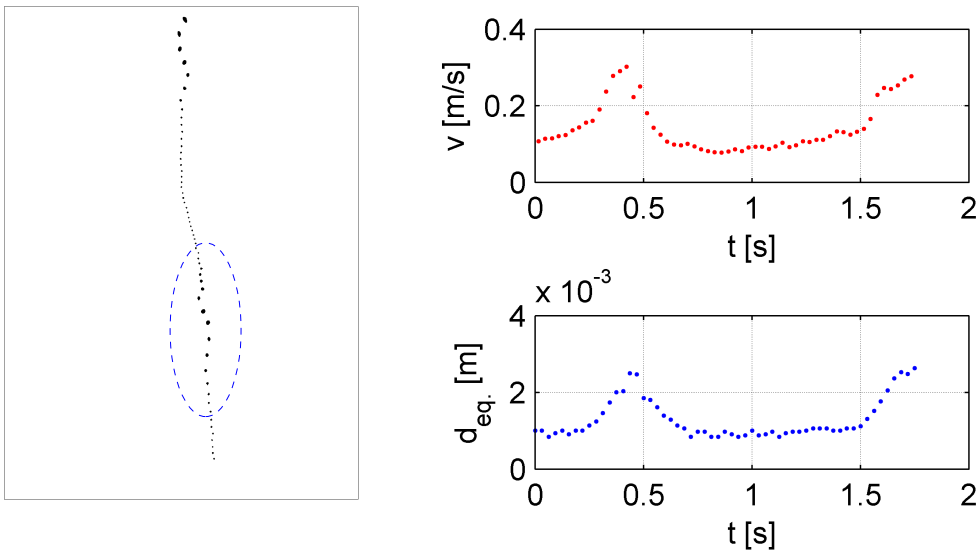

Fig. 3.4: Traced bubble showing spontaneous growth and subsequent shrinking

It is interesting that the bubble that re-shrunk does not condensate completely but moves on with smaller size, which indicates that this growth-/shrink effect may happen again. The incomplete condensation is believed to be caused by in-condensible gases that are solved from the water at the heaters' surface. The solubility of air in the water has a minimum at the boiling point which is present at the heater surface. The in-condensible solved gases are only slowly dissolved into the liquid again, so that these in-condensible gases reach the surface prior to that.

An image series of a geysering event is shown in Fig. 3.5. The created vapour quickly elevates and pulls hot liquid upwards which in consequence causes more vapour production. It becomes clear that during this event bubble coalescence and breakup is not negligible actually. However, this will not be considered in the modelling as the aim in this work is the initial dilute bubbly bulk boiling process. The flow pattern changes towards plug flow although seldom the whole cross section is filled by vapour. The image processing fails during such events, so that cross-correlation of the modelling is possible.

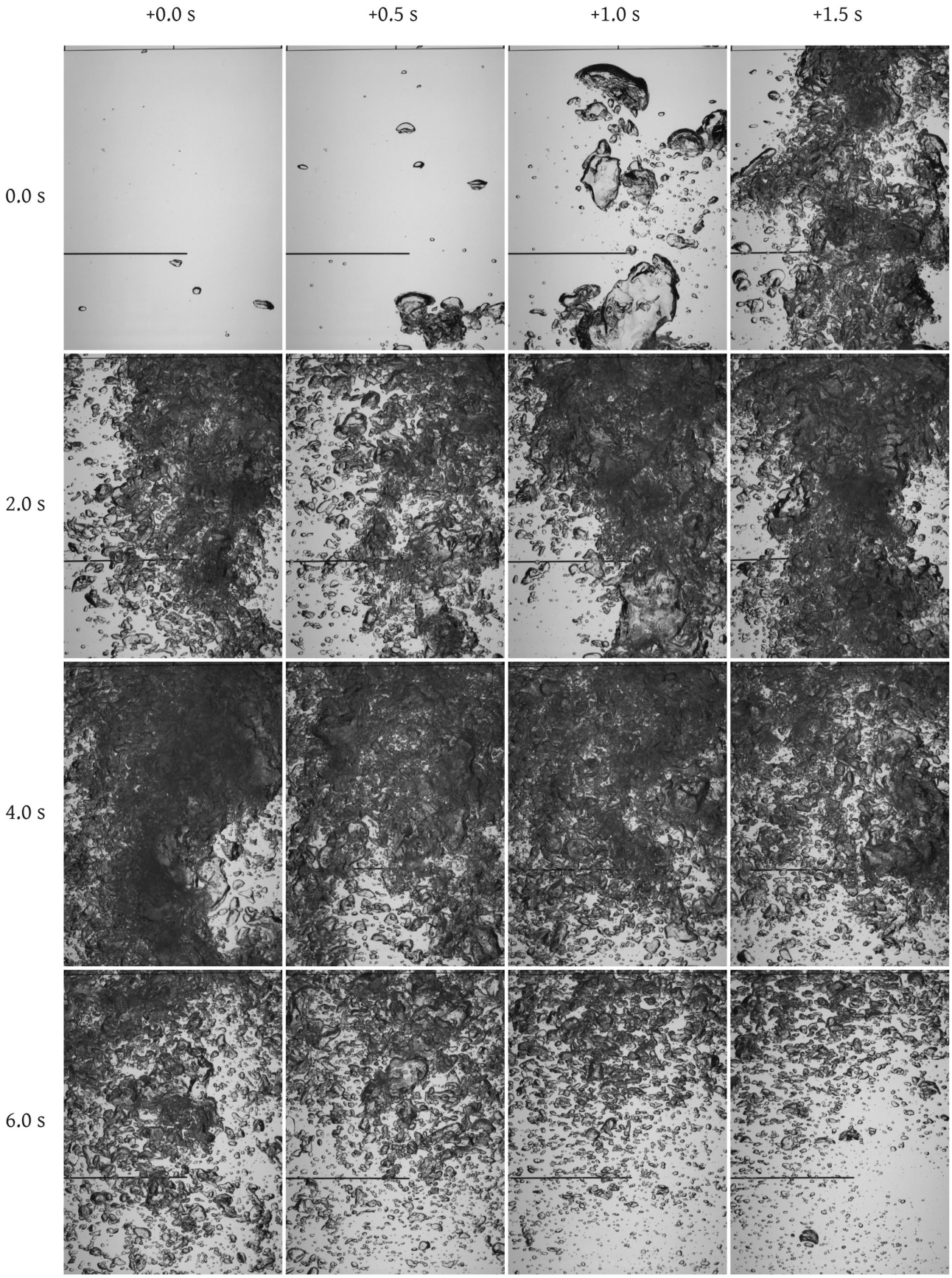

Fig. 3.5: Image series of a geysering event

3.3 Temperature Stratification

The temperature measurement is important to see how the temperature stratification inside the water column is. These values were investigated from all measurements that were conducted, which by far exceeds the length of the video recordings. In Fig. 3.6 the average temperature stratification is shown. The black line with the circles compares the measured temperature values with the saturation temperature according to the Antoine equation, which will be shown later in eq. (4.25).

It can be seen that the slope of the saturation temperature and the mean thermal layering are similar. There are events that exceed the saturation temperature slightly. These values are very low though and might be in the range of the measuring accuracy. It might as well be the case that there are no measured temperature values found that exceed saturation temperature. The temperature measurements are scarce and the the response time of the sensors is long. Another interesting question is how often temperatures higher than saturation are detected.

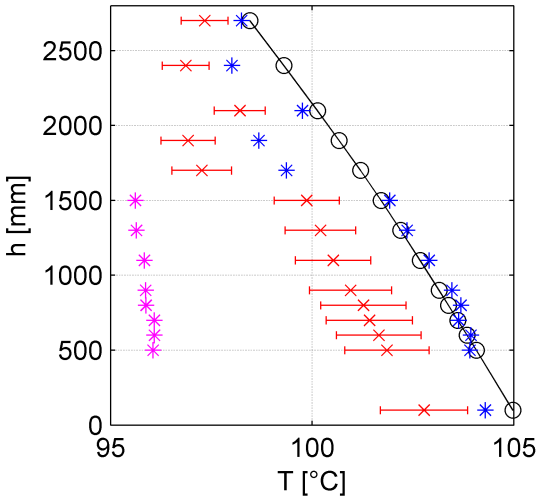

Fig. 3.6: Mean temperature (red cross) and standard variation (red bar) as well as minimum (magenta star) and maximum (blue star) values compared to the saturation temperature (black line and circles) with 119 °C heater temperature

In Fig. 3.7 the number of temperature measurements exceeding the saturation temperature for the operation with 119 °C heater temperature are shown. It can be seen that only in the lower mid part of the container the saturation is exceeded. The temperature stratification is important to know for a realistic initialisation of the temperature layering in the calculations. The results gathered from the resistance thermometers are consistent, but the thermocouples partly seem unreliable, at least in detecting the correct absolute temperature. The fact that no super-heating events were detected in the upper part of the container indicates the less reliable thermocouples. That can be seen by the non-linear behaviour of the mean

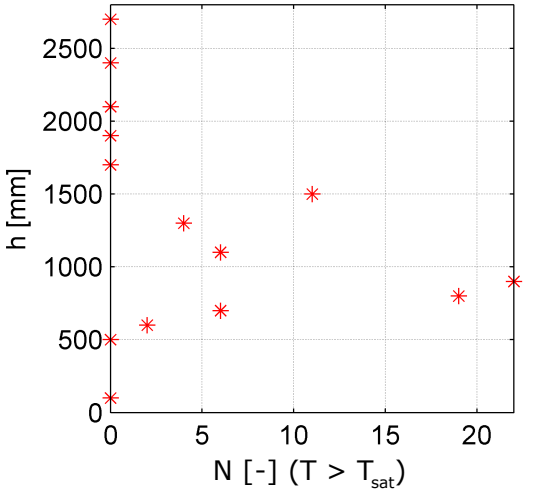

Fig. 3.7: Count of temperature measurements exceeding saturation temperature during operation with 119 °C heater temperature

temperatures. If only the resistance thermometers are considered the layering has a slope comparable to the saturation temperature. As the thermocouples measurements are inconsistent, the layering is considered to be linear and with the same slope as the saturation temperature.

3.4 Statistics of Instabilities

Two-phase instabilities occur during operation. These events are characterised by a local and sudden rise in vapour fraction. The high vapour fraction causes strong convection by big bubbles which are pulling hot portions of water upwards. An image series of such a geysering event was shown previously in Fig. 3.5. Hence the creation of vapour continues due to the release of latent energy until the water temperature drops below saturation in the whole container. This effect is commonly known as geysering. The geysering events are not directly useful for modelling but are discussed because of the observed decrease in temperature. For evaporation into a bubble energy is needed. The only energy available is from super-heating by pressure decrease. Therefore it takes super-heated liquid to evaporate into a bubble and due to evaporation the temperature of the liquid is reduced. This temperature decrease can be measured and is used to estimate the level of super-heating inside the volume. Later this will be relevant to one of the modelling parameters.

3.4.1 Frequency of Geysering Events

A Fast-Fourier analysis is conducted to investigate whether there is an geysering frequency present. Two measurements can detect an geysering event. First due to the increase in vapour volume the water level rises and therefore a pressure peak is registered. This measurement suffers from low increase in value and therefore causes problems in clear detection. The

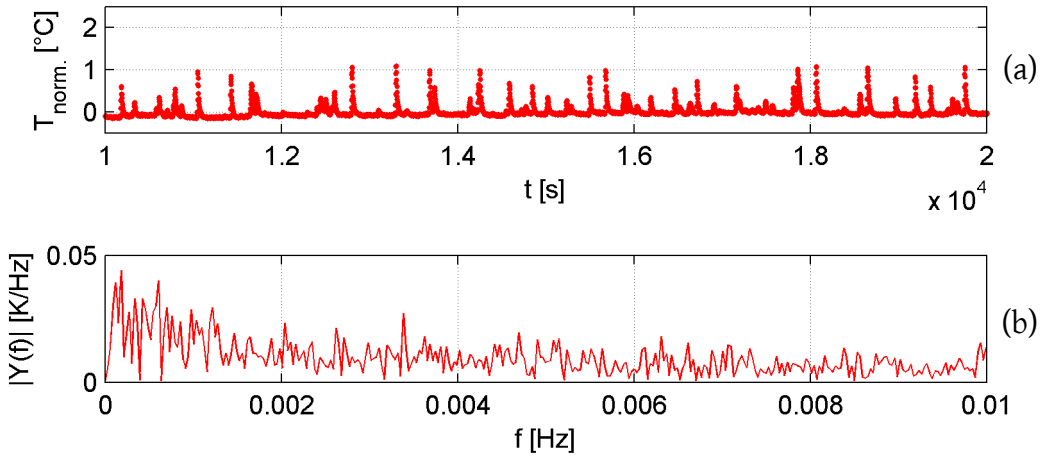

Fig. 3.8: Fast Fourier analysis of a temperature (T15) measurement: normalised time signal (a) and frequency signal (b)

secondpossible measurement value is the increase of the output temperature in the heat exchanger installed at the chimney. That effect is caused by the increase in condensed vapour volume. Considering these measurements it becomes clear that the temperature increase in the heat exchanger offers a more definite indication of an geysering event. Therefore when the normalised temperature signal has a peak higher that 0.5 K an geysering event is present (see Fig. 3.8a). As the measurement interval is 2 s, frequencies higher that 0.25 Hz are not detectable as this would not satisfy the Nyquist sampling theorem [102]. From observation the geysering events are usual apart several minutes. The conducted Fourier-transformation (see Fig. 3.8) shows no distinct peaks that would suggest a periodical behaviour. Therefore the instabilities are indicated to be irregular.

Another way to characterise the eruptions is to mind the time gaps Δt between geysering events G. Even if it is established that there is no geysering frequency there can still be a low variation in the time delay between eruptions. In Fig. 3.9 the time gaps between eruptions are shown for a measurement with 120 °C heater temperature. The time intervals vary strongly with the intervals $\Delta t \approx 137 \pm 101$ s, so it can safely be said that the behaviour is erratic in the experiment. As the there are no flow measurements and no frequently occurring events, the velocity initialisation for calculations is somewhat arbitrary.

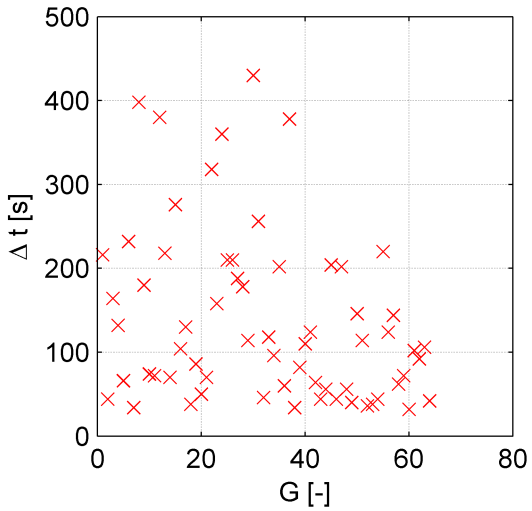

Fig. 3.9: Interval times Δt between Geysering events G

3.4.2 Temperature Decreases

During an geysering event, like discussed in the previous chapter, the bulk water temperature drops. As already described in chapter 2 the temperature measurements are done with low frequency. Therefore the fluctuating parts of the temperature cannot be measured with the used sensors. The temperature decrease is nonetheless of interest as it indicates the magnitude of the temperature decrease from locally supersaturated to saturated temperature. Later this parameter will be used for modelling. To evaluate the temperature decrease, first an geysering event needs to be detected and then the corresponding temperature measurements are considered. As before, the detection is done by finding temperature peaks in the temperature measurement at the cooling water secondary loop. Another possibility is the detection of pressure peaks in any

pressure transducer. The pressure peaks are very low and therefore more difficult to identify but the measuring frequency is about 6 Hz which is 12 times faster than the temperature measurement. The temperature peaks are very distinct and can be detected reliably. The corresponding temperature values from 10s before the peak to 20 s after the peak are considered. The maximum and minimum temperature are selected and the difference is the temperature decrease. The behaviour of the mean temperature during a geysering event is shown in Fig. 3.10.

Two ways of averaging are considered. First the temperature decrease of each measurement point is evaluated. It is visible that higher temperatures decrease and lower eventually increase. This is dependent on evaporation or condensation near the respective sensor as well as mixing processes. The temperature spread generally decreases. Upon averaging all temperature measurements inside the volume the average temperature decrease is calculated. This is a lumped parameter approach. These two ways of averaging yield different values for the super-heating, which are close in range though. The results of evaluation of 904 geysering events are shown in Fig. 3.11. It can be seen that the temperature decrease is in a similar range for all events. Upon consideration of the histograms of the temperature drops it is notable that they are in a quite distinguishable range but show no special distribution. The number of eruptions considered might be too small to go further into detail. Tab. 3.3 summarises the findings that are used for modelling.

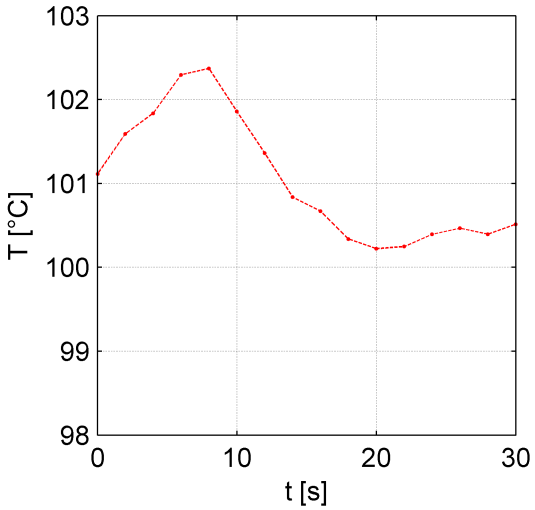

Fig. 3.10: Mean temperature measurement during an geysering event

Tab. 3.3: Measured water temperature drops during geysering events

Ave. Temp. decrease	Std. deviation	Local ave. temp. decrease	Std. deviation
0,8 [K]	±0,3 [K]	1,6 [K]	±0,5 [K]

The values shown in Tab. 3.3 are an estimate of the water temperature decrease during an geysering event. That means it is a indirect measure for the super-heat that is present during a geysering event. As the values are averaged and fluctuations are not measured, the significance is minor, but still the range of 0.5 K to 2 K of super-heat is reasonable and therefore outlines a good starting value range for the simulation model.

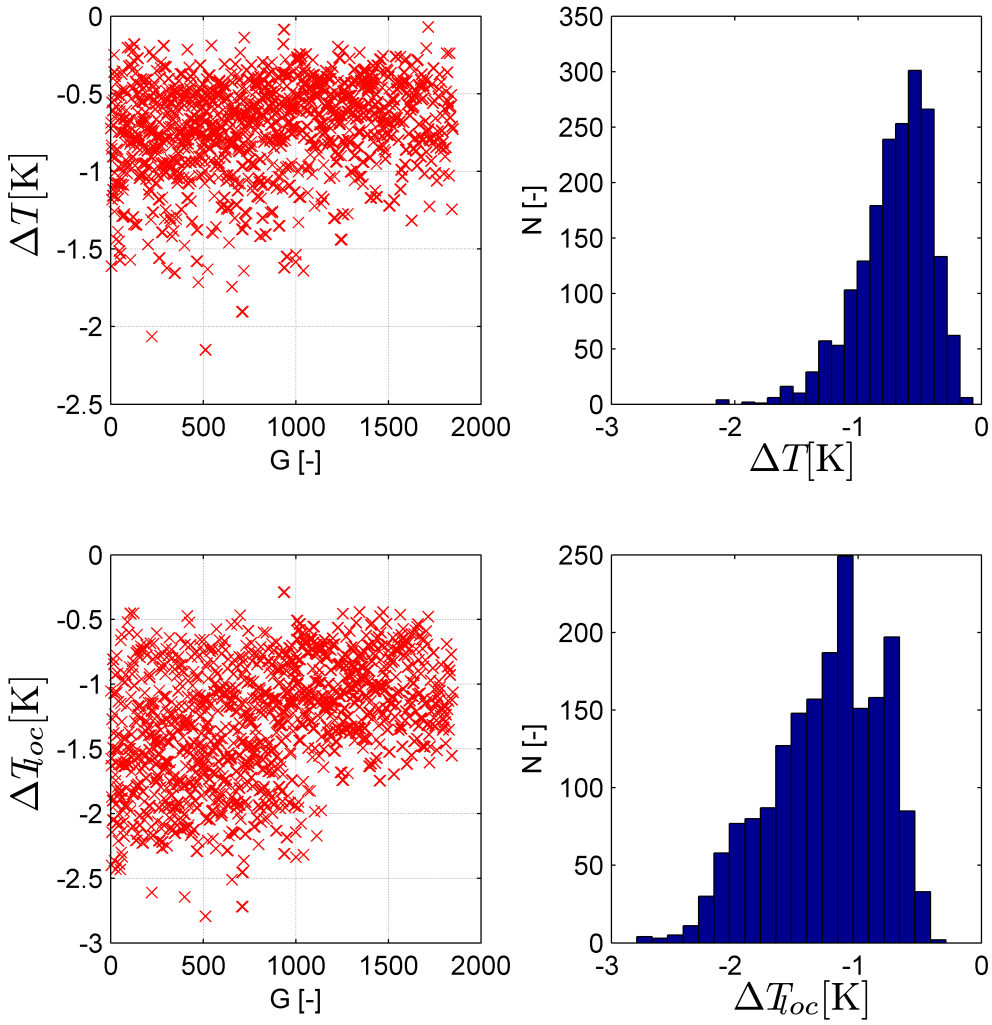

Fig. 3.11: Measured temperature decrease after geysering events

3.5 Bubble Properties

This chapter will present the most important measurements concerning the bubble size distributions observed and the statistical and transient behaviour of the bubble number density. Some additional aspects that were investigated, like bubble shape and velocity, are shown as well.

3.5.1 Bubble Shape

The measurement is a projected view of vapour bubbles and any statement for spheres is an

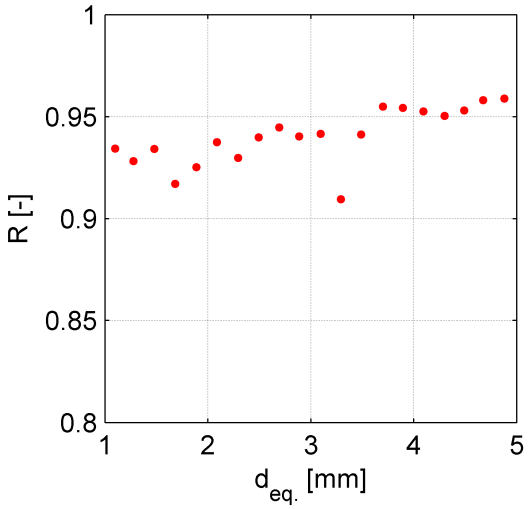

Fig. 3.12: Estimated roundness for bubbles up to 5 mm eq. diameter

extrapolation from the projected 2D view.

It is commonly observed that bubbles beyond a certain size begin to deviate from spherical shape. This is usually associated to the increasing relative velocity to the liquid and the lower internal pressure of the bubbles as a consequence of lower surface tension forces. The surface tension forces thereby decrease the less the curvature of the surface is. This chapter evaluates the parameters roundness and eccentricity of the detected bubbles. Unfortunately the results from the 1st measurement campaign are unreasonable and the cause is unknown. The results from the 2nd measurement campaign are consistent, although the number of evaluated bubbles is lower. Judging from the roundness criterion bubbles of up to 5 mm equivalent diameter have a roundness value near 1 which indicates a low deviation from spheric shape (see Fig. 3.12).

The eccentricity however has a somewhat strange behaviour as the values are in the range of 0.3 - 0.5 and declining with size. That would mean the bigger the bubbles the smaller the eccentricity. To illustrate the difference in the values of eccentricity a circle and perfect ellipses were drawn with increasing eccentricity and previously shown in Fig. 2.8. It can be seen that the values deviate quickly from the value 0 that corresponds to a perfect circle. The eccentricity seems to suffer from the relatively low number of pixels in small image objects. As the value depends on the squared ratio of the of the foci distance and its major axis length small discrete values worsen the estimation.

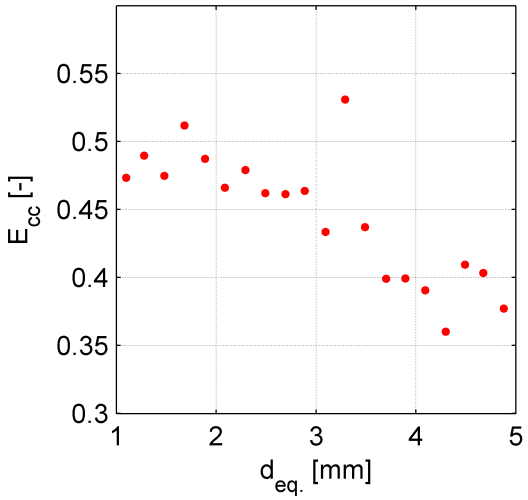

Fig. 3.13: Estimated eccentricity for bubbles up to 5 mm eq. diameter

As the eccentricity stays low with higher bubble diameters there is little concern that smaller bubbles would be more eccentric. The results do not indicate strong deviation from roundness for bubbles with a diameter $d_b < 5$ mm and therefore the usage of spherical bubble shape in the modelling approach is reasonable.

3.5.2 Bubble Size Distribution

The bubble size distribution shows the same qualitative behaviour in all measurements. The relevant data are gained from the measurement campaign 1 and 2. In the measurement campaign 1 the bubble size ranges from 1-10 mm in equivalent diameter. The second measurement campaign looks more into detail by measuring the bubble from 0.1-1 mm equivalent diameter. The bubble sizes were grouped in 0.1 mm diameter steps. In a double logarithmic diagram the

distribution is linear and in all cases with little variation in slope. For an overview of the size distributions measured during the 1st measurement campaign the imaging positions 2-6 are all plotted in Fig. 3.14.

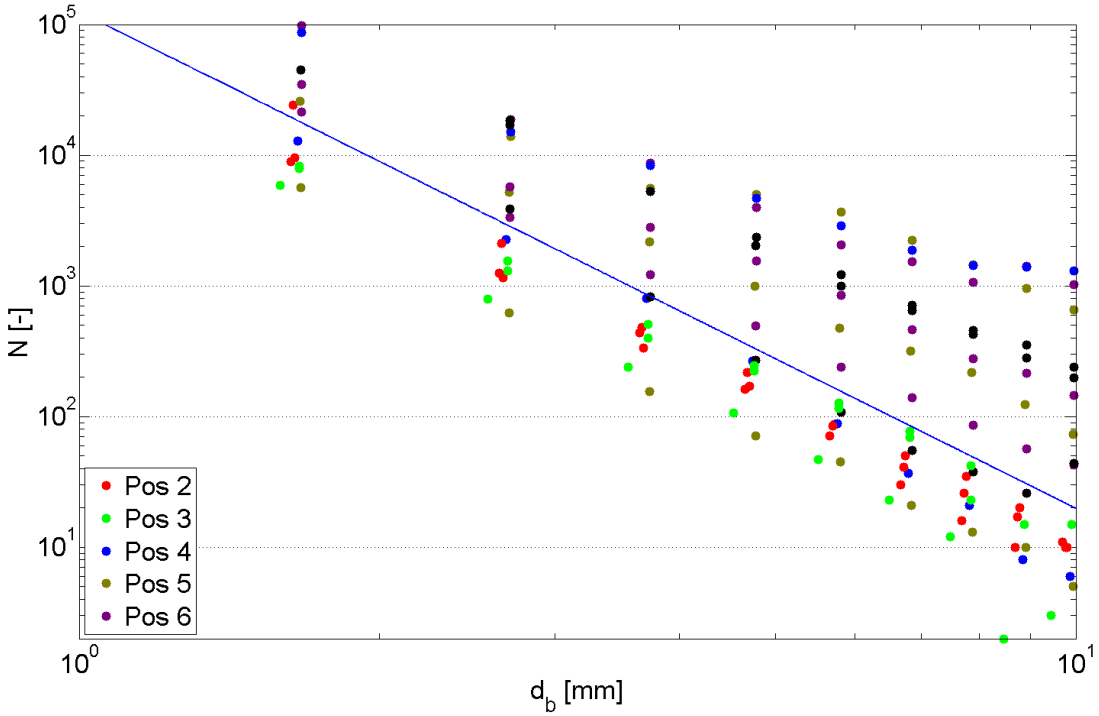

Fig. 3.14: Overview of bubble size distributions (1st campaign, all heater temperatures) and estimated slope of the distribution (blue line)

It is evident that although the magnitude is varying the slope stays relatively constant. That way the distribution can be described be the exponential law given in formula (3.1).

$$N = a_{dist} \cdot d_b^{b_{dist}} \tag{3.1}$$

The exponent b has been ranging between -4.8...-2.8, whilst a_{dist} is estimated to be 33000...140000 in the 1st measurement campaign. The mean values resolve to b_{dist} = -3.7 and a_{dist} = 60000. In the 2nd measurement campaign b_{dist} ranges from -5.0...-4.0 and a_{dist} is 0.0065...3.65. resulting in a average values of b_{dist} = -4.6 and a_{dist} = 1.9. However that is estimated from only 3 curve fits, as the distribution is less clearly linear due to fewer measurements and curve fitting only succeeds in 3 positions. The changes in magnitude are not correlated to the position linearly. They are in fact dependent on the imaging section and the measurements temporal length. Therefore only the slopes' exponent is of interest for the distribution. Using all slopes evaluated, the size distribution resolves to $N = a_{dist} * d_b^{-3.8}$ (see blue line in Fig. 3.14). The bubble number distribution is not moved upwards with the position, but the most bubbles are in the region of image section 4 (Pos 4).

In comparison the distributions of the 1st and 2nd campaign are plotted in the same diagram to

visualise the slope (see Fig. 3.15). It can be assumed that the less linear distribution in the measurement campaign 2 is because of fewer bubbles measured. The absolute value of detected bubbles in that diagram is not of relevance as it depends on the total number of detected bubbles which, in turn, depends on the measuring time and image section size. For better presentation of the results the measurements are normalised by the total bubble number in each measurement.

The only significant deviation from that distribution is in the range below 1 mm bubble diameter. In Pos 4 the bubble distribution has a peak in the range of 0.5 mm diameter.

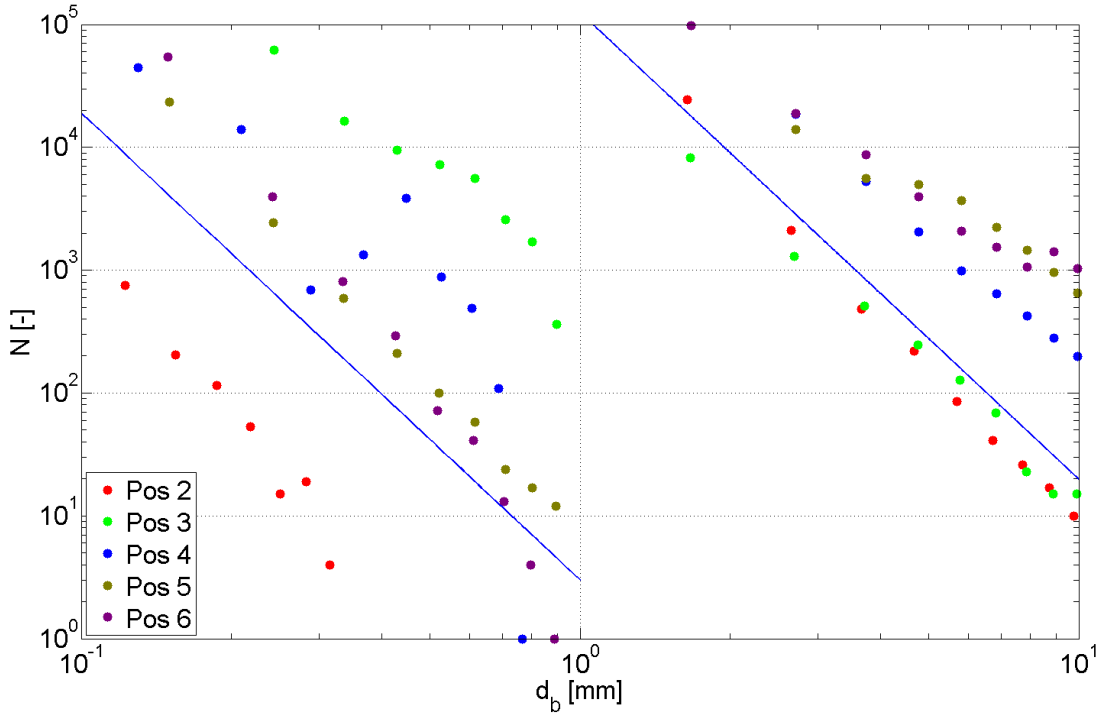

Fig. 3.15: Bubble size distribution for different measuring ranges (0.1-1mm and 1-10mm)

3.5.3 Bubble Number Density

To calculate the bubble number density the measured volume is to be determined first. The measured volume is of the shape of a truncated pyramid (see Fig. 3.16). From the measured distances x,b and D, and the aspect ratio of the image, all remaining lengths and the volume can be calculated. The resulting volumes for the two different imaging sections are shown in Tab. 3.4.

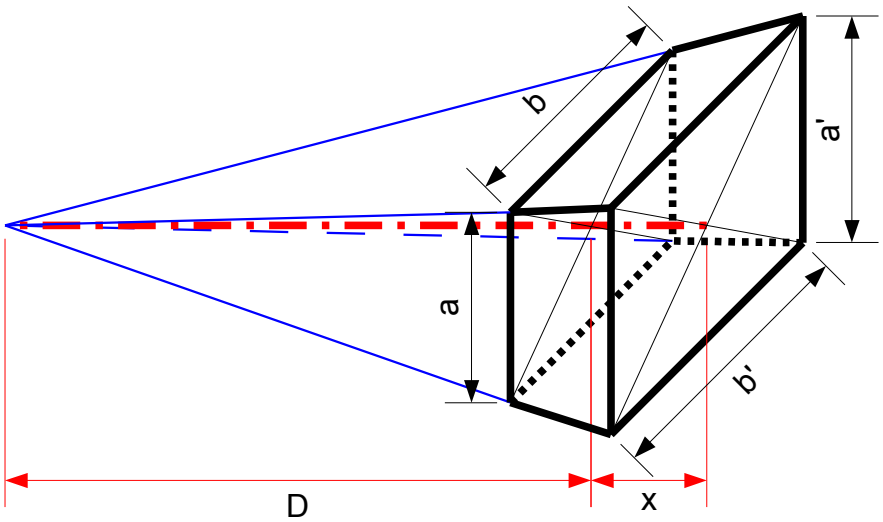

Fig. 3.16: Illustration of the measured volume

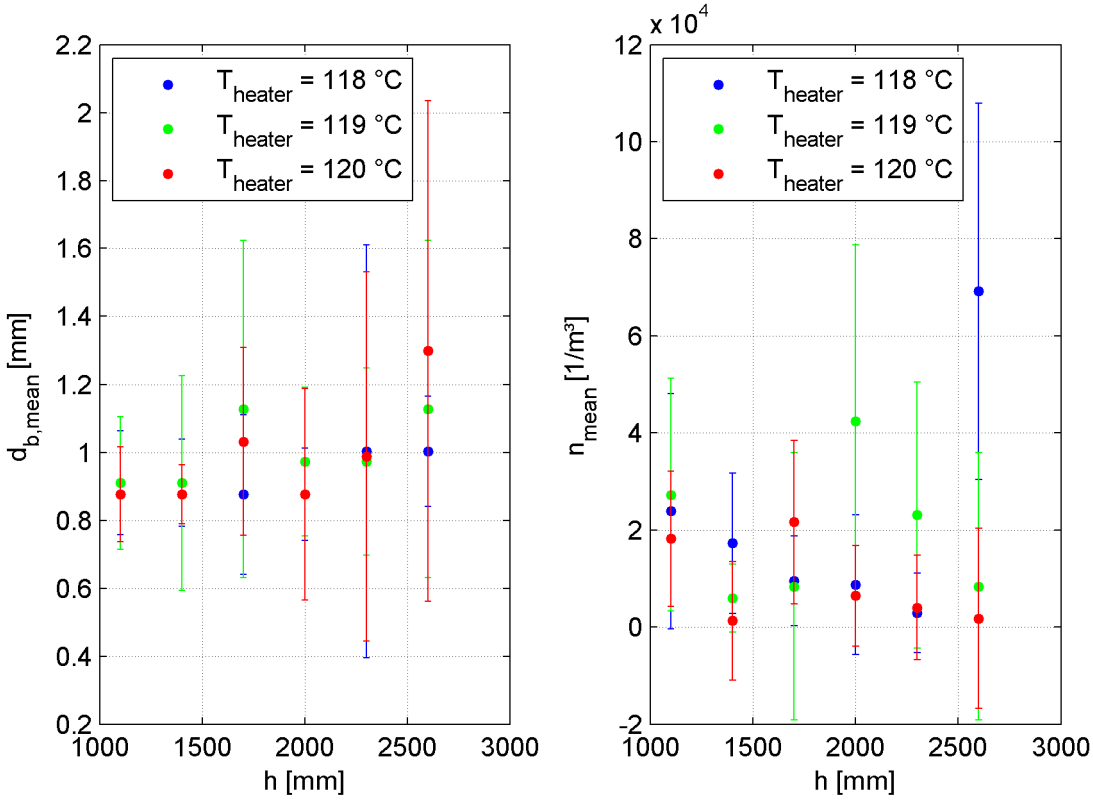

Fig. 3.17: Mean bubble diameters and number densities

Tab. 3.4: Measuring volumes in the respective campaigns

		1st Campaign (20x28)	2nd Campaign (6x8)
Measuring volume	[mm³]	6201691	713975

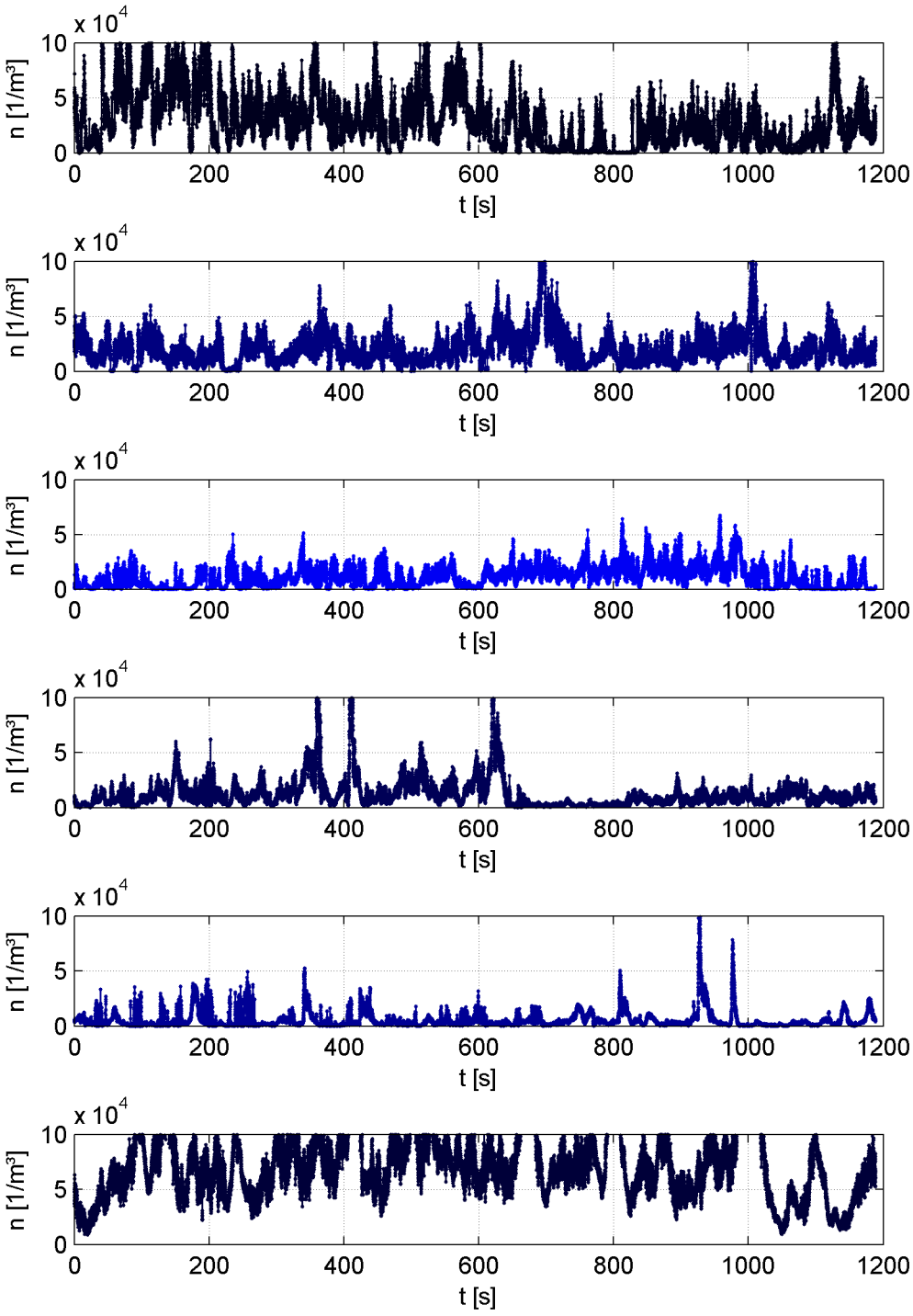

Fig. 3.18: Measured bubble number density n at all six positions (not simultaneous, T_{heater} = 119 °C)

The measured bubble number changes constantly. Single peaks arise, but cannot be correlated with temperature peaks that indicate a geysering event. The transient behaviour of the bubbles

number density is shown in Fig. 3.18. The bubble number density changes over several orders of magnitude and mostly ranges from $n = 0 - 10^5$ [1/m³]. Only single peaks occur that are much higher than that value. The rate of the changes of this value is high so that steep increases and decreases are regular.

The transient behaviour makes it difficult to find a suitable method to describe the behaviour. The location of the initial bubble generation moves and therefore for the pressure peak to coincide with the sudden rise in number density the visualisation area needs to be in the right position. Therefore either far more measurements would be necessary for statistical agreement or all imaging sections need to be filmed simultaneously. That way not only the peak but the position of the origin of the instability could be correlated.

Therefore a statistical evaluation is done in the following. The number density average value that has been measured in the test set-up is 16680 m^{-3}. The standard deviation from that value has been calculated and the average values at the various heights as well as the standard deviation are shown in Fig. 3.17.

These values can be considered to be first hints towards a suitable modelling. Looking further into detail, the probability density of the bubble number density can mostly be fitted well using a log-normal distribution. From that fit the expectation value E and standard deviation σ can be calculated which are as well possible values for modelling. From the log-normal fit the expectation values E were determined to be between 5432 m^{-3} and 75808 m^{-3}. The standard deviations are between 8247 m^{-3} and 97537 m^{-3} (see Tab. 3.5 and Fig. 3.19).

Tab. 3.5: Parameters of the log-normal bubble number density distribution

E_x	Pos. 1	Pos. 2	Pos. 3	Pos. 4	Pos. 5	Pos. 6
118 °C	40756	21586	13986	12364	5432	75708
119 °C	42558	9199	16992	51692	31071	16992
120 °C	24825	7063	25534	10673	8135	8258
σ	Pos. 1	Pos. 2	Pos. 3	Pos. 4	Pos. 5	Pos. 6
118 °C	97537	21887	27072	13981	8247	41097
119 °C	79150	17149	27328	48372	35875	27328
120 °C	36592	25800	22350	17008	12699	27703

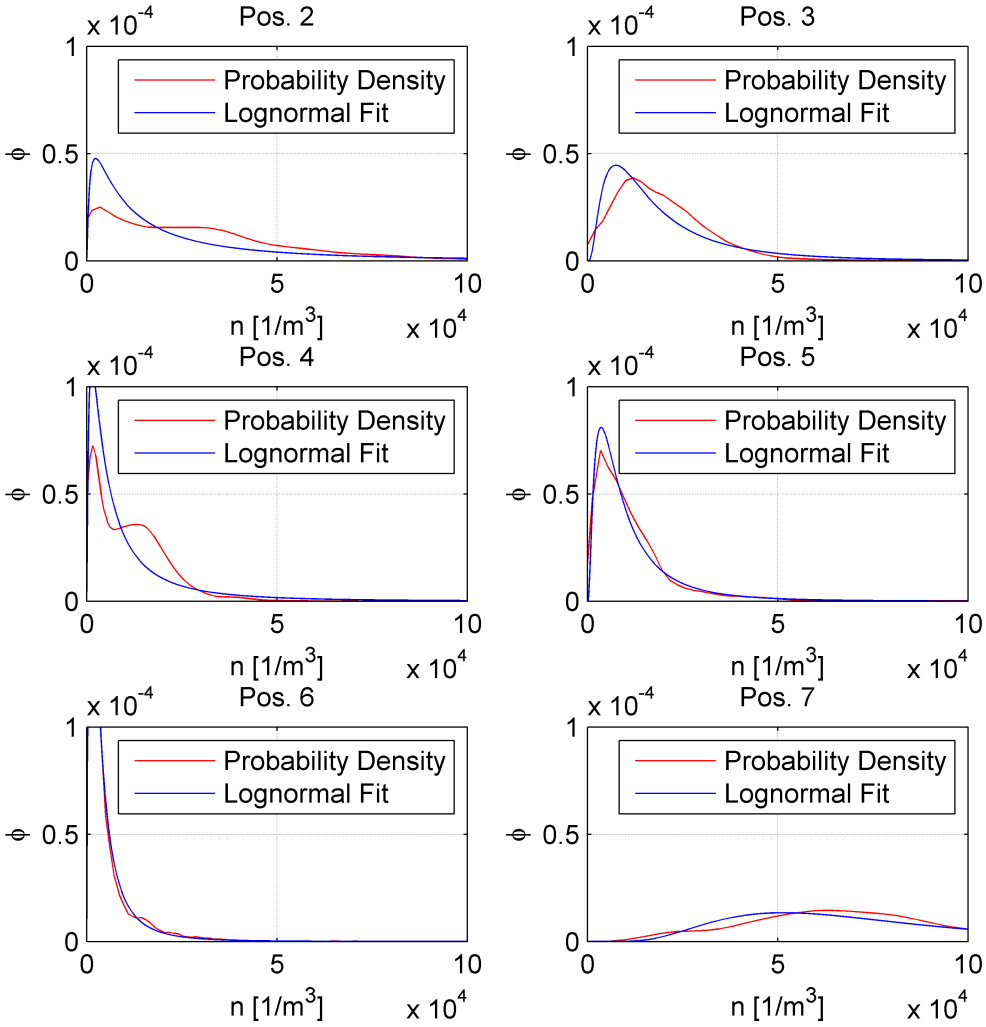

Fig. 3.19: Bubble number density distributions' probability density Φ fitted to a log-normal distribution

No matter what point of view the bubble number density is changing over several orders of magnitude. Hence, it is to be expected that the standard deviation is high. To ensure the bubble number density does not depend on the vapour fraction, the bubble number density was split into vapour fraction groups to consider the change in probability density Φ. It remains constant in all groups. Therefore, no or only slight dependency of the bubble number density on the vapour fraction can be determined. This is presented in Fig. 3.20.

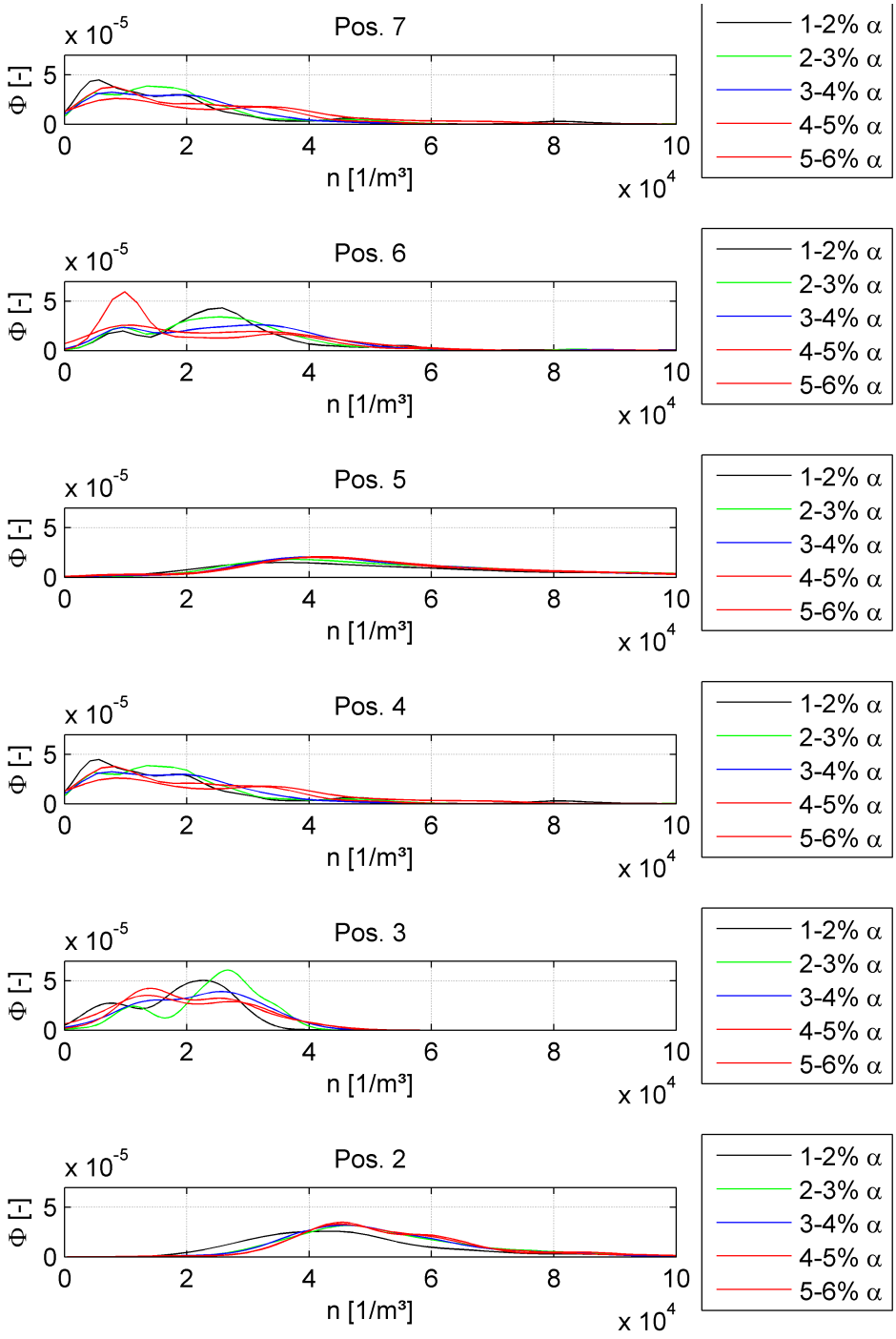

Fig. 3.20: Correlation between the bubble number density distribution and the vapour fraction

3.5.4 Vapour Fraction

After the bubble's detection and the subsequent estimation of the equivalent diameter $d_{eq.}$, it is possible to calculate the equivalent volume of all bubbles. It has been discussed earlier that the roundness of bubbles does not deviate much from spherical shape.

For a perfect unit circle several ellipses with increasing eccentricities but the same equivalent diameter are used to calculate the volume of the corresponding rotational bodies. The result is shown in Fig. 3.21. For the same equivalent diameter the volume of the rotational body keeps increasing. An eccentricity value of 0.5 spawns a

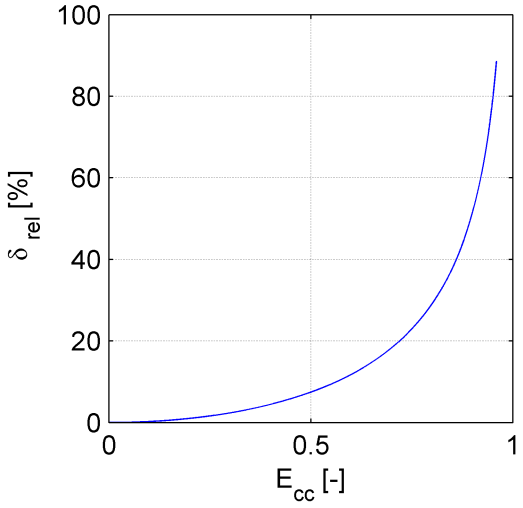

Fig. 3.21: Error in volume estimation due to eccentricity

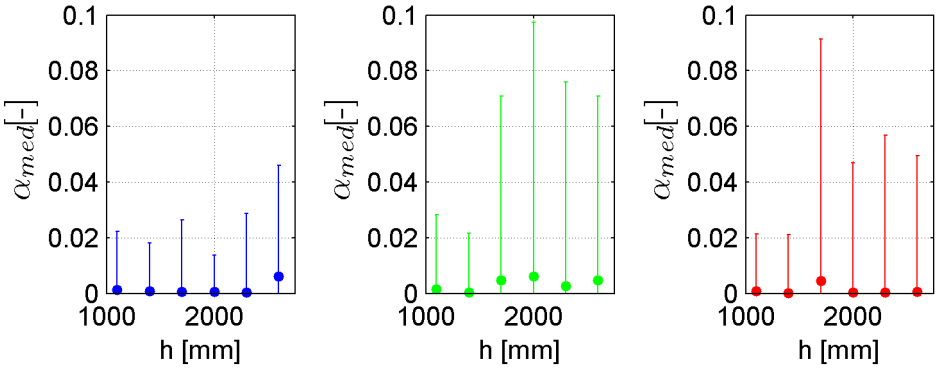

Fig. 3.22: Average vapour fraction during measurement (left: 118 °C, center: 119 °C, right: 120 °C)

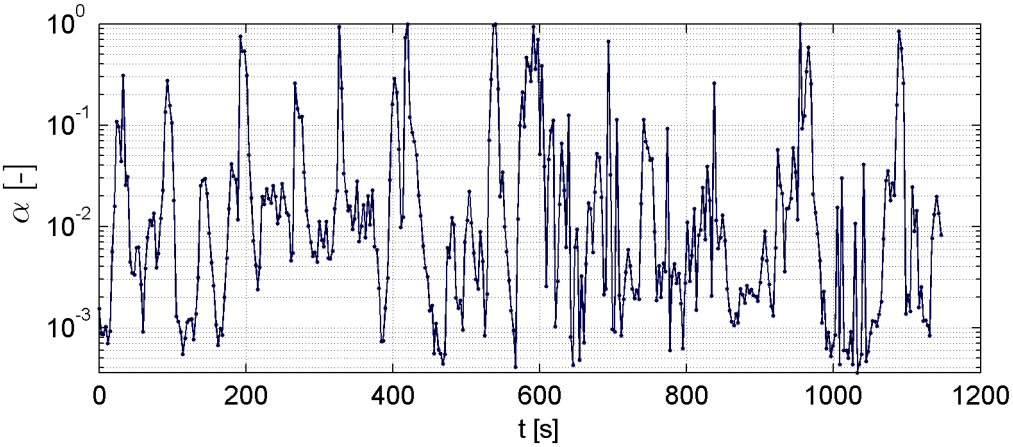

Fig. 3.23: Transient behaviour of the vapour fraction (position 3 in the 119 °C measurement)

relative error in Volume of 7.5 %. In the previous section the measured volume was determined

and so the vapour fraction can be estimated. An interesting value is the average vapour fraction detected to see if the flow is really dilute bubbly flow. That is because with higher vapour fractions coalescence and breakup are more likely dominant effects. The median values are mostly in the range of a few percent (see Fig. 3.22). If the standard deviation is used as a measure for the range in which the vapour fraction usually is, it seldom exceeds 10 %. Therefore it is appropriate to consider the flow as bubbly and dilute.

The transient behaviour can be seen in Fig. 3.23. It becomes clear that even though there are events of a local high vapour fraction, most of the time the values are in the range from 0.1 % to 10 % volume fraction.

Overall it can be concluded that the vapour fraction is in a reasonable value range for the assumption of a dilute bubbly flow pattern. Single events of local high vapour fraction are observed but only for a short time. Therefore, statistical values are not affected.

3.5.5 Bubble Velocity

The bubble velocity is measured from fully traced bubbles, that were captured at an increased frame rate (i.e. 72 fps). As the velocity results from the movement of the the objects centre between two frames, the average bubble size in these two frames is considered bubble diameter. As the water velocity is unknown the measured velocity is not the relative velocity between the phases. For each traced and distinct bubble the displacement and equivalent diameter is measured. By averaging the equivalent diameter between two frames the diameter is determined. The displacement between two frames and the frame rate are used to calculate the average velocity. Using this method approximately 600000 single data pairs are at disposal. To evaluate the data size groups are defined ranging from the equivalent diameter 0.3 mm up to 10.1 mm using 0.2mm steps. All bubbles that are in the range of a size group are then averaged in size and velocity. For every size group at least 1000 values are used. Clift et al [101] show a diagram for the terminal velocity of air bubbles rising in water. For comparison with this well-known data, the measurements are plotted against Clift's result in Fig. 3.24. The overall behaviour of the vapour bubbles in the measured region is close to being linear. At roughly 1.5 mm bubble size, the measurement matches the water/air mixture shown. After that the vapour bubbles rise with higher velocity. When the same diagram is considered using the Eotvos number *Eo* (see Fig. 3.25) the rising velocities are nearly identical with a tendency of higher vapour velocity with bigger diameters. This suggests that the different vapour density and surface tension are responsible for the differences with small bubble diameters and later the deformation of the vapour bubbles differs from that of air bubbles. Comparing water/air and water/vapour, the density and surface

tension is lower for the water/vapour system.

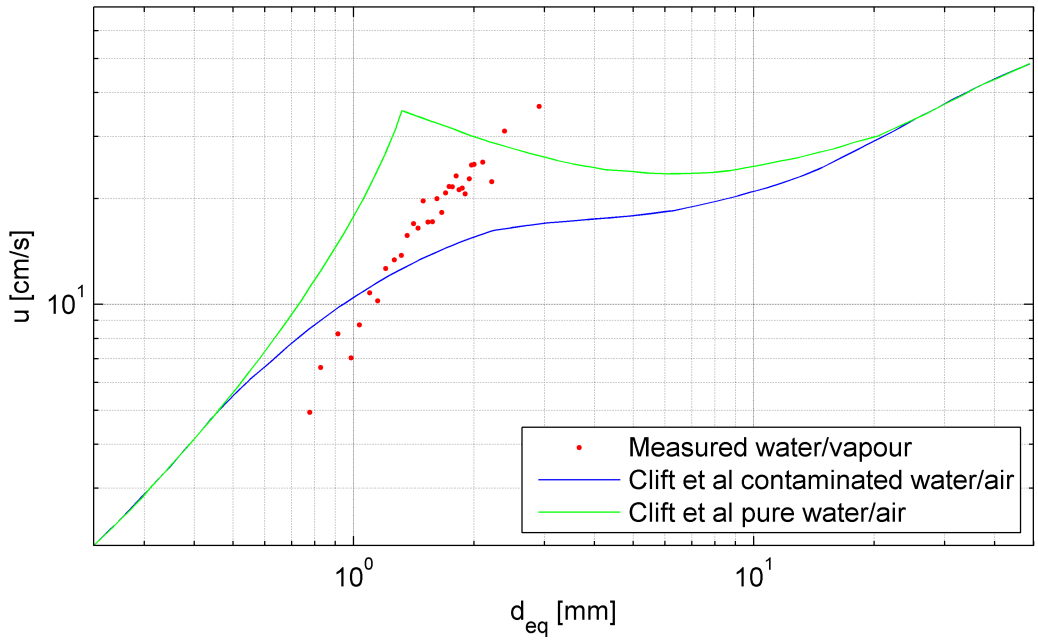

Fig. 3.24: Comparison between the terminal velocities of bubbles

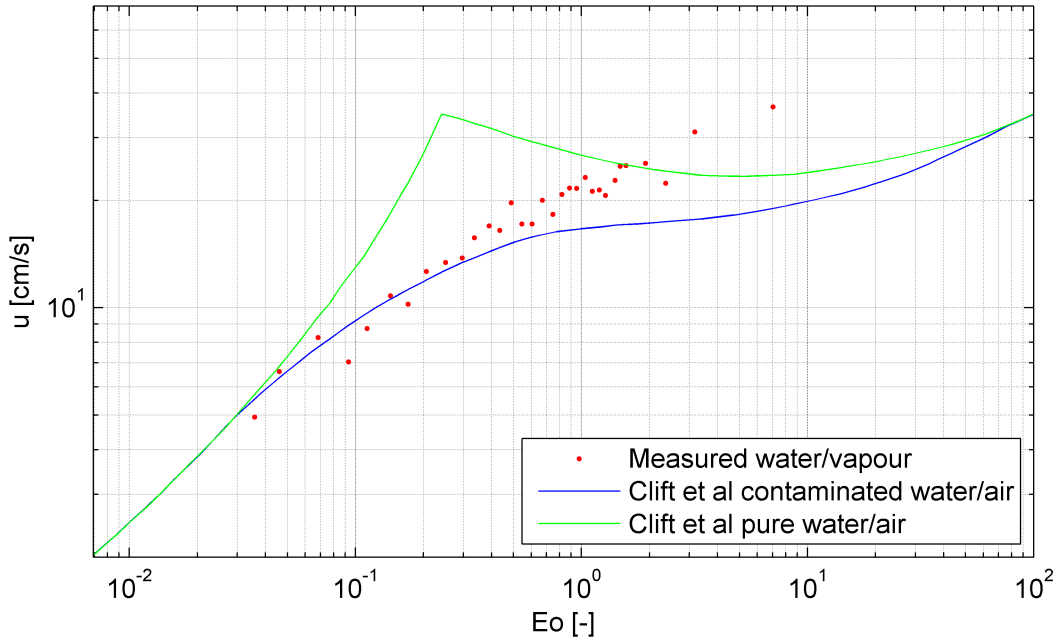

Fig. 3.25: Dimensionless presentation of the measured terminal velocities of bubbles

3.6 Summary and Interpretation of the Experimental Results

There are several findings resulting from the experiment that are relevant to the development of an underlying mechanism.

First of all it is necessary to incorporate the possibility to change the bubble number as well as the bubble sizes locally. It has been established that the bubble number varies over several orders

of magnitude during operation. The growth/shrink mechanism for obvious reasons needs changing bubble sizes but not necessarily changing bubble numbers.

The bubble number distribution shows an exponential decrease in bubble number probability with increasing size. Therefore a virtually unlimited supply of micro-bubbles can be assumed. The measured bubble number density can only change if more bubbles grow to a visible size. The amount of available evaporation energy determines the amount of vapour that can actually be generated. The amount of energy available is located in the latent heat temporarily stored in the current local super-heating of the liquid. Only with higher super-heating smaller bubbles can begin to grow as their saturation temperature is increased by the surface tension.

Most of the time the average bubble diameter is approximately 1 mm, which is not surprising considering the bubble size distribution. The bubble number density keeps changing all the time mostly within $0 - 10^5\ m^{-3}$ bubble number density and a few but very high peaks. These peaks have extremely high value and are existent for a very short period of time. The influence on the basic mechanisms therefore is considered to be negligible.

In this test set-up the average bubble number density n = 16680 $1/m^3$, which will be directly incorporated into the model as well as the previously mentioned range in which the transient values are.

Another boundary has been evaluated from the identification of instabilities and the connected temperature decreases in the liquid. The measured temperature decreases are in the range of 0.5 K ... 2 K. This is assumed to be the amount of super-heating that is present before a geysering event.

For later initialisation purposes of the simulation the thermal layering was considered. The average temperatures have a linear distribution a few degrees below the saturation temperature. The bubble velocities are in a range of up to 0.3 m/s as the velocities of the traced bubbles show. The water velocities were not measured, which makes initial water velocities a somewhat arbitrary choice that will be in the range of 0.1 m/s ...1 m/s. It is well possible that high water velocities will cause thermal mixing which might suppress hot plumes to reach super-heating.

The measured vapour fractions during the experiments are usually in the range of 0.1 % ...10 %, but can be exceeded for short periods in time. Therefore dilute bubbly boiling is present most of the time.

4 Mechanistic Modelling

This chapter will define the proposed algebraic pool boiling model and show the required physics incorporated as well as the mechanism. The basic procedure to do a numerical flow simulation is given by Laurien and Oertel [103]. The chapter will be structured accordingly.

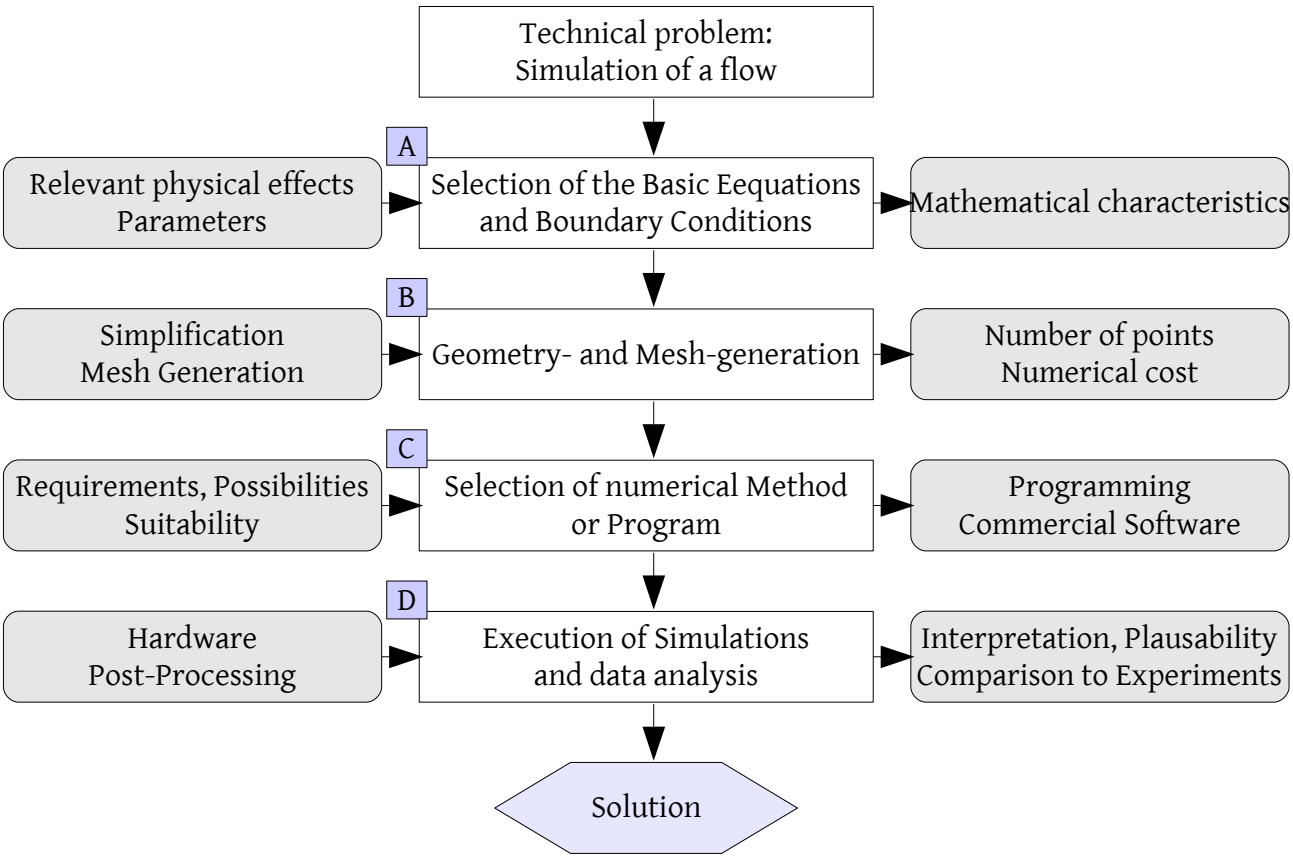

Fig. 4.1: Basic procedure towards execution of a numerical flow simulation [103]

The problem at hand is a two-phase flow simulation that needs to be classified. Here the system consists of a dispersed gas and a continuous liquid, both being water. There is no free surface to be considered and the (measured) vapour fraction was low (< 10 %). Therefore a two-phase single component dilute bubbly boiling problem is to be considered.

That means a simulation of the original geometry of the test set-up with comparable boundary and initial conditions will be performed with the mechanistic model that will be proposed in this chapter. The simulation should reproduce the identified mechanisms and later a quantitative comparison is considered.

After the technical problem is defined the fundamental equations and boundary conditions need to be considered. Then the geometry and meshing is performed and a numerical method or

program is chosen. The steps B and C are self-explanatory as the geometry in the experiment is cuboid and in this work the commercial code Ansys CFX is used. The code was chosen for various reasons. Programming a numerical solver was outside the time-scope of the work and the commercial code CFX is suited and available. The meshing will be discussed later in the grid advection study. Upon computation and and post-processing the solution is to be interpreted and compared to the experiment. The following sub-chapters will discuss the fundamental equations and the boundary conditions, as well as the proposed model based on the experimental findings.

4.1 Integration Domain, Boundary- and Initial Conditions

4.1.1 Basic Calculation Set-up

The following section will show the used basic simulation set-up for all of the calculations. Any changes to these basic settings will be explained in the respective sections. The various settings will be shown in separate tables.

The boundary conditions are mostly identical with the surrounding faces (SIDEWALL / BOTTOM) and bottom face being smooth adiabatic no-slip walls. The top (OUT) is defined as an opening having an outside temperature slightly above saturation and a constant pressure of p_{ref} = 101325 Pa. The opening is set to 100 % vapour fraction, so only vapour may be re-entering the domain, but water can only exit it. The front- and back-side (FRONT / BACK) of the container are set to translational periodicity (see Fig. 4.2). Later calculations representing the experimental set-up the bottom is a heated wall instead of being adiabatic. There is no water inlet used because the transient calculation times are relatively short. The loss of mass passing the outlet (vapour) is small over such calculation times and the change in the water level is negligible. By default the wall contact model uses the contact area fraction of phase α at the wall that is identical to the volume fraction in the control volume adjacent to the wall. The whole set of boundary settings is summarised in Tab. 4.1.

Tab. 4.1: Boundary settings in the calculations

TOP	[-]	Opening
Flow regime	[-]	Sub-sonic
Mass and Momentum	[-]	Opening pressure and direction
Relative pressure	[Pa]	0
Flow direction	[-]	Normal to boundary condition
Turbulence	[-]	Medium intensity (5%)
Opening temperature	[K]	374.15
Vapour fraction	[-]	1
Water fraction	[-]	0
SIDEWALL / BOTTOM	[-]	Wall
Wall velocity	[m/s]	0
Roughness	[-]	smooth
Heat transfer	[-]	Adiabatic/Constant Heat Input
Wall contact model	[-]	Use volume fraction
FRONT / BACK	[-]	Translational periodicity

The problem can only be described by a transient calculation as the process is not stationary. During calculations with adapting time steps the range is 10^{-5} s to 10^{-3} s, mostly ranging between 10^{-5} and 10^{-4} s. This is the cause for long calculation times as the transient times are in the range of several seconds. The number of iterations per time-step is set to be between 2 and 10, and the time adaptation changes the time steps so that 4-6 iterations are achieved. The initial time-step is set to 10^{-5} s and can be increased up to 10^{-2} s. The increase factor is 1.05 and the decrease factor is 0.8. An overview of theses settings is given in Tab. 4.2.

Tab. 4.2: Time-stepping used in the calculations

Analysis type	Time-step	Initial Time-step	Adaptive Time-Step	Target Loops	Time-Step increase factor	Time-Step decrease factor
[-]	[-]	[s]	[s]	[-]	[-]	[-]
transient	adaptive	10^{-5}	10^{-5} – 10^{-2}	2-6	1.05	0.8

The continuous phase is liquid water and the dispersed phase is vapour (water in gaseous state). The water phase is defined by the IAPWS - IF97 (The **I**nternational **A**ssociation for the **P**roperties of **W**ater and **S**team - **I**ndustrial **F**ormulation **97**) in a temperature range from 273 K to 623 K and a

pressure range from 10^3 Pa to 10^7 Pa. The vapour phase is as well defined by the IAPWS - IF97 but in a temperature range from 273 K to 550 K and the pressure ranging from 10^4 Pa to $2x10^5$ Pa using 150 sampling points. The material properties are summarised in Tab. 4.3.

Tab. 4.3: Material properties used in the calculations

	Name	Definition	Morphology	Temperature range [K]	Pressure range [Pa]	Sampling points	Particle diameter
Water	Water1	IAPWS - IF97	continuous	273 – 623	10^3 – 10^7	100	-
Vapour	Steam3	IAPWS - IF97	dispersed	273 – 550	10^4 – $2x10^5$	150	boiling

As the flow velocities are relatively small with natural convection the thermal energy model is used instead of the total energy model. For turbulence modelling, the k-ε-model with scalable wall function is used for the liquid water and the "dispersed phase zero equation" turbulence model for the vapour. The fluid pair model describing the drag between the phases is the particle model using the Schiller-Naumann drag as stated earlier. The buoyancy is calculated using the density difference with the reference density ρ_{ref} = 958 kg/m^3 which corresponds to liquid water at the boiling point and the gravitational acceleration is g = -9.81 m/s^2. For mass transfer the thermal phase change option depending on the increased saturation temperature as defined in (4.9) is set. Any heat transfer directly causes mass transfer according to the the amount of energy transferred and the evaporation enthalpy. For the heat transfer the two resistance model with zero resistance on the vapour side and the Ranz-Marshall model on the water side is used. The bubble diameter is calculated locally using the boiling model that was presented earlier. All other options are as the default setting except that the phases are calculated as coupled. The solver settings will be shown later as they were determined by an advection scheme study and a grid study.

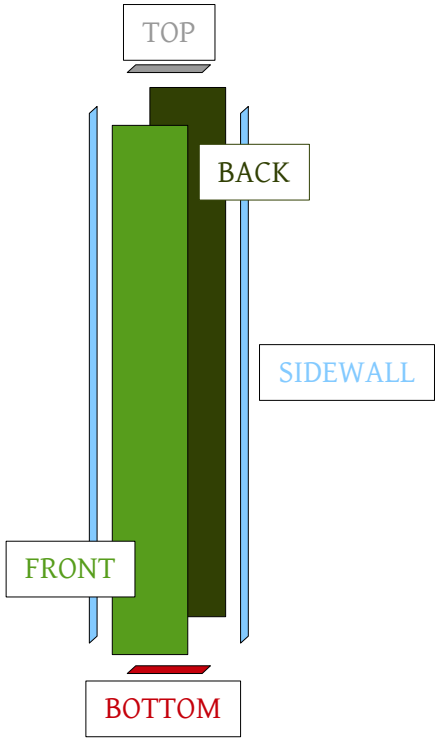

Fig. 4.2: Illustration of the regions in the simulation

4.2 Underlying Differential Equations

The problem to be simulated consists of a continuous liquid phase and a dispersed gaseous phase with a flow regime that corresponds to dilute bubbly flow. As both phases consist of the same component, the process involves mass transfer between the phases. The mass transfer is

driven by sub-cooling and super-heating, therefore by locally different temperatures. This is why the energy equation is a necessity. As strong buoyancy causes slip velocities between the phases the 2-phase formulation has to be heterogeneous. The homogeneous formulation would neglect slip velocities between the phases and that facilitates solving as only one set of momentum equations is solved. Among these there are various mathematical formulations available that are suited to solve the problem.

The mathematical description of the flow is based on the Two-Fluid equations. Two phases are simulated sharing the same volume. By modelling of the interactions between these phases a two-phase simulation is realised. The derivation of the Navier-Stokes equations can be found in the literature [103], but the two-phase formulation, originally derived by Drew [51], shall be shown here. Afterwards the relevant formulation of the models necessary for the phase change are discussed.

The averaging is done using the phase fraction. The letter k is used to denote the phase considered, i.e. l denotes the liquid phase and g the gas phase. The phase indicator function ε_k is phase averaged over the time interval Δt

$$\bar{\epsilon}_k = \frac{1}{\Delta t} \int_t^{t+\Delta t} \epsilon_k(x, y, z, \Theta)\, d\Theta; k = l, g \quad , \tag{4.1}$$

and accordingly the phase velocities are averaged

$$\bar{\vec{u}}^k = \frac{1}{\bar{\epsilon}_k \cdot \Delta t} \int_t^{t+\Delta t} \epsilon_k(\Theta) \cdot \vec{u}(\theta)\, d\Theta; k = l, g \quad , \tag{4.2}$$

as well as the temperatures

$$\bar{T}^k = \frac{1}{\bar{\epsilon}_k \cdot \Delta t} \int_t^{t+\Delta t} \epsilon_k(\Theta) \cdot T(\Theta)\, d\Theta; k = l, g \quad . \tag{4.3}$$

The fraction of each phase resolve to

$$\alpha_l = 1 - \alpha_g \quad . \tag{4.4}$$

Using these phase averages the two-phase formulation can be derived from the original Navier-Stokes equations. The set of equations resolves to the continuity equation

$$\rho_k \left\{ \frac{\partial \alpha_k}{\partial t} + \nabla (\alpha_k \vec{\bar{u}}^k) \right\} = \Gamma_k ; k = l, g \quad , \tag{4.5}$$

With the time *t*, the density ρ , the phase fraction α , the velocity $\vec{u}$ and the mass source/sink quantity *Γ.* In the following momentum equation the index m denotes the three spatial directions. The momentum equation is

$$\rho_k \left\{ \frac{\partial (\alpha_k \bar{u}_m^k)}{\partial t} + \nabla (\alpha_k \vec{\bar{u}}^k \bar{u}_m^k) \right\} = -\alpha_k \frac{\partial p}{\partial x_m} + \nabla \left[\alpha_k \left(\underline{\underline{\bar{\tau}}}^k + \underline{\underline{\tau}}^{Re,k} \right) \right]_m + \bar{u}_m^k \Gamma_k + f_{(k,m)} + M_{(k,m)} ; \quad m = 1,2,3 ; k = l, g \tag{4.6}$$

and with the densities δ_k, the phase fraction α_k , velocity u_m, the pressure *p*, the direction x_m, the Reynolds stresses $\underline{\underline{\tau}}$, the term $\bar{u}_m^k \Gamma_k$, which is an momentum exchange by inter-phase mass transfer, the buoyancy term $f_{(k,m)}$ and the momentum exchange vector $M_{(k,m)}$. It is worthy to mention that there is only a single pressure existent. Therefore, the bubbles do not have an increased pressure caused by surface tension. The full buoyancy model depending on the density is used. The equation for the buoyancy force is

$$f_{(k,3)} = \frac{\pi}{6} d_b^3 (\rho_{ref} - \rho_g) g ; f_{(k,1)} = f_{(k,2)} = 0 \quad , \tag{4.7}$$

with the bubble diameter d_b, a reference density ρ_{ref}, the gas density ρ_g and the gravitation *g*. The energy equation is given by the following equation (4.8).

$$\rho_k c_{vk} \left\{ \frac{\partial (\alpha_k \bar{T}^k)}{\partial t} + \nabla (\alpha_k \vec{\bar{u}}^k \bar{T}^k) \right\} = \nabla \left[\alpha_k (\bar{q}^k + \bar{q}^{Re,k}) \right] + \bar{e}_{tot}^k \Gamma_k + E_k \tag{4.8}$$

with the term $\bar{e}_{tot}^k \Gamma_k$ that resolves to

$$\bar{e}_{tot}^k = c_{vk} \bar{T}_k + \frac{1}{2} (\vec{\bar{u}}^k)^2 \quad . \tag{4.9}$$

The other quantities are the density ρ, the heat capacity with constant volume c_v, the fraction α_k, the temperature *T*, the time *t*, the velocity u_m, the heat flux q_m and the phase energy exchange term *E*.

The following equation shows, how the vapour fraction α_g, the bubble diameter d_b and the bubble number density n (i.e. per volume) are related. The vapour fraction α_g is a calculation result and cannot be pre-described. Therefore either the bubble diameter or the bubble number density has to be modelled.

$$\alpha_g = \frac{\pi n}{6} d_b^3 \Leftrightarrow n = \frac{6\alpha_g}{\pi d_b^3} \Leftrightarrow d_b = \sqrt[3]{\frac{6\alpha_g}{\pi n}} \tag{4.10}$$

The heat and mass transfer in the so-called particle model considers bubbles to be rigid spheres. These bubbles are at saturation temperature as there is strong mixing inside a moving bubble. Therefore the bubbles temperature in a first approach depends on pressure only. The liquid surrounding the bubble transfers heat if the temperature differs from that of the bubble. The problem is then basically a heat transfer problem. An illustration is shown in Fig. 4.3. The relative velocity of the liquid is $\Delta\vec{\bar{u}}$, which depends on the forces acting on the bubble. The liquid temperature $\bar{T}^l$ depends on the solution of the energy equation. The interface being at saturation temperature T_{sat} is assumed and depends on the pressure. Usually, the corresponding pressure is the liquid pressure and not the bubbles internal pressure. The thickness of the interfacial boundary s is considered to be infinitesimally small.

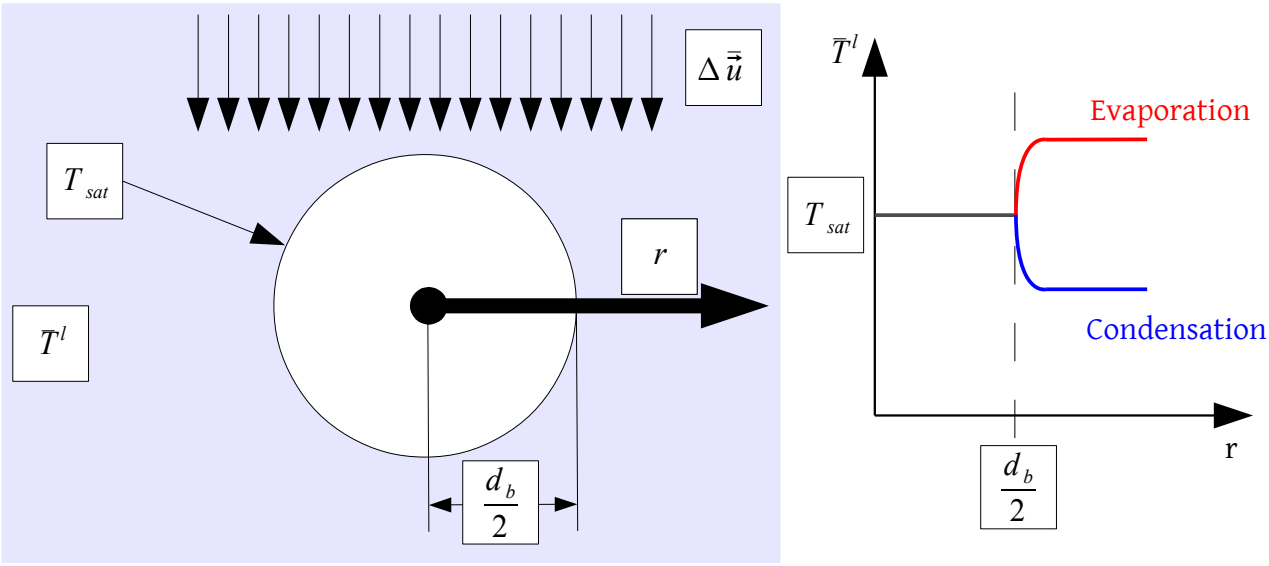

Fig. 4.3: Illustration of the particle model used for modelling the heat transfer between the phases

For the heat transfer coefficient that determines the heat flux, e.g. the Ranz-Marshall model[70] can be used. The Reynolds number is necessary for the heat transfer correlation. The heat

transfer coefficient is calculated from the relative velocity of the bubble. Depending on the prescribed bubble diameter and the local vapour fraction the bubble number is determined. That way the inter-facial area for heat transfer is determined, too. Hence, by changing the diameter the heat transfer inter-facial area is changed. The bubble slip velocity, again, depends on the bubble diameter, because it changes the buoyancy and an increased velocity causes higher heat transfer coefficients. All heat transfer directly causes mass transfer with the amount being determined by the transferred energy and the evaporation enthalpy. Thereby the vapour fraction is increased. The mathematical description is shown in the following equations. First, the Reynolds number is calculated using the slip velocity of the bubble.

$$Re = \frac{d_b \Delta \vec{\bar{u}}}{\nu_l} \tag{4.11}$$

The variables are the bubble diameter d_b, the slip velocity $\Delta \vec{\bar{u}}$ and the liquid viscosity ν_l. With the Reynolds Number known, the Ranz-Marshall correlation can be used to calculate the heat transfer coefficient h_{RM}.

$$h_{RM} = \frac{\lambda_l}{d_b} \cdot (2 + Re^{0.5} \cdot Pr_l^{0.33}); \; with \; Pr_l = \frac{\eta_l c_p}{\lambda_l} \tag{4.12}$$

Besides the Reynolds number Re, the Prandtl number Pr_l, which only depends on the liquid properties, is necessary. The Prandtl number depends on the liquids dynamic viscosity η_l, the heat capacity with constant pressure c_p and the heat conductivity λ_l. Now, the heat transfer model, as well as the inter-facial area ($n \cdot \pi \cdot d_b^2$) is defined. The energy transfer E_l is driven by the difference between the liquid temperature $\bar{T}_l$ and the saturation temperature T_{sat}.

$$E_l = h_{RM} \cdot n \cdot \pi \cdot d_b^2 (\bar{T}_l - T_{sat}), \; E_g = 0 \tag{4.13}$$

Using the evaporation enthalpy of liquid water the transferred energy directly causes mass transfer between the phases. Hence, the source-/sink term resolves to

$$\Gamma_l = \frac{E_l}{\rho_l \cdot \Delta H_{evap}} = -\Gamma_g \quad . \tag{4.14}$$

This is calculated according to the evaporation enthalpy ΔH_{evap}. The momentum modelling can be formulated by equating the forces acting on the bubble.

$$\vec{M}_g = \vec{M}_l = n \cdot \sum \vec{f}_i \tag{4.15}$$

The drag force that is acting on the bubble is

$$\vec{f}_D = c_D \frac{\rho_g}{2} \Delta \bar{\vec{u}}^2 \frac{\pi}{4} d_b^2 \cdot \; with \; \Delta \bar{\vec{u}}^2 = \left| \bar{\vec{u}}_g - \bar{\vec{u}}_l \right| (\bar{\vec{u}}_g - \bar{\vec{u}}_l) \quad . \tag{4.16}$$

It depends on the drag coefficient c_D, the vapour density ρ_g, the squared velocity difference $\Delta \bar{\vec{u}}$ and the bubble diameter d_b. By using equation (4.10) the momentum can be calculated by

$$\bar{\vec{M}}_g = c_d \frac{3 \alpha_g \rho_l}{4 d_b} \cdot \Delta \bar{\vec{u}}^2 \tag{4.17}$$

The drag coefficient is modelled using the Schiller-Naumann model, which is

$$c_D = \frac{24}{Re} (1 + 0.15 \cdot Re^{0.687}) ; \; Re = \frac{\Delta \bar{\vec{u}} \cdot d_b}{\nu_l} \quad . \tag{4.18}$$

Throughout the chain of calculation the bubble diameter is used but not modelled. The starting point for modelling is equation (4.6) and (4.10) and it has to be decided first if either the bubble diameter or the bubble number density shall be modelled.

By definition of the bubble number density the bubble diameter is determined from the vapour fraction which is a calculation result. It has been noted that in the current Euler-Euler formulation only one pressure exists. The pressure inside of bubbles however is increased by surface tension forces. Especially with smaller bubbles the curved surface increases the bubbles' internal pressure. In consequence the saturation temperature of the bubble increases. Using the Young-Laplace equation [104] the pressure increase can be described for spherical bubbles. The surface tension σ is constant, but the exerted forces depend on the surfaces' curvature.

$$p_{YL} = \frac{2 \sigma}{r_b} = \frac{4 \sigma}{d_b} \tag{4.19}$$

When this equation is considered an increase in the internal bubble pressure is beginning to show in the sub-millimetre range. This is why a stable bubble becomes very small for high super-saturations and has an infinite diameter for saturation. Below 0.1 mm bubble diameter the equilibrium temperature inside the bubble increases strongly (see Tab. 4.4). As in the measurements only small super-saturations were found, it is unreasonable to use very small

bubble diameters, as these bubbles are non-viable unless higher super-saturations are achieved.

Tab. 4.4: Increasing internal pressure with decreasing bubble diameter

d_b	[mm]	1	0,1	0,01	0,001
p	[Pa]	p_{amb}+240	p_{amb}+2400	p_{amb}+24000	p_{amb}+240000

4.3 Model Mechanism and Bulk Boiling Model

The model to be proposed extends the general concept of a constant bubble number density. As previously shown in the experimental investigation some main effects are important. Firstly, to create homogeneous nuclei inside a volume, large super-heating is necessary. This has been shown by many authors [40]-[46] that investigated nucleation physics. The physical case of heterogeneous nucleation is not sufficiently understood to be exploited for practical application, although the necessary super-heating is lower. Secondly, upon pre-existence of micro-bubbles super-heating is suppressed by evaporation into the very same existing micro-bubbles.

The physical term “nucleus” is defined for a canonical system, therefore the term micro-bubble will be used for very small bubbles (< 0.1 mm) that interact with the surrounding liquid temperature. An important characteristic of the micro-bubbles is the increased saturation temperature. If there is an existing number of micro-bubbles inside a volume it is important to relate how many actually activate to grown bubbles. The change in saturation temperature caused by bubble growth and the decreasing hydrostatic pressure may exceed the capabilities of the modelled heat transfer from liquid to vapour and therefore, if the heat/mass transfer is insufficient, the liquid super-heating will increase. Upon encountering this situation formerly inactive micro-bubbles are activated. Therefore the number density is increased exponentially because of the exponential bubble size distribution (see Fig. 4.4). The assumption of the exponential increase is based on the observed bubble size distribution in the experiment. Third, the growth-/shrink-effect creating upward convection by drag from bubbles. This effect is a result of the previously mentioned bubbles behaviour combined with the local temperature distribution. The bubbles emerging in a superheated area need to exist long enough to drag the water sufficiently. If the upward convection is too slow, the bubbles will collapse to micro-bubble size again. This effect avoids super-heating as the water is heated but no sufficient drag is created to keep the evaporation going.

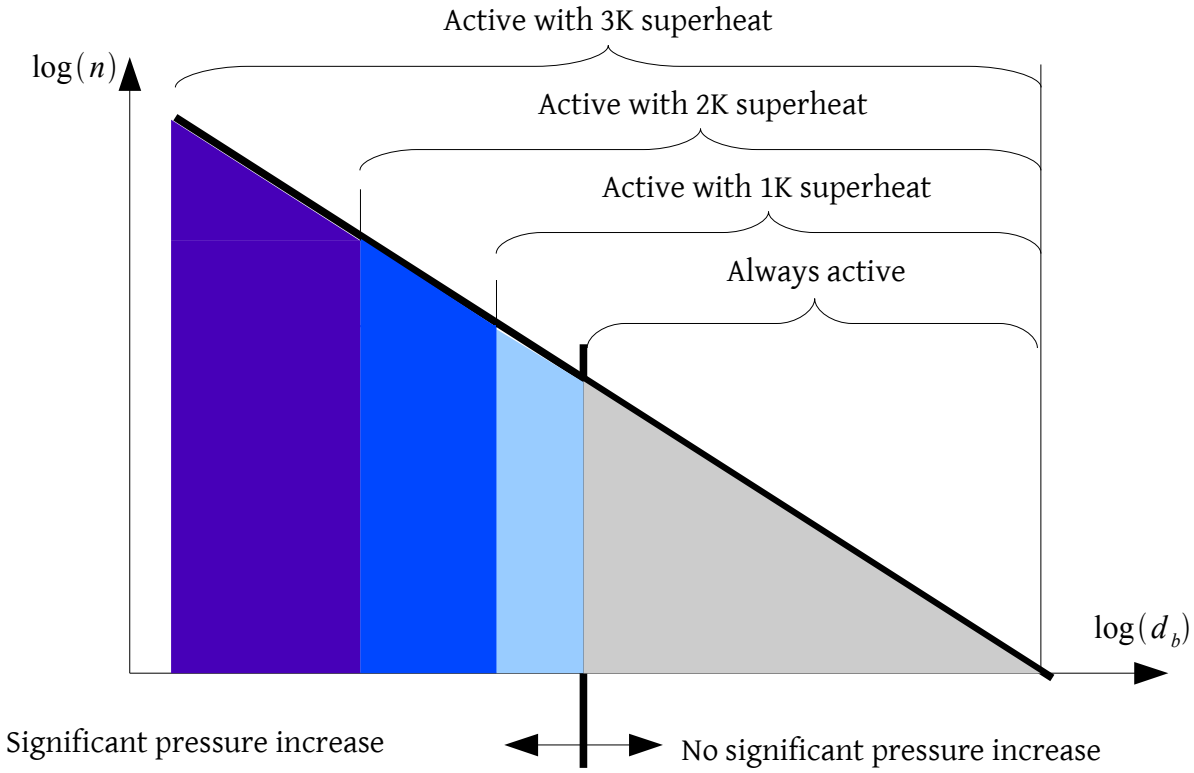

Fig. 4.4: Illustration of the increase in the bubble number density by super-heating

To illustrate this further a gedankenexperiment shall be done. Consider a micro-bubble along a streamline rising inside a liquid column. Inside the container the liquid temperature varies and the heat source is on the bottom. Therefore the unstable situation of hot liquid on the bottom and cooler liquid at the top establishes. The bubble will encounter various local temperatures along its trajectory. At some point the micro-bubble will reach a location along its path where the micro-bubbles' saturation is present. There the micro-bubble will slightly grow. That causes the bubbles' inner pressure to decrease and in consequence the evaporation to continue. The second effect is the acceleration by the increased lift forces. As the bubble has very low inertia the speed-up is nearly instantaneous. So the bubble grows and at the same time accesses latent heat by decreasing its own saturation temperature. The bubbles' quick elevation causes the bubble to outrun its originally surrounding liquid. When the grown bubble then reaches a location along the streamline where the saturation of the grown bubble is present and it shrinks the opposite effect happens. The bubbles saturation temperature increases and the bubble gets decelerated because of the decreased buoyancy of the shrunk bubble. The in-condensible gases remain so that the micro-bubble continues along the streamline. This is graphically illustrated in Fig. 4.5. The red line represents the temperature along the bubble trajectory (blue path). Therefore a hot path

opens after y_1 as there saturation is present and the subsequent evaporation decreases the bubbles' saturation temperature towards the light blue broken line. Therefore the growth continues until the saturation of the grown bubble (light blue dashed line) is below the liquid temperature (red line) past y_2. The bubble shrinking increases the saturation temperature of the bubble towards the dark blue line causing a quick return to the micro-bubble state.

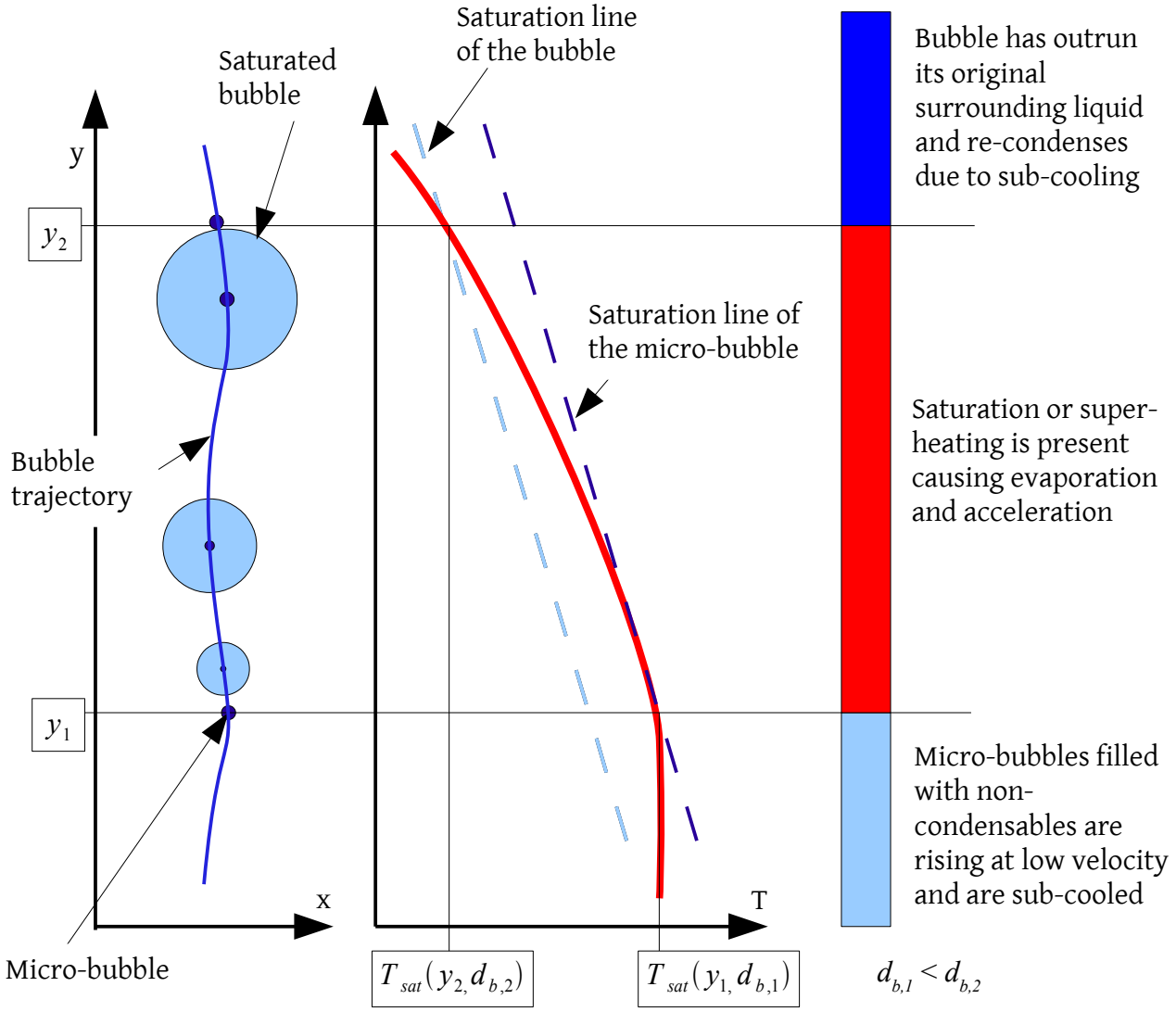

Fig. 4.5: Illustrated growth/shrink mechanism

If the same situation is considered without taking into account that the saturation temperature depends on the bubbles size, the grown bubble would not be able to outrun its original surrounding liquid as it would rapidly re-condense. That is because the bubble growth instantaneously pulls the bubble into sub-cooled liquid and suppresses the observed effect.

The bulk boiling model aims to reproduce the mechanisms that have been observed and discussed in the chapter 3. That includes the possibility of bubble growth/shrinking as well as

increases and decreases in bubble number density. It is dependent on the local super-heating. The super-heating itself depends on local temperatures and pressures. Depending on the local temperatures either a growth/shrink-effect may happen or the upward motion becomes strong enough to cause an evaporation. For obvious reasons the bubble diameter needs to be variable for phase change simulation. Basically this can be achieved by using a constant bubble number density. Hence by increase in vapour fraction the bubble diameter will rise until saturation temperature is established in the surrounding liquid. However the bubble number density is unknown, but the average bubble number density has been measured for the test set-up to be 16680 $1/m^3$. The second effect that cannot be accounted for by using a constant number density is a local sudden increase in bubble number density. Therefore an additional term is incorporated and is depending on the local super-heating. The function increases the bubble number density by an exponential law.

The exponential law is chosen because of the bubble number distribution measured to be of exponential behaviour and therefore, the smaller the size of the bubbles to be activated exponentially more become available. Another aspect is the transient behaviour of the bubble number density that changes very quickly over time in the measurements.

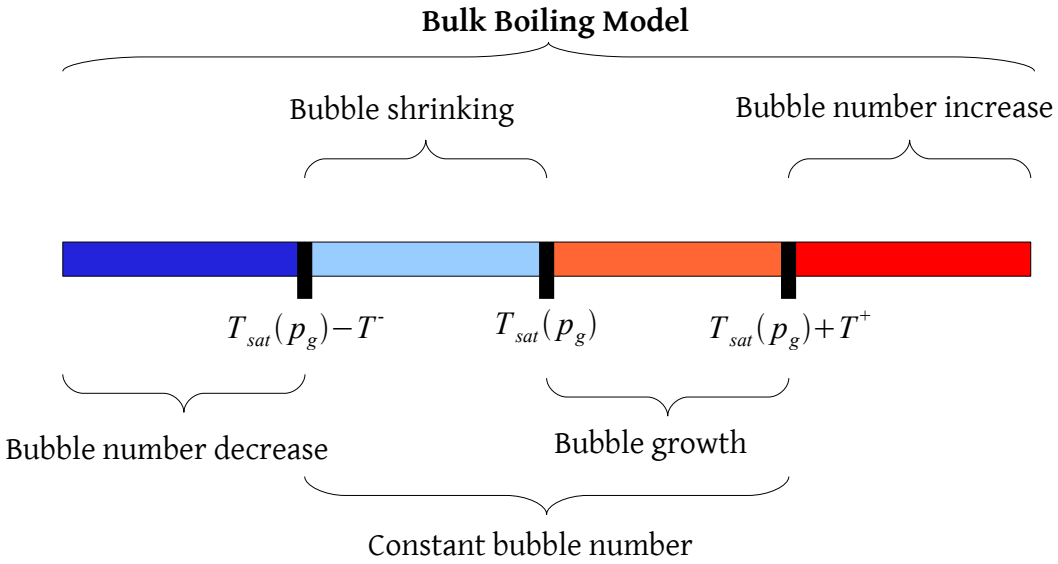

Fig. 4.6: Overview of the boiling model functionality

For comparison the classical nucleation law is based on an exponential law for the nucleation rate. The classical nucleation theory by Becker and Döring, e.g. shown in [12],describes nucleation rate in equation (4.20).

$$J_{BD} = \sqrt{\frac{2\sigma}{\pi m}} \xi \left(\frac{p_v}{kT} \right)^2 \exp\left\{ \frac{-16\pi\xi^2\sigma^3}{3(kT^3)(\ln S)^2} \right\} \tag{4.20}$$

The super-heating $S = p_v / p_e$ is the ratio of the actual and (thermodynamical and chemical) equilibrium vapour pressures, k is the Boltzmann constant, T is the temperature and σ, ξ and m describe the surface tension of the critical cluster, the molecular volume and the mass of the water molecule , respectively.

The model parameters a and b will now be estimated from the experimental data. Thereby the system is determined by prescription of the bubble number density as then the bubble diameter results from the vapour fraction (see 4.6). The model constant a has the meaning of constantly active number of nuclei, hence a repository of active micro-bubbles. As mentioned earlier, in the experimental set-up the average bubble number density has been measured to be $n_0 = 16680\ 1/m^3$.

$$n = a + e^{b(\bar{T}_l - T_{sat})} \tag{4.21}$$

The second model constant b determines how many more bubbles activate upon super-heating according to the local conditions. In the model concept (see Fig. 4.6) this increase is denoted by the T^* value. Direct measurement of the local super-heating though is not possible with the current experimental set-up. The approximation used is the average temperature decrease encountered after geysering events. However b is related to the gradient of bubble number increase and then again that depends on the flow velocity that actually changes the rate of increase in super-heat. Unfortunately the flow velocity was not been measured at all. To increase the active bubble number density to 10^5 the exponent has to be 11.33 which results from the dependency of number increase on super-heating. The value 10^5 is based on the measured range of the bubble number density. Hence b is calculated by division of 11.33 by the expected super-heating. Therefore one arbitrary, yet reasonable, choice is that for a super-heating of 1.6 K, which was estimated before with the temperature drops during geysering events, the bubble number density shall rise to 100000 $1/m^3$ which results in b = 7.08. When the results of the simulation

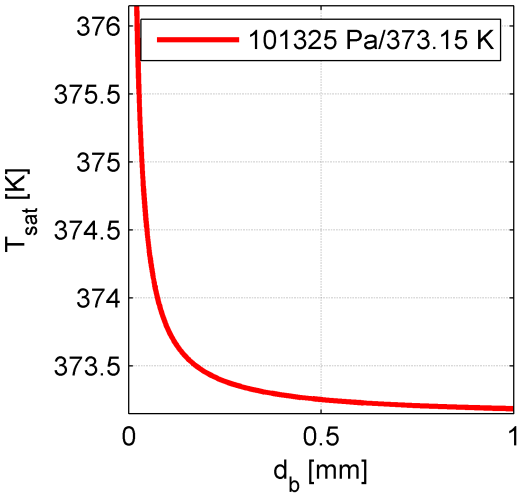

Fig. 4.7: Vapour bubble saturation temperature in dependence on the bubble diameter

reproduce the relevant mechanisms and quantitative value are comparable viable factors have been found. This will be checked later by comparing simulation and measurement data.

To calculate the saturation temperature in °C with the internal bubble pressure p_{YL} and the ambient pressure p_{amb} in Pascal the Antoine equation

$$T_{sat} = \frac{B}{A - \log_{10}((p_{amb} + p_{YL})/100[Pa])} - C \tag{4.22}$$

is used with the constants for water being A = 8.0732991, B = 1656.390 and C = 226.86. This way, the bubbles inter-facial temperature is dependent on the continuous phase's saturation pressure and the bubble diameter. As with low vapour fractions the bubbles are very small the saturation temperature might be too high for evaporation to happen.

This is why the smallest bubble diameter $d_{b,min}$ = 0.1 mm corresponds to a necessary super-heating of 0.6 K (see Fig. 4.7). The value results from the lowest measured bubble sizes. This lower bubbles diameter restriction may as well be considered as a switch from constant bubble diameter to variable number density. So first the bubbles multiply with a constant (and small) bubble diameter and then they start to grow with a constant number density. Afterwards upon sufficient upwards movement the super-heating increases and more micro-bubbles become activated. Therefore below a certain vapour fraction the bubble number density is

$$n = \frac{6 \cdot \alpha_g}{\pi \cdot d_{b,min}} \quad . \tag{4.23}$$

With higher vapour fractions above 10 % there is coalescence and/or break-up (not modelled) that changes the bubble number and therefore the model ceases to be valid as no reduction of the number density in incorporated. However it is thinkable to extend the model capabilities with regard to the local vapour fraction.

4.4 Advection Scheme Blend Study

In Ansys CFX the order of calculation can be varied between first-order and second-order with a so-called blend factor. The blend factor 0 denotes a first-order calculation while the blend factor 1 is a second-order calculation. The other option called high-resolution is a numerical method that iterates the blend factor locally so that the most accurate result with good stability and convergence is achieved. The following study seeks insight into the results dependence on the

order of calculation. Therefore the following calculation set-up is performed with the blend factors 0, 0.25, 0.5, 0.75 and 1. The mesh used is the Stage 1 mesh (Tab. 4.5) consisting of 10000 Elements and with a spacing of 10 mm.

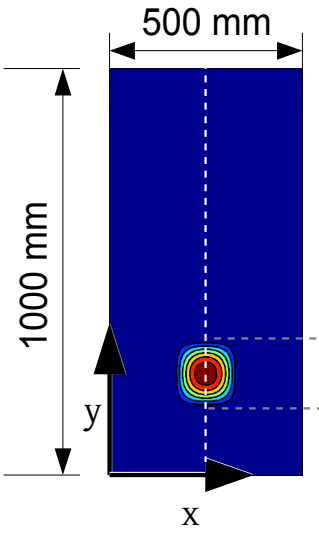

Fig. 4.8: Illustration of the calculation domain

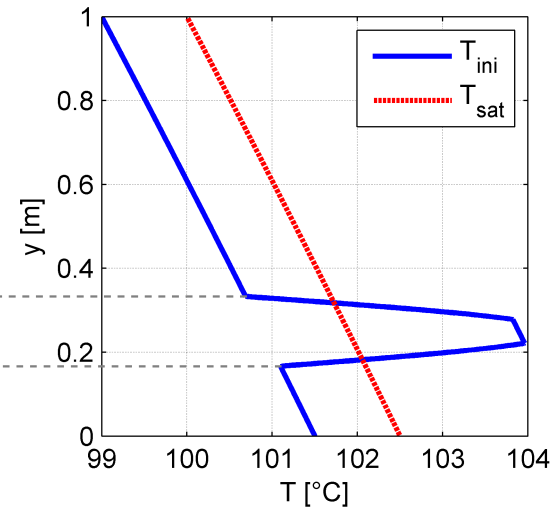

Fig. 4.9: Initialised hotspot used in the blend and grid study

The calculation used for the blend study simulates the evaporation from an initialised hotspot within a water pool. The geometry is a quasi 2D water column with the dimensions 1.0 m x 0.5 m x 0.01 m (see Fig. 4.8). The temperature initialisation generates the necessary thermal pre-conditions for evaporation. A hotspot with 2 K superheat is initialised in the lower part of the volume and the surrounding fluid is sub-cooled by 1 K. The pressure has been initialised using the hydrostatic distribution. The reference pressure at the opening of the system is p_{ref} = 101325 Pa. Hence, the pressure distribution p_{ini} is given by

$$p_{ini}(y) = p_{ref} + \rho \cdot g \cdot (y - y_{WL}) \tag{4.24}$$

with the density δ, the gravitational acceleration g, the ordinate y and the water level y_{WL}.

The initial temperature layering is based on the hydrostatic distribution used in the Antoine-equation.

$$T_{ini} = \frac{B}{A - \log_{10}(p_{ini}/100)} - C \tag{4.25}$$

The hotspot is initialised by the functions given in eq.(4.26) and eq.(4.27). The resulting function given in eq.(4.28) is added to the Antoine-equation given in eq.(4.25)

$$T_{ini,HS}(x)=max\left(\sin\left(\frac{-3\cdot\pi}{x_{width}}\cdot x\right),0\right)\ for\ \ x\in(0,0.5) \tag{4.26}$$

$$T_{ini,HS}(y)=max\left(\sin\left(\frac{-3\cdot\pi}{x_{width}}\cdot y\right),0\right)\ for\ \ y\in(0,0.4) \tag{4.27}$$

$$T_{ini,HS}(x,y)=T_{sat}+min\left(2,3.5\cdot T_{ini,HS}(x)\cdot T_{ini,HS}(y)-1\right) \tag{4.28}$$

The result of this initialisation is shown in Fig. 4.8 and Fig. 4.9.

The plateau is used so that increasing mesh density does not cause changing of the largest local temperatures caused by changing volumetric averaging. Because of the pressure difference from bottom to top the saturation temperature changes, hence, higher super-saturations are achieved.

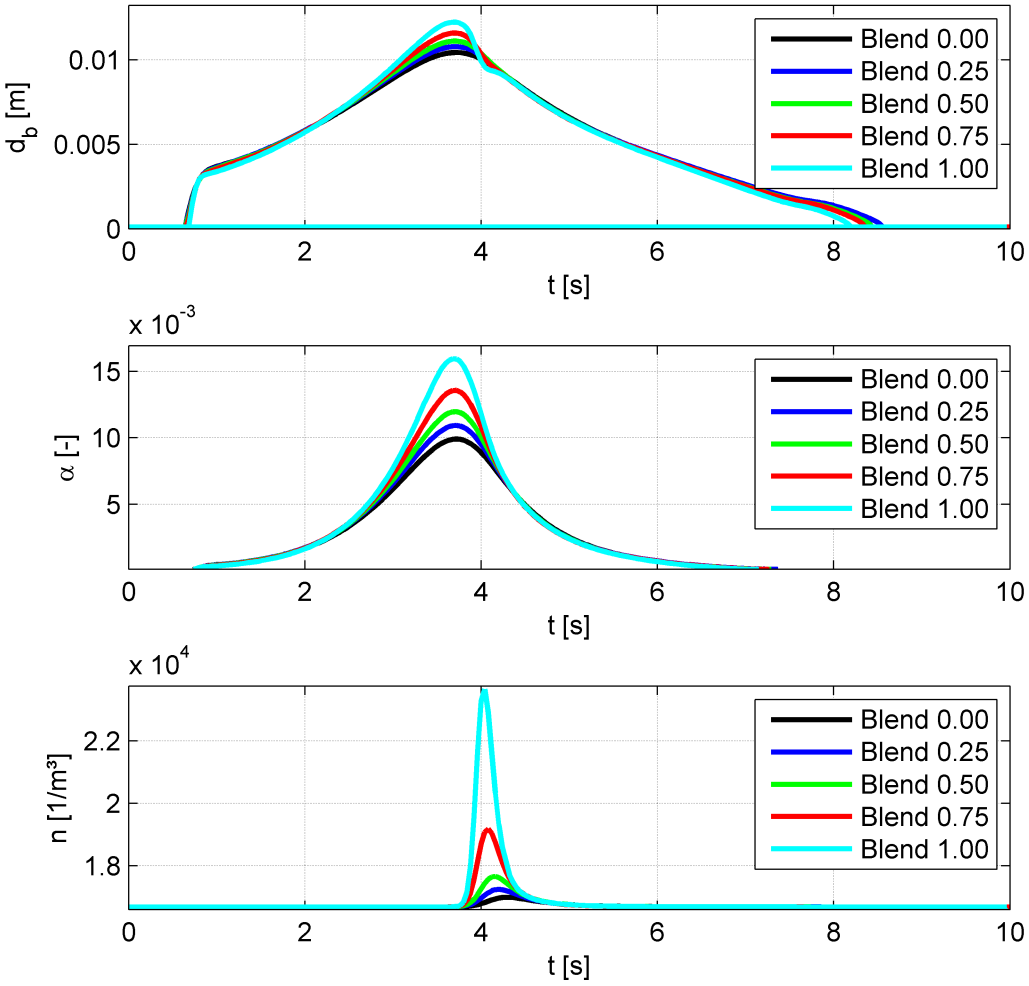

Fig. 4.10: Comparison of the bubble diameter, the vapour fraction and the bubble number density with varying blend factor

The advection scheme or the numerical discretisation of the equations can be done using first or higher order methods. CFX offers first and second order discretisation that can be combined using a blending factor.

It has been stated in the state of the art that a study that compared an Euler-Euler simulation of first and second order with an Euler-Lagrange simulation and concluded that the first order results from the Euler-Euler simulation are not comparable [52]. The comparison is done here using the bubble diameter, the vapour fraction and the bubble number density monitored in a monitor point located above the hotspot (x = 0.25m and y = 0.4m). It can be seen that the blending factor influences the values of the bubble diameter, the vapour fraction and the bubble number density.

The higher the order of the calculation the larger the bubble diameter, the vapour fraction and the increase in bubble number density (see Fig. 4.10). The increased bubble number density with increasing blend factor means that the local super-heating is increased. Therefore the model is sensitive to the advection scheme order. This is because of lower numeric diffusion with increasing scheme order and therefore sharper gradients increasing the local super-heating. In consequence the bubble diameter is decreased at higher super-heatings. The slopes of the changing vapour fraction increase as well which indicates that the heat-/mass transfer is increased with the higher advection scheme order. Therefore the mass transfer to the vapour phase is increased resulting in an ultimately higher vapour fraction and this results in a higher maximal vapour bubble diameter. All simulations had calculation times that are in the same order of magnitudes, as well as similar residuals below 10^{-4} RMS value. Hence, the only sensible choice is to calculate using a second-order scheme by setting the blend factor to 1 as it is able to deliver the necessary gradients that are needed to account for local effects.

4.5 Grid Convergence Study

A grid study is a way to identify, if the result is dependent on the used grid. This could be due to a dependence of the model on the local resolution, which may resolve more effects. The same set-up as in the previous blend study calculations is used. Several calculations with the same initial and boundary conditions with increasing mesh density are performed. The advection scheme blend factor is 1 as it was determined in the previous section.

Tab. 4.5: Mesh refinement steps for the grid convergence study

		Stage 1	Stage 2	Stage 3	Stage 4
Nodes	[-]	15453	60903	94878	241803
Elements	[-]	10000	40000	62500	160000
Spacing	[mm]	10	5	4	2,5
Norm. Spacing	[-]	1	2	2,5	4

Tab. 4.6: Coordinates of the monitored target quantities

		Monitor Point 1	Monitor Point 2	Monitor Point 3
x	[m]	0.25		
y	[m]	0.4	0.6	0.8

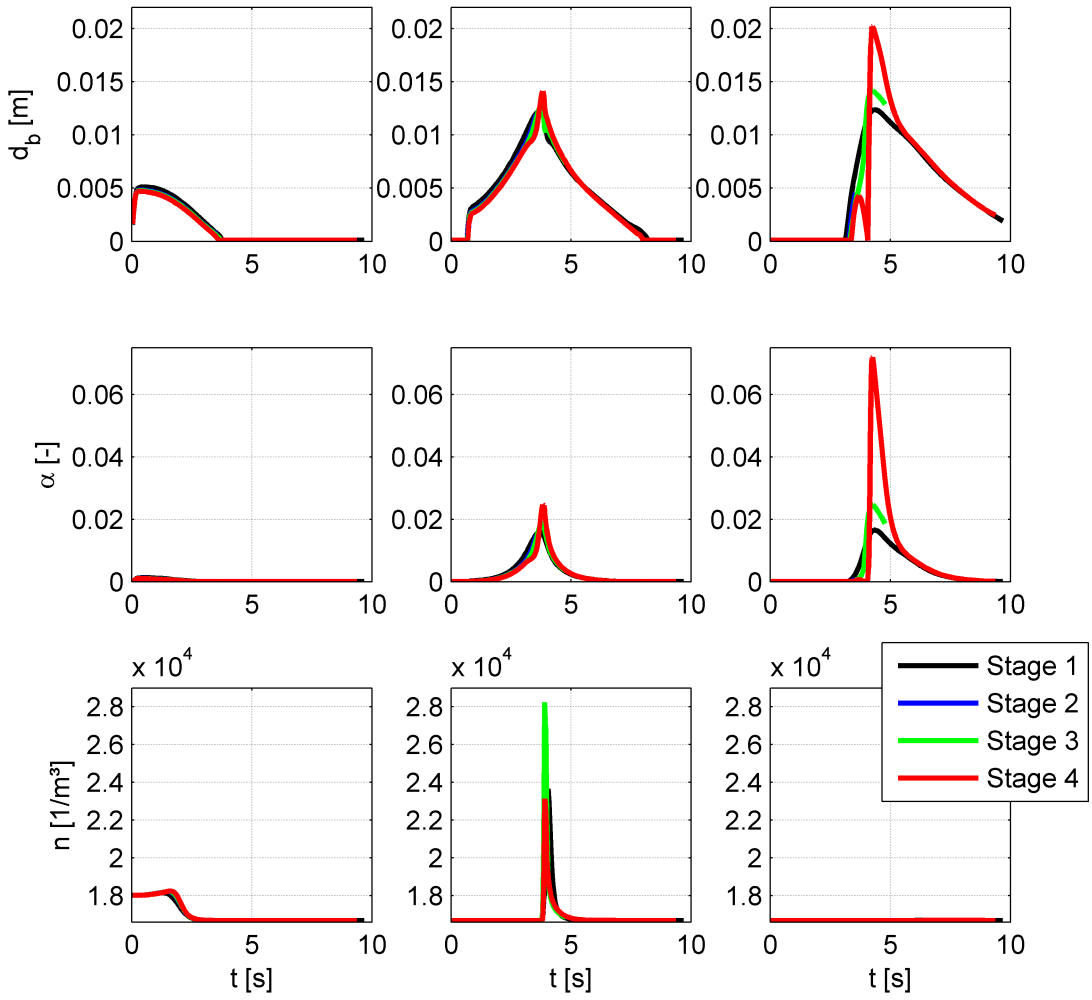

Fig. 4.11: Behaviour of the bubble diameter, vapour fraction and bubble number density depending on the grid size

The theory of numerical methods states that by increasing the mesh density the numerical error decreases [103]. For the case of a mesh with infinite number of nodes the error tends towards zero. That of course is not possible. The grid is refined in two dimensions in three steps, as recommended in [105], resulting in four meshes of increasing density. The grid refinement step 2 and 3 suffered from very long calculation times, whilst the most coarse mesh was the fastest and the most refined grid still had reasonable calculation times. The convergence criteria were met in all calculations, but step 2 and 3 needed many more time steps with minimum time stepping (adaptive) to reach the result.

In Fig. 4.11 nine diagrams are shown. Each column represents a monitored point above the initialised hotspot. The bubble diameter, the vapour fraction and the bubble number density (target quantities) of all four simulations are shown in different colours. The black line represents the coarsest and the red line shows the last refinement step. What can be seen is that in the first monitored point (or first column of diagrams) the grid dependence is negligible. In the second column differences can be noticed. The bubble number density change is increased in the stage 3 calculation but comply in the stage 1 and stage 4 calculation. The other quantities like bubble diameter and vapour fraction are close to identical. In the third monitor point the bubble number density shows no change at all in all stages. It is to be mentioned that this means that the evaporation dominates the upward motion that is relatively slow in all cases. This is why no higher super-heatings are observed and the number density accordingly should not change.

The generated vapour fraction on the other hand is changed. That means that the fine grid causes a higher evaporation rate Γ with the same bubble number density at hand. That indicates that the mass transfer model, which is the previously described single resistance model with the Ranz-Marshall model itself depends on the grid (see Fig. 4.12). Consider the previous gedankenexperiment with the micro-bubble that is moving along a streamline with the growth/shrink mechanism happening. The effect of the evaporation rate was not discussed. If the evaporation/condensation rate is higher the bubble size changes become more extreme. The bubbles grow extremely fast and are pulled upwards fast as they have very low inertia which causes them to run ahead even more in front of the hot portion of liquid. There the bubbles get re-

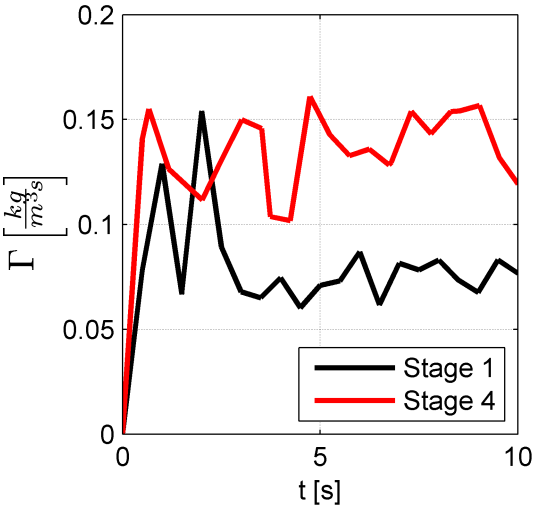

Fig. 4.12: Maximum heat/mass transfer showing the dependency of the modelling on the grid

condensed as quickly and the pulled liquid cannot keep up. The higher bubble diameter depicted in the right column therefore shows two growth/shrink effects instead of one.

Three problems showed clearly in the calculations. Single events of imbalance cannot be avoided and they mostly affect the pressure calculation. To avoid calculation instability the saturation temperature will be defined in the following calculations by the ordinate using the hydrostatic pressure distribution. This way single events of poor quality pressure calculation do not destabilise the calculation. It seems though that improvements are necessary considering the heat transfer modelling and its dependency on the grid. It is indicated that the tendency to produce more vapour with higher grid densities complies with increased vapour generation with smaller bubble diameters. The following calculations are performed using the coarse meshes, as the dependency of the bubble number density is considered sufficiently small. The change in the bubble number density is minor after all. The turbulence numerics are as well calculated in a first order scheme. The turbulence has only minor relevance as the flow velocities are low and the heat transfer mechanism does not depend on it with in this modelling. The 1^{st} order transient scheme is used because the 2^{nd} order scheme failed permanently. The reason cannot be ascertained but it seems that the absolute pressure oscillations are way out of bounds so that the equation of state table is exceeded. Even extraordinary extension of the tables does not solve the problem. The root mean square (RMS) residual target was chosen to be below 10^{-4} and the conservation target demands to be below 1 %. Therefore the grid and solver settings as well as the residual target and conservation target are set as summarised in Tab. 4.7.

It is unfortunate that the heat/mass transfer depends on the grid and the reason is unclear. On the other hand the temperature calculation is less dependant on the grid. That becomes clear because the calculated bubble number density is not affected much. The model for the bubble number density depends on the temperature. So although the vapour fraction may be affected by the problems in the heat/mass transfer model the bubble number density model is valid and has a low dependency on the mesh.

Tab. 4.7: Solver settings determined from grid studies

Mesh width	Advection scheme	Transient scheme	Turbulence numerics	Residual target	Conservation target
[mm]	[Blend Factor]	[-]	[-]	[RMS]	[%]
~ 5	1	1^{st} order	High Res.	$< 10^{-4}$	< 1%

5 Simulation Results

After the general practice for the simulations has been established in the previous section the following chapter will show simulation results comparable to the experimental set-up. The choice of values for the boiling model will be in the range of the experimental findings. That means that the parameter A is tested for the mean bubble number density and for the maximum expectation value of the log-normal distribution. The formerly estimated super-heating (from the temperature decrease) will be the guideline for the parameter B as well as the bubble number density which only shortly exceeded 100000 at all times. Direct comparisons of key values like bubble diameters and bubble number density transient behaviour, as well as vapour fractions are used to fine-tune the final parameters for the boiling model.

5.1 General simulation set-up

The simulation set-up in the following several sections will be identical except for the parameters of the boiling model. If not mentioned the settings shown in the previous chapter are applied. The geometry is now a 2D cut-out of the original experimental set-up and so the dimensions are 2.75 m x 0.39 m x 0.01 m. The meshes cell width is generally close to 5 mm as it was determined and used before and as a result the mesh consists of 44100 nodes or 28618 elements. The calculations were performed on 24 CPUs of the type Intel Xeon @ 2.8 GHz, 8 Mb Cache with a typical calculation time of 2-3 days for a 20 second transient or in other words ~1500 CPU hours. All boundary conditions are set as before (see Tab. 4.1) except the bottom region (BOTTOM) which is now set to constant heat input as the situation is in the experiment and no hot-spot is initialised (see Fig. 5.1 (b)). In the experimental set-up the energy balance cannot be determined, hence it is unclear how much heating energy really is used for evaporation.

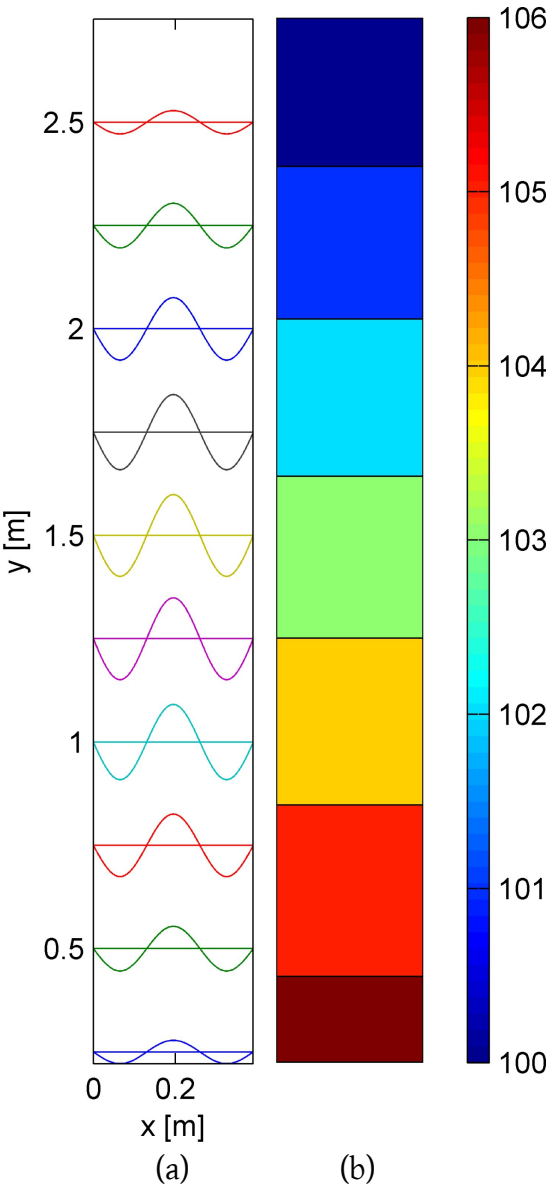

Fig. 5.1: Initialisation of the velocity (a) and the temperature (b) in the simulation set-up

Usually, in the experiment the total heat input power ranges up to 7500 W, but the simulated volume is approximately 1/10 of the volume of the experiment (compare dimensions), therefore a constant heat input of 750 W is imposed. The choice of a constant temperature boundary failed because a calibrated wall boiling model would be a necessity and is not available. Otherwise, without any wall boiling model, the heat input is very low.

The pressure distribution happens to be hydrostatic. The temperature stratification is initialised 1 K below saturation temperature like defined before. As mentioned before, contrary to the previous set-up no hot spot is initialised and, initially, no super-heated hot-spot is present.

$$T_{ini} = T_{sat} - 1 \tag{5.1}$$

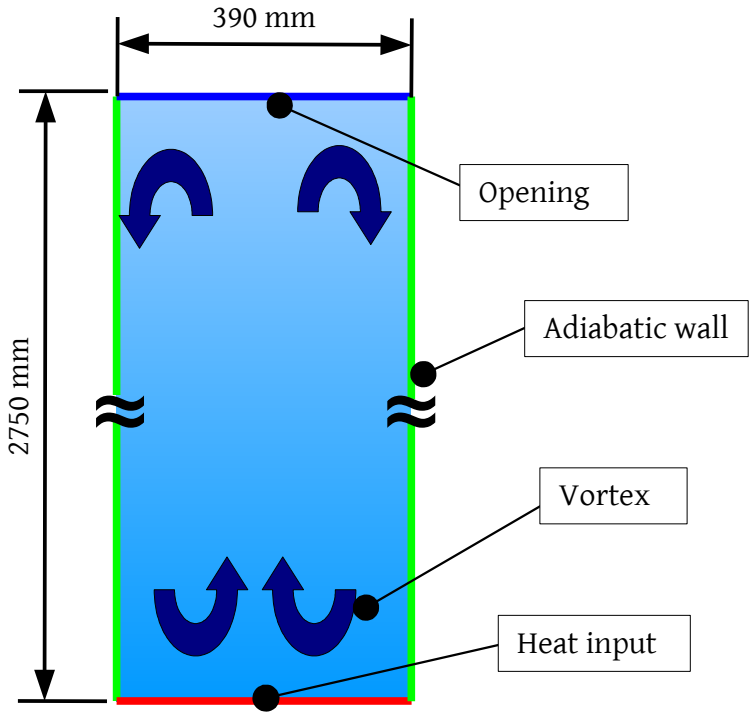

Fig. 5.2: Illustration of the simulation set-up comparable to the experiments

As the calculation times are prolonged unnecessarily by starting from a stagnant condition the initial velocity is prescribed by the equation (5.1).

$$v_{ini}(x, y) = -v_{max} \cdot \sin\left(\frac{3 \cdot \pi}{x_{width}} \cdot x\right) \cdot \sin\left(\frac{\pi}{y_{WL}} \cdot y\right) \tag{5.2}$$

The initial velocity v_{ini} is defined depending on the width in x-direction x_{width} and the water level

y_{WL}. The initialisation corresponds to a counter-rotating double vortex moving the centre of the liquid column upwards whilst the outer parts move downwards (see Fig. 5.1 (a)). The initial maximal velocity of the vortex is v_{max} = 0.1 m/s at half the column height. The calculations are performed for a transient simulation time of 20 s.

5.2 Simulations with varied boiling Parameters

The following sections will vary the parameters of the used boiling model for validation. The first focus of the simulations is to illustrate that the relevant mechanisms observed in the experiments can be reproduced. That means that first a growth/shrink mechanism needs to be observed.

5.2.1 Simulation with low average number density and medium dependency on super-heating

The boiling is used, see eq. (4.21), with the experimentally determined parameters A = 16680 and B = 7.08. The dependency of the bubble number on the super-heating is illustrated in Fig. 5.3. It can easily be seen that the bubble number density does not change significantly below 1 K super-heating.

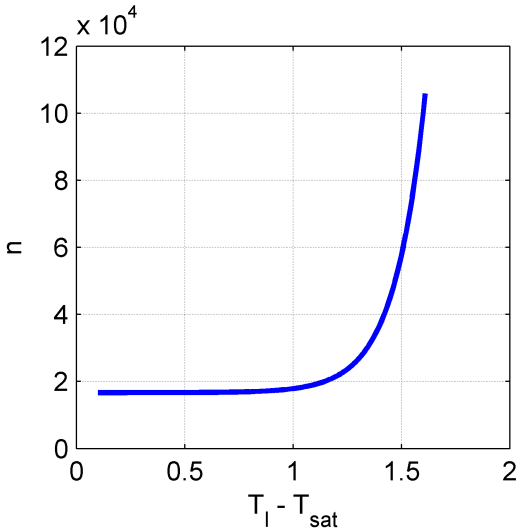

Fig. 5.3: Dependency of the active bubble number density with parameters determined from the experiment

The growth/shrink mechanism is characterised by sudden evaporations and re-condensations that can be seen in fluctuating bubble diameters. The vapour bubbles outpace the saturated or super-heated liquid water. In consequence, the upward motion of the liquid is amplified and the re-condensation of the bubbles heats the water upstream of the vapour fraction to saturation. The general upward motion causes the water above the vapour to become saturated because of the decreasing pressure. Upon encountering that situation an geysering event (geyser) happens as the result of a strong growth/shrink phenomenon and the presence of a hot path. This so-called hot path is a water volume that is at least saturated for bubbles without significant inner pressure (d_b > 0.1 mm) upstream of created vapour. The initial vapour fraction generated by the heat input area encounters three different situations:

- In the centre region there is an upward convection causing the liquid to get closer to

saturation. Therefore after overcoming the sub-cooled region a hot path is available for eventually created vapour. The flow is moving upward and pulls more hot portions of liquid water into lower pressure regions. This is the mechanism that has been described and is needed for a strong growth/shrink mechanism that may cause a geysering instability.

- The second situation encountered is at the wall were the velocity is zero. Close to the wall the water convects downwards with a slow motion.
- The third situation is sub-cooled liquid moving downwards and so the vapour experiences a downward sub-cooled flow. The sub-cooling keeps increasing as the downward convection transports the water into higher pressure regions. Here, no hot path is present and the vapour is likely to escape these regions towards either the centre or wall region. After this energy discharge the system becomes calm for a prolonged time period.

The geysering event is shown in Fig. 5.4 by depicting the vapour fraction using consecutive frames starting from 1.6 s with time steps of 0.2 s. Approximately the first half of the images the bubbles outpace the super-heated liquid which can be seen by higher vapour fraction following lower vapour fractions. Then a hot path opens and the vapour keeps rising with very little re-condensation which is why no smaller leading vapour fractions are present any more.

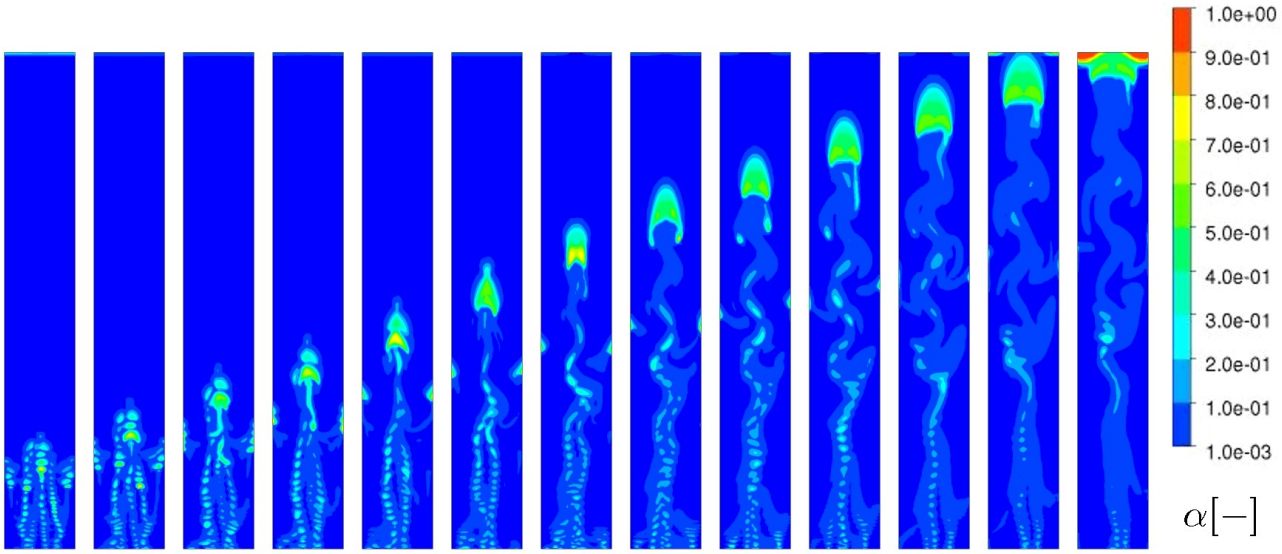

Fig. 5.4: Image series showing the evolution of the vapour fraction

To illustrate the growth/shrink mechanism further, the smaller leading bubbles can be seen in the image series shown in Fig. 5.5. Here a smaller cut-out of the image section is used and the bubble diameter is shown. The biggest bubble diameter is trailing smaller leading bubbles clearly.

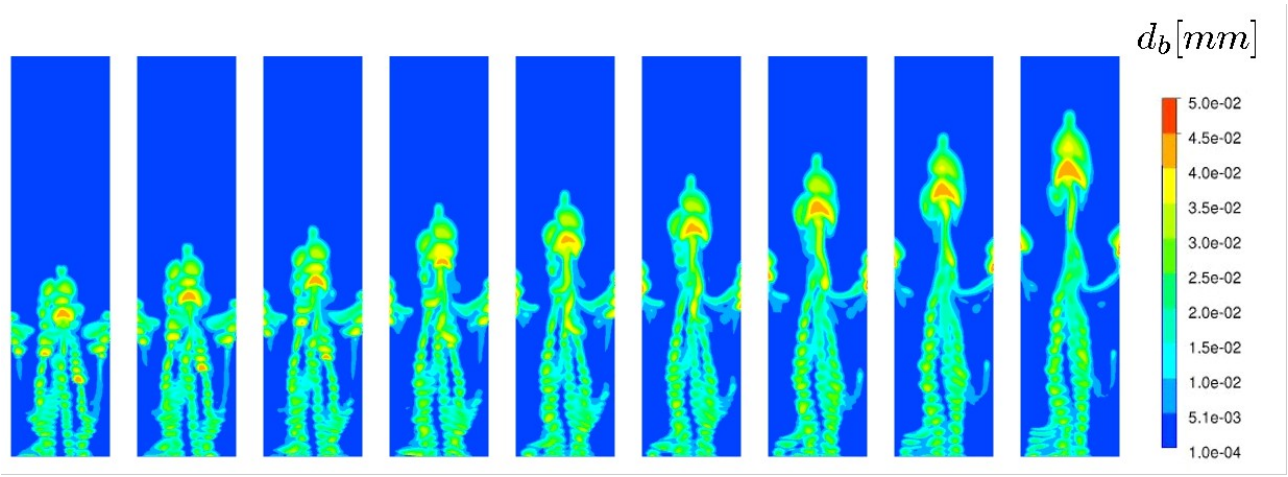

Fig. 5.5: Image series showing the bubble diameter changes

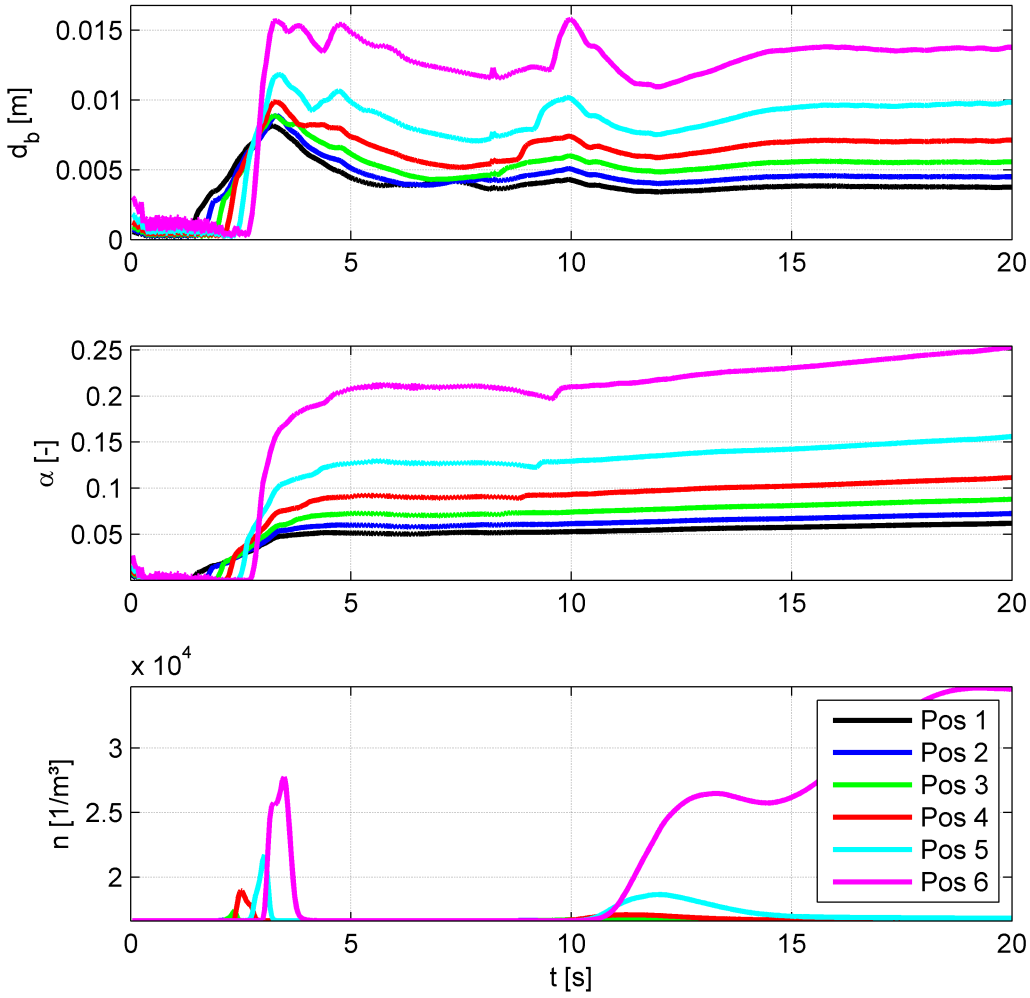

Fig. 5.6: Calculated average bubble diameter, vapour fraction and bubble number density with the boiling values A = 16680 and B = 7.08

The bubble number density was determined in the same way as in the experiment. Comparable volumes were defined and the arithmetic average of the bubble number density in that volume was calculated by the total number of bubbles in relation to the volume. This way the transient bubble diameter, the vapour fraction and the bubble number density is extracted in the different volumes and shown in Fig. 5.6. The quantitative behaviour of the bubble diameter is reasonable.

First, the average bubble diameter is small until super-heating is established. Then quickly the vapour fraction increases and with it the average diameter increases. The bubble number density changes only shortly and does not seem to have a strong impact on the diameter or the vapour fraction. The average bubble number density remains unchanged, as to be expected from the small and short increase in bubble number density.

The diagram in Fig. 5.7 shows the detailed quantitative representation of the growth/shrink mechanism (amplified cut-out of Fig. 5.6) and offers a clear distinction to the geysering as the bubble size fluctuation ceases after some time. The six positions shown correspond to the six measured volumes inside the experimental set-up. In position 1 (black line), which is the lowest considered volume, the bubble diameter fluctuates between 0.1 mm and 0.3 mm. With increasing vapour fraction this range increase up to position 6 (magenta line) where the diameter changes between 0.5 mm and 1.5 mm. At some point in time all the fluctuation stops and the diameter quickly rises continuously. That is when the mentioned hot path opens upstream and the bubbles do not encounter a sub-cooled layer any more. This situation results in a geyser if no sufficient sub-cooled layer appears.

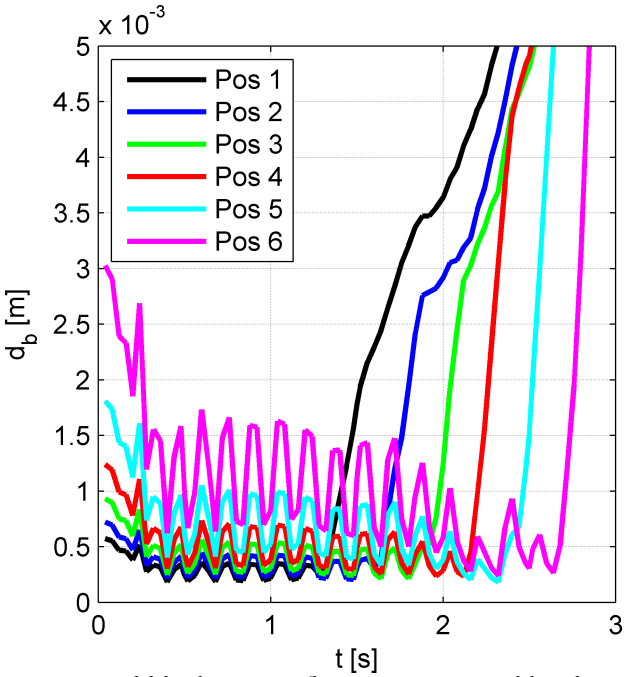

Fig. 5.7: Bubble diameter fluctuation caused by the growth/shrink mechanism

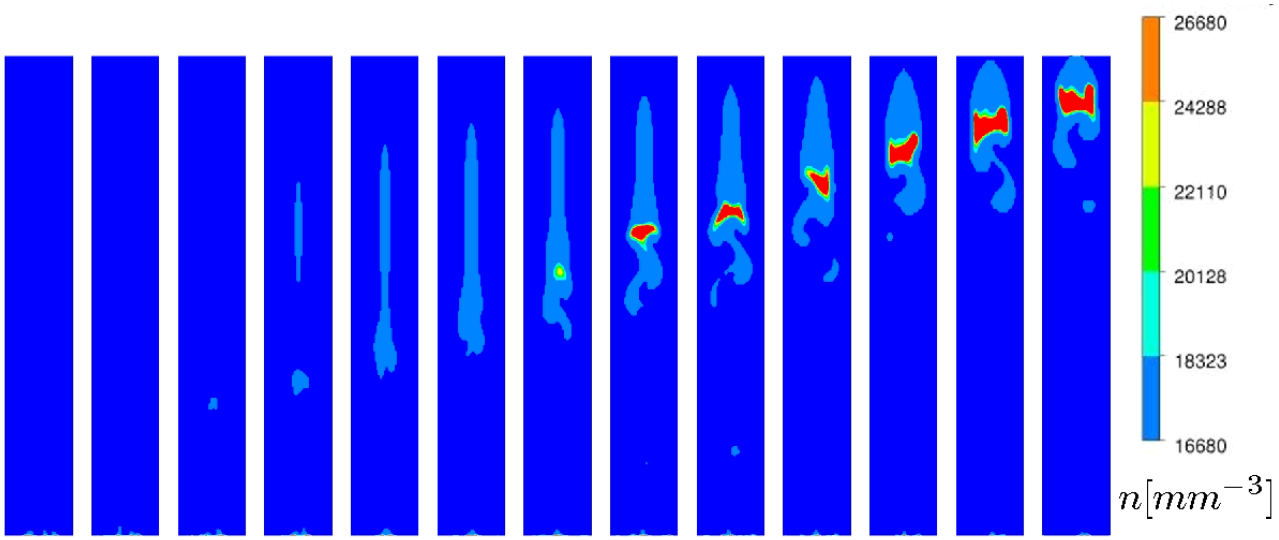

Fig. 5.8: Image series showing the increased bubble number density in the wake region of the rising bubble plume

The geysering instability is instigated by the liquid upward motion that is accelerated by the drag forces exerted by the rising bubbles. It needs to be considered how it is even possible to achieve an increased liquid super-heating. That is only likely if the heat/mass transfer is not sufficiently causing evaporation which would cause a quick return to saturation temperature. This is the case only if the saturation temperature (hence the saturation pressure) decreases more quickly than the evaporation happens. The evaporation rate is limited by the driving heat difference and the heat transfer resistance, as well as the interfacial area. Higher super-heat means that smaller bubbles can become active as they reach saturation. It has been stated earlier that the bubbles internal pressure increases by surface tension forces, which becomes significant for micro-bubbles. According to the experiments statistically the bubble size distribution is exponential and therefore an exponential bubble number increase is happening. Analogously to the previously shown vapour fraction image series, the bubble number density is shown in Fig. 5.8. Here it can be seen, that the quickly rising bubbles cause an increased bubble number density in their wake region. This increase is the activation of the smaller bubbles present. The activation originates from the higher super-heating that is caused by the quick upward motion. The increased bubble number density increases the interfacial area by changing the vapour distribution into more and in average smaller bubbles. These effects were illustrated earlier in Fig. 4.4 and were re-produced now in the simulation as well.

To calculate to the next evaporation event takes too long or is unlikely to happen. A prolonged calculation of 200 s kept getting warmer but was yet to evaporate. Another aspect is, that the vapour generated at the heated surface creates a stable path at the side-walls and the vortex rotational direction flips and becomes stable (see Fig. 5.9 and Fig. 5.10). The corner area where the vertical adiabatic side-wall meets the heated bottom area a constant supply of vapour exists. The vapour created at the bottom area moves mostly along the wall. Therefore, the centre region moves downwards and along the wall a quick upward motion establishes. Such a situation is not encountered in the experiment. This indicates a problem that might be tackled by incorporating a wall lubrication force and turbulent dispersion force, that were not used here. Another possible explanation is that the walls are set to be adiabatic or that the heat input is overestimated. In the experiment there are heat losses at the wall and the near wall cooling might affect the pattern of the natural convection.

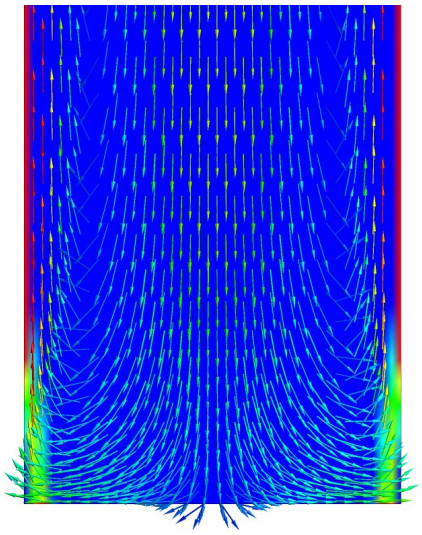

Fig. 5.10: Stable flow situation caused by vapour generation in the corner region

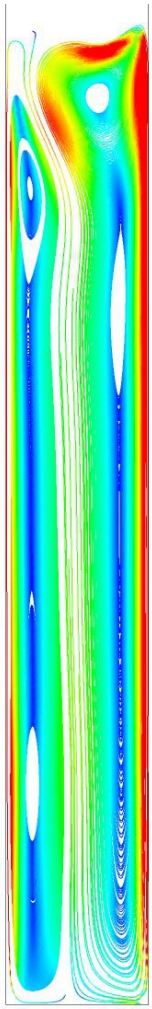

Fig. 5.9: Convection pattern

5.2.2 Comparison of the Water Temperature decrease in the Simulation and the Experiment

During the calculation of the geysering event the water temperature was monitored in several points and the result is plotted in Fig. 5.11 and corresponds to the measurement data shown in Fig. 3.10. Exactly the same behaviour was discussed in the chapter 3.4.2 concerning the experimental measurement. There it was estimated that the local temperature decrease mostly ranges at 1.6 K. The calculation does not offer statistical results but the difference between the maximum and minimum temperature of each monitor point is about 2 K. This would suggest an over-prediction of vapour generation. It can be seen that the behaviour is well represented by an evaporation event that causes an overall temperature decrease and the decrease of the temperatures towards saturation temperature.

The uprising temperatures in the beginning are because of the upward movement in the centre of the column due to the initialised double vortex. Then, especially in the upper parts of the volume, a sharp decrease in temperature is caused by evaporation and the temperature drops to saturation. This is caused by the high super-heating in the upper volume that causes small vapour bubble diameters with higher saturation temperatures. Then strong evaporation quickly cools down the water. After the first geysering event the temperature keeps dropping. Because of the unrealistic steady state that develops over time the temperature keeps dropping and eventually becomes steady. Hence it is not possible to calculate realistic long term transient with re-occurring geysering events. However, this is not necessarily related to the bubble modelling.

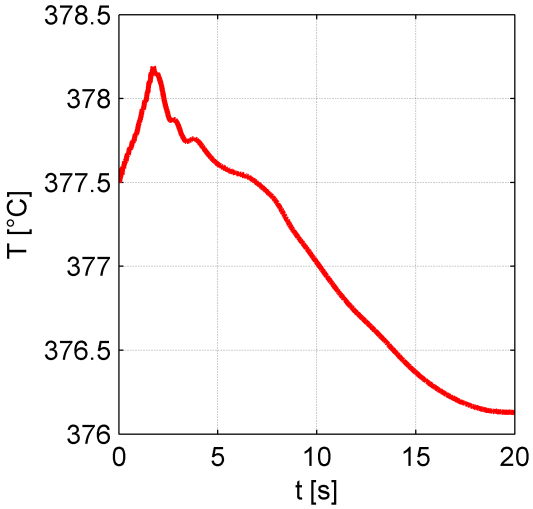

Fig. 5.11: Simulated temperature decrease during geysering event

5.2.3 Simulation with higher dependency on super-heating

In the following sections the parameters of the boiling model are adjusted to consider the model parameters' influence on the results. The simulations are performed analogue to the section before, which is why only a quantitative comparison is shown. The mechanistic behaviour is very similar in all cases and only interesting deviations are mentioned. As the comparison between the simulation and the experiment did only show a relatively low change in bubble number density the Parameter b of the boiling was changed arbitrarily to $b_* = 10.62$, which is 1.5 times higher than $b_{exp} = 7.08$. This changes the model sensitivity of the bubble number density changes to super-heating as the number density now rises to 100000 1/m³ upon 1 K super-heating (see Fig. 5.12).

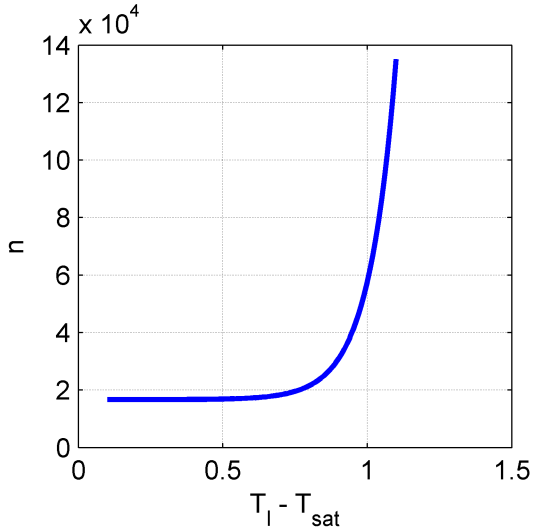

Fig. 5.12: Relation between the bubble number density and the super-heating with increased Parameter b

With lower super-heating the bubble number density increases more, supposedly causing the bubbles sizes in the wake of the leading bubble plume to decrease. That should increase the vapour generation in the wake region during the geysering instability. Like in the previous simulation an image sequence starting from 1.6 s with 0.2 s time stepping between the frames shows the vapour fraction in Fig. 5.14. Apparently in the wake of the bubble plume another bubble plume develops and has bigger bubble diameters again. That would suggest a mechanism similar to the shown growth/shrink mechanism. The effect would additionally amplify the violence of the geysering geysering.

The growth/shrink mechanism is observed as well, which was not self-evident. Upon low super-heating the bubble number density quickly increases, so that the bubble diameter decreases and therefore the bubble growth might be suppressed by the number density increase. In can bee seen that the vapour structures decrease in size. As before the quantities are extracted and shown in Fig. 5.13. Apparently now the increase in bubble number density does exceed the previous

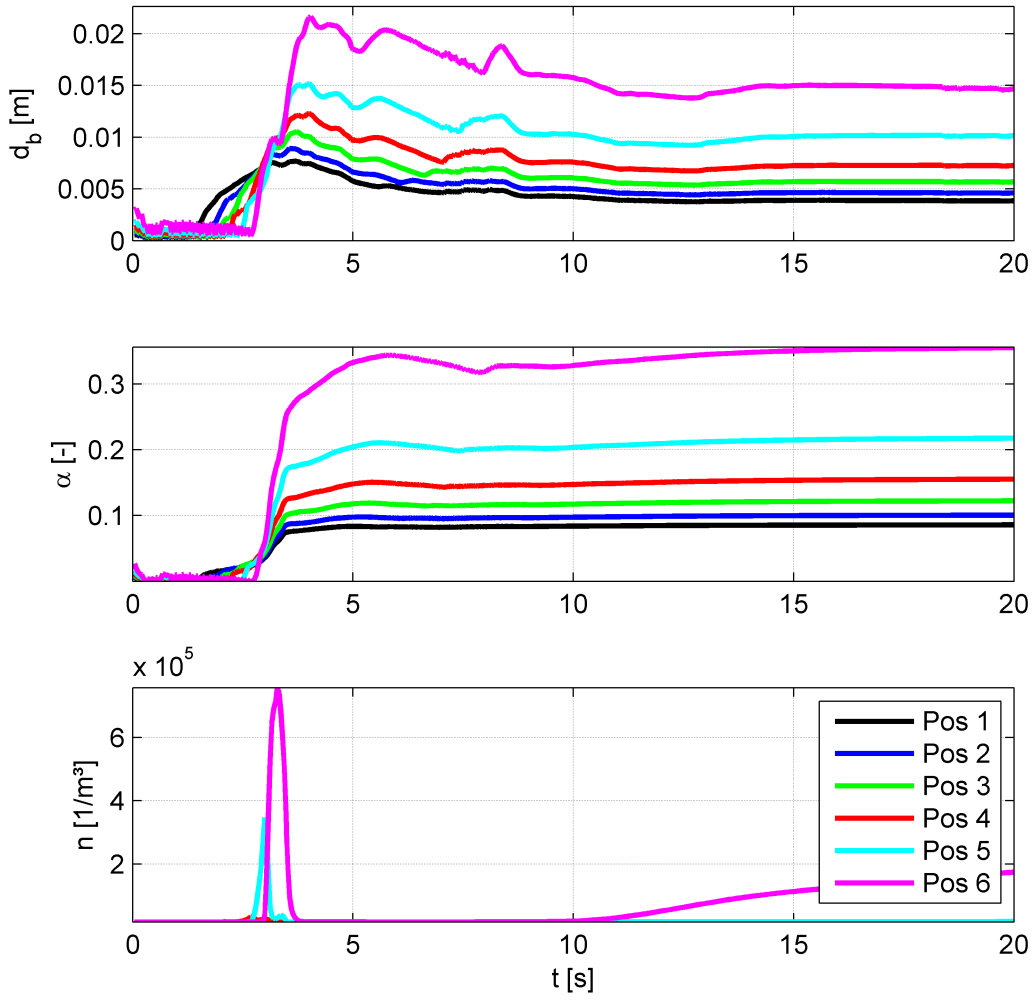

Fig. 5.13: Simulated bubble quantities with high average bubble number and high dependency on super-heating

values. The bubble number density n increases to up to over n = 600000 m^{-3} causing the vapour fraction α to increase very quickly. The average bubble size does not decrease unexpectedly because of the sharp increase in bubble number density, but keeps growing. The increased evaporation compensates for that effect and only shortly keeps the average diameter constant. Therefore the behaviour of the bubble number density is represented better, but the average bubble sizes are higher than expected and a too high vapour fraction is calculated.

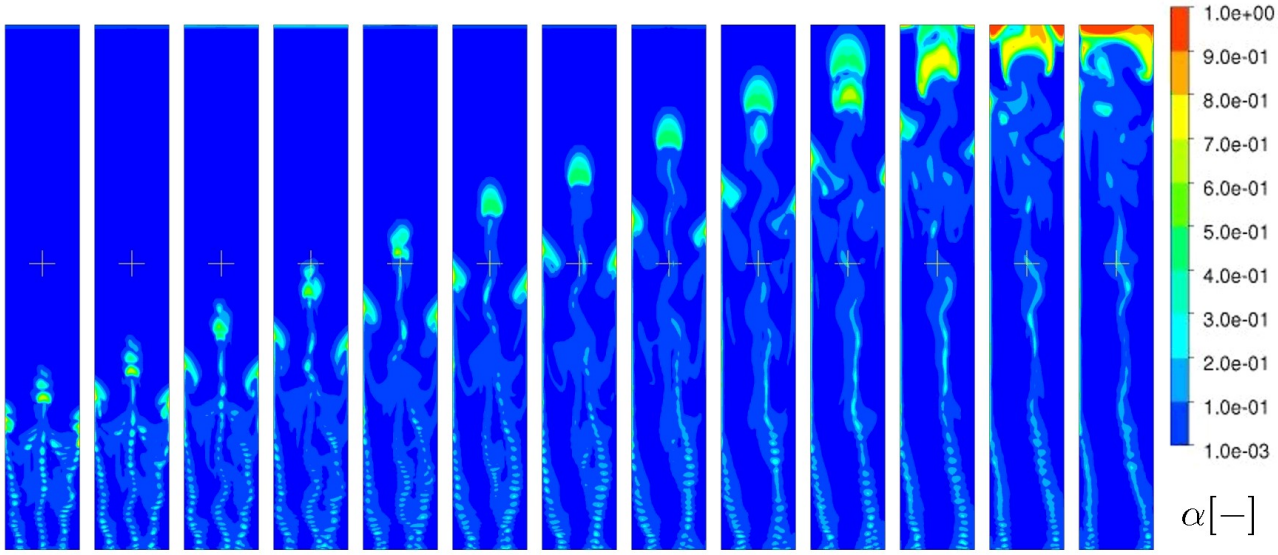

Fig. 5.14: Vapour fraction generation in the wake of the leading vapour bubble plume

It was stated previously that smaller bubble diameters cause more mass transfer and therefore a higher vapour fraction. Considering the average bubble number in the second simulation the average increases to an average of n = 29653 m^{-3} which is still comparable to the experiment. That causes the bubbles to be smaller with the same vapour fraction and this results in an increased vapour generation.

5.2.4 Simulation with lower dependency on super-heating

Although the comparison between the simulation and the experiment did only show a relatively low change in bubble number density the Parameter b of the boiling was changed arbitrarily to $b_{-} = 3.54$, which is half the value of $b_{exp} = 7.08$. Using this parameter reduces the model towards a constant number density situation. Hence it is checked if the increased number density causes the evaporation trailing the leading bubble plume.

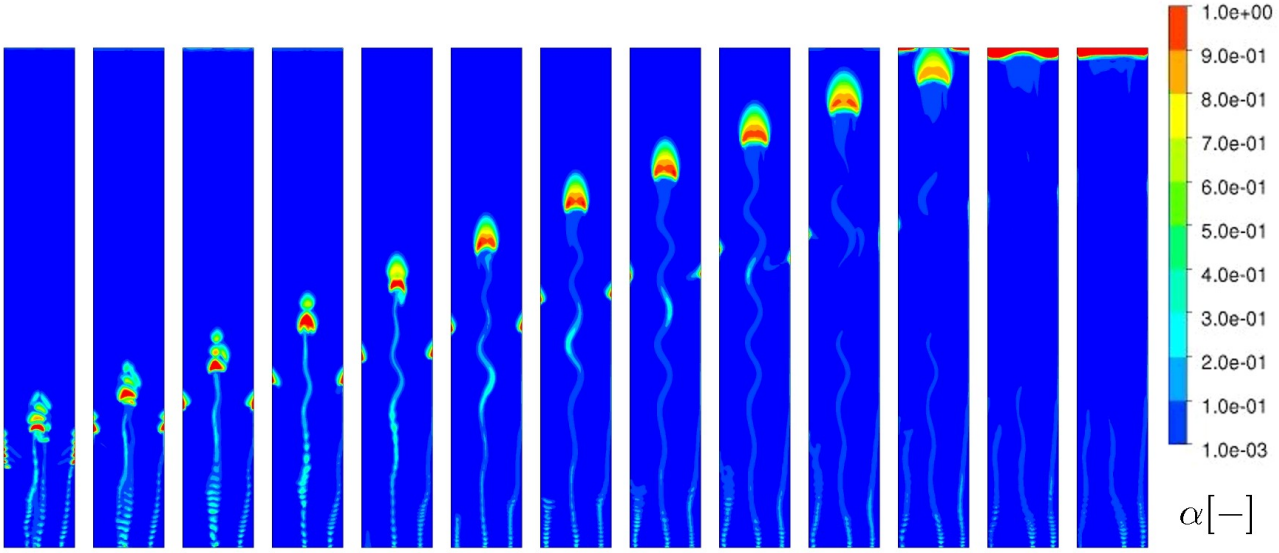

Fig. 5.15: Simulated geysering event with quasi-constant bubble number density

The vapour fraction increases at several locations above the heated surface and the vapour quickly moves upwards. With increasing vapour fraction the average bubble diameter increases as well. In consequence the buoyancy increases as well, which causes higher velocities of the vapour fraction. The volumes of higher vapour fraction unite on their ascend and cause a slight geysering. There is no additional vapour generation in the wake of the leading vapour bubble plume (see Fig. 5.15). The activation of micro-bubbles does not happen and so close to no increase in the bubble number density is present. The growth/shrink mechanism is represented well (see Fig. 5.16).

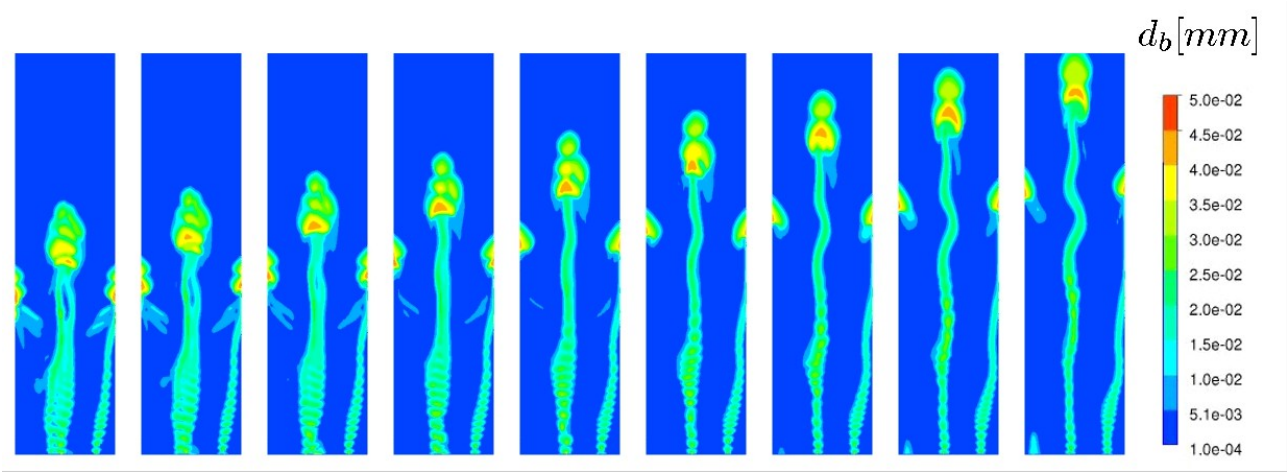

Fig. 5.16: Simulated growth/-shrink effect

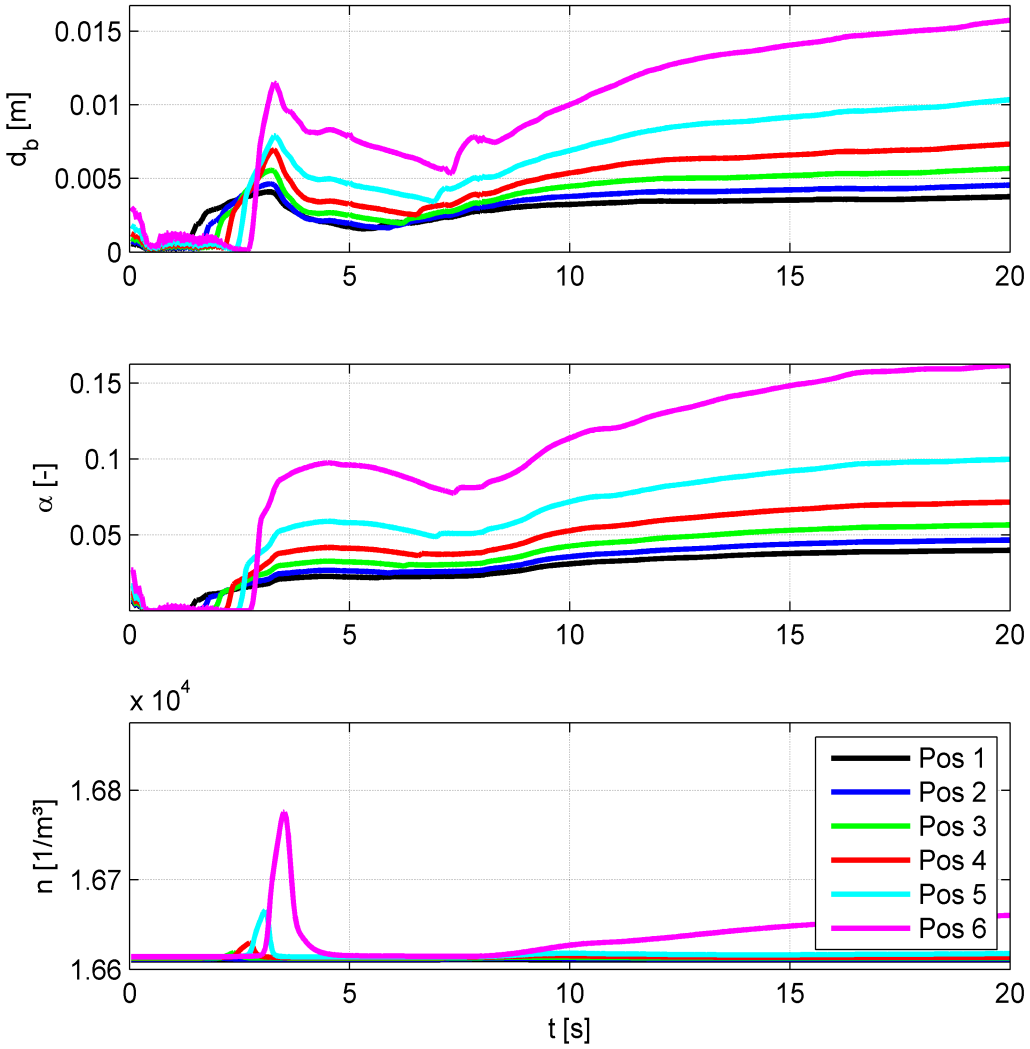

Fig. 5.17: Simulated bubble quantities with low average bubble number density and low dependency on super-heating

The unification of such separate volumes with high vapour fraction has been observed in the experiment as well. When a pair of bubbles rise behind one another in a stagnant pool the trailing bubble moves with higher velocity. Both bubbles in fact do move faster than a single bubble. After the geysering event the system has reached a lower temperature and the generated vapour encounters higher sub-cooling which condenses most vapour. The vapour cannot reach the surface any more. The vapour fraction and bubble diameter estimations show a better agreement than previously but the number representation is worse than before. Therefore in consequence it should be checked if the value for A is too low. As the average bubble number density affects the size of the bubbles, an increase will lower the average diameter. In the experiments data the expectation value for the bubble number density was approximately 75000 at most but till now the arithmetic average of a = 16680 was used.

5.2.5 Comparison with high average bubble number density and medium dependency on the super-heating

Now the highest expectation value for the bubble number density that has been determined from the experiments is used for a = 75000. The parameter for b = 7.08 was shown to be most reasonable in the previous calculations. It is expected to get decreased bubble diameters which were over-predicted previously. At the same time the sudden increases in bubble number density are to be represented.

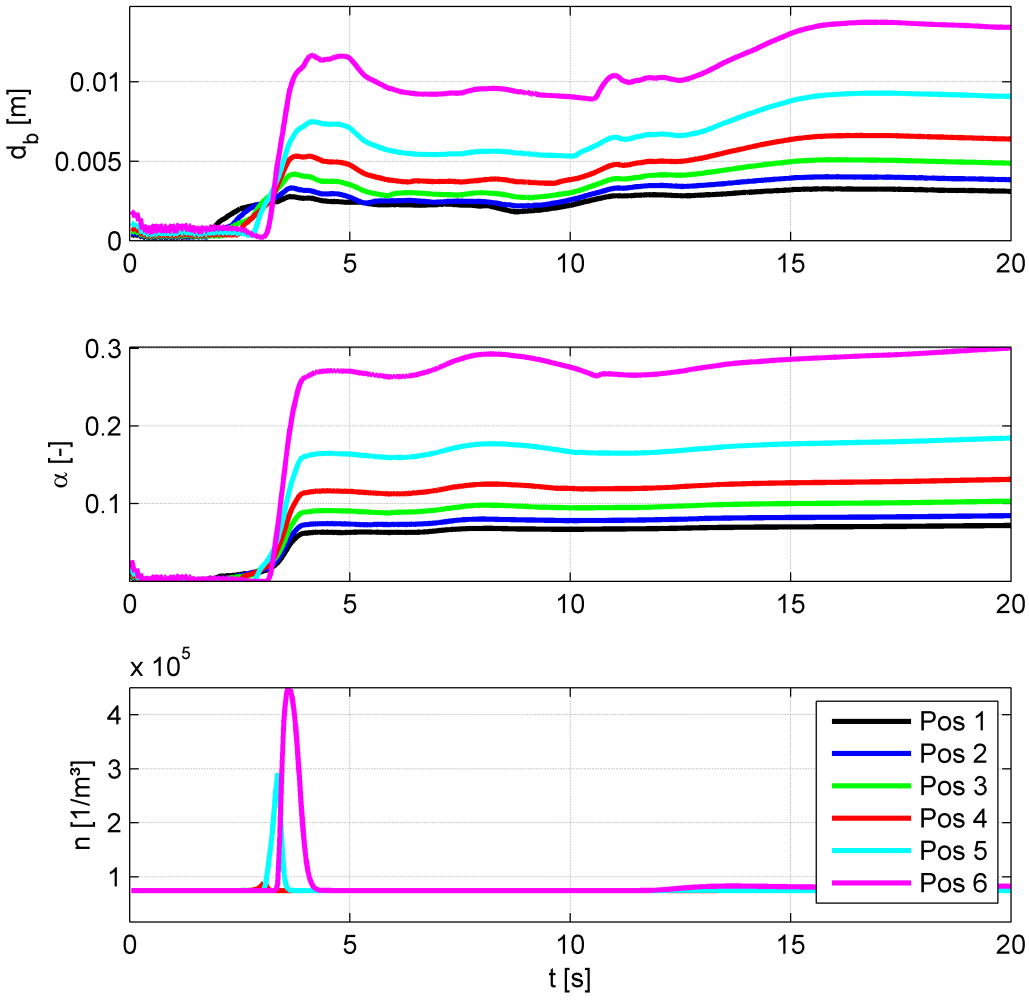

Fig. 5.18: Simulated bubble quantities with high average bubble number and average dependency on super-heating

5.3 Calculation with heat losses along the side-wall

The parameters for the boiling have been ascertained in the previous sections and show good agreement in representing the mechanisms identified in the experiment. The long-term behaviour of the natural convection that develops is unrealistic. Besides the possibility that the bubble forces are not modelled sufficiently there is the possibility that the absent heat loss at the side walls is the cause. Natural convection is very sensitive, so another calculation was performed. The set-up is identical to the previous section, but the side-walls now have a heat transfer coefficient of 10 W/(m² K) with an outside temperature of 20 °C. Hence the outer portions of the liquid column get cooled and a downward convection is expected.

This way the vapour will escape towards the centre of the water column. The stable long term situation observed in the simulations before may change into the unstable situation with several convective vortices in the experimental set-up. The influence on the bubble quantities can be neglected. The values are practically the same as in the previous simulation without heat losses (see Fig. 5.18).

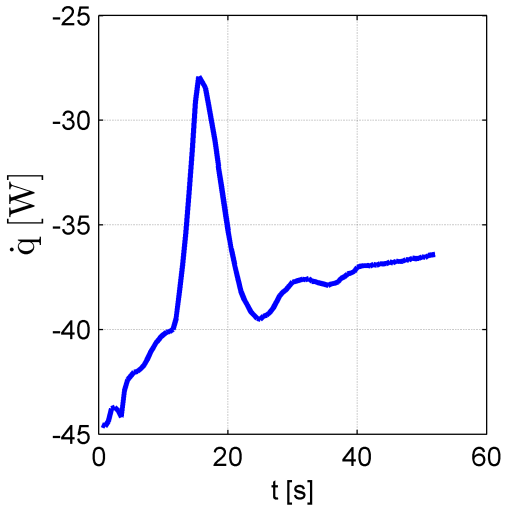

Fig. 5.19: Calculated heat losses at the side-wall in the diabatic simulation

The calculation shows that heat losses along the side-walls do not change the natural convection pattern. It doesn't change the bubble generation whatsoever so it is suspected that the heat losses are too small for any relevant effect. In Fig. 5.19 the heat loss at the side-walls is shown over the simulation time. The values are ranging between -27 W and -45 W and are therefore approximately 20 time lower than the heat input. The water mass that is cooled down at the side-wall region does not cause notable downward movement. Therefore the drag from the rising bubbles suppresses all downward convection and the flow pattern keeps being stable. The vapour generation is simply too strong so that the created vapour is able to rise until it reaches the water surface. Considering the simulation set-up of the heat losses, it does seem that the 2D representation does have the drawback that the heat losses along the walls are not represented well. The experimental set-up certainly has the greatest heat loss at the glass plates and/or at the chimney, where the vapour may re-condense partly and drip back into the water volume. It is well possible that therefore the drag exerted by the bubbles does dominate the single-phase convectional pattern.

5.4 Calculation with lower heat input

The higher vapour fraction may cause the stable flow situation because of the relatively big bubble diameters. The bubbles are lifted quickly and influence the liquid flow more than vice versa. So one more variant considered is the identical set-up as in the previous section but with half the heat input, namely 375 W. That way the vapour generation is reduced which reduces the bubble diameter. Hence the single-phase natural convection is not negligible any more. The calculation shows a less violent geysering event as before, as expected. After that only a low vapour fraction is generated from the heating area and the vapour does not reach the water surface permanently. Hot vapour plumes therefore move towards the corner area of the heat input where the vapour detaches from the heat input and rises. In consequence a swashing motion from left to right develops which may cause such a bubble plume detachment on the opposite corner region. This way partly a more realistic natural convection develops (see Fig. 5.20).

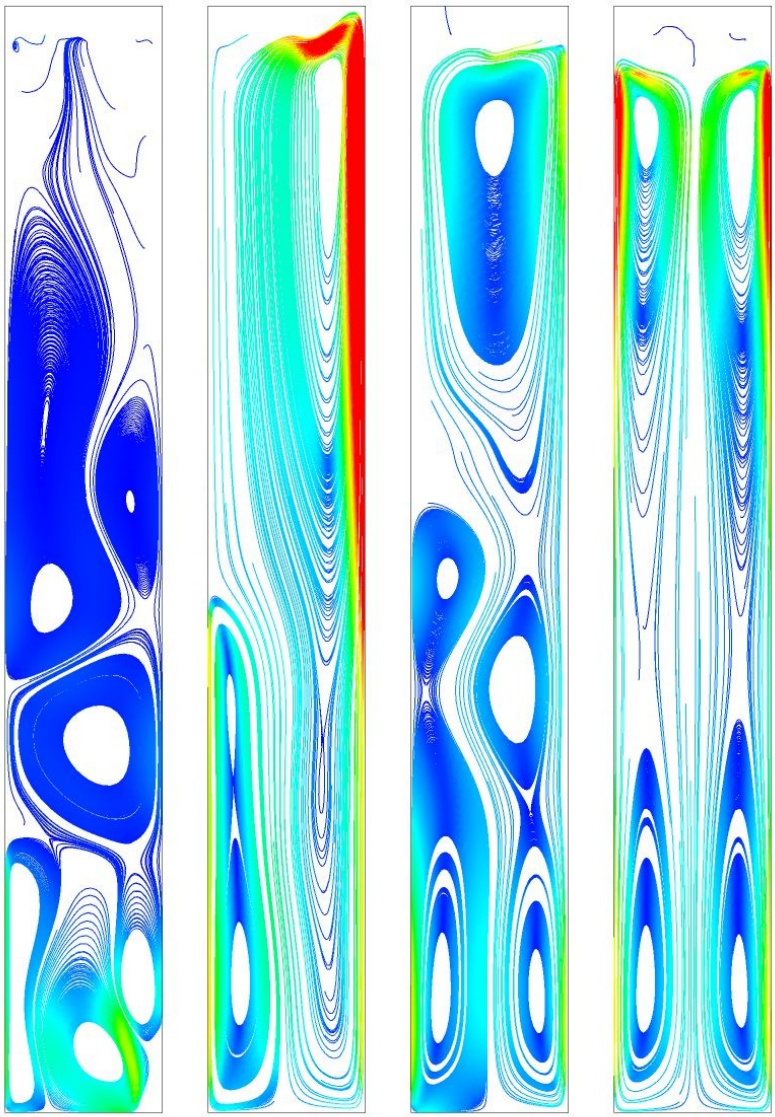

Fig. 5.20: Convection pattern changes towards a stable situation: (a) 20 s (b) 30 s (c) 40 s (d) 347 s

As this became evident early in the simulation an extended transient with a time period of 347 s has been computed. However, when considering the calculated temperatures several small events of geysering happen, but after some calculation time the solution becomes stationary. Considering the monitored temperatures there are several events of dropping temperature, but later the temperatures stabilise (see Fig. 5.21). The monitor point

position, given in the diagram, denotes the distance from the heated surface. Considering the velocity distribution at 347 s, again, the vapour generated at the heated surface reaches the top of the column and a stable double vortex develops. The flow pattern finally develops as it was shown earlier in Fig. 5.2. Considering the temperatures at the end of the long term calculation the highest temperatures are in good agreement with the experiment. The lowest temperatures are about 6 K overestimated.

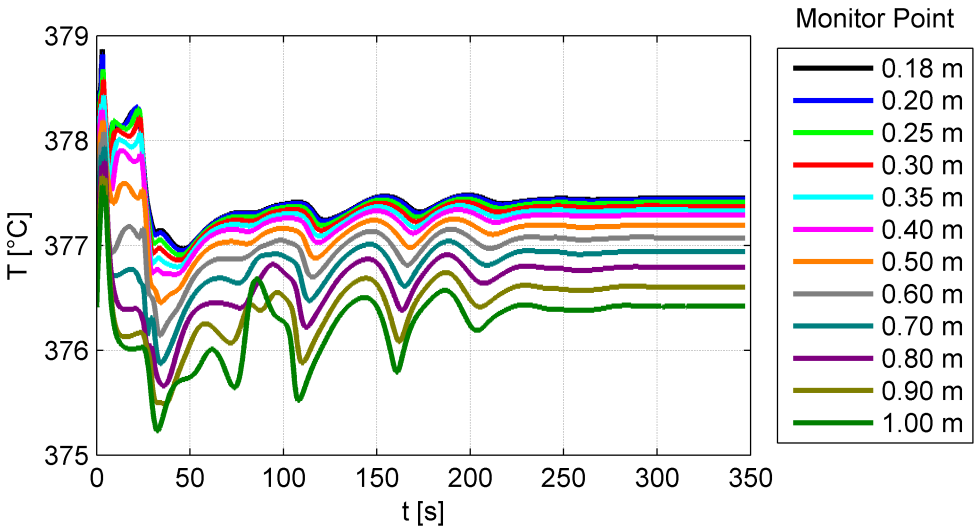

Fig. 5.21: Monitored temperature inside the simulated volume

5.5 3D Simulation with calibrated boiling parameters

So far, the convection pattern was not satisfactory and there are indications that this is caused by the insufficient representation of the heat losses a full 3D Simulation has been performed. Now the domain is half of the volume in the experiment supplemented with a symmetry condition. Therefore the heat losses at the glass plates can be represented as well and the convectional pattern might change. The power input is increased to 3750 W as the water quantity is increased by the factor five. This is therefore corresponding to the 2D simulations with 750 W heat input. The higher input was chosen to quickly evaluate if a re-occurring geysering situation can be achieved. The mesh width is again ~5 mm and now consists of 478819 nodes or 527368 hex-hedral elements which increases the computational effort by far. The behaviour in the beginning of the simulation is comparable to the previously performed 2D simulations.

The natural convection patterns are very similar to the observation in the experiment. Now small counter-rotating vortices are formed inside the volume after the first geysering event. As the geysering event causes an upward movement on one side of the liquid column the pattern is changed towards a dominant vortex, but no symmetrical pattern establishes (see Fig. 5.22). Therefore it is concluded that the convectional pattern is represented well.

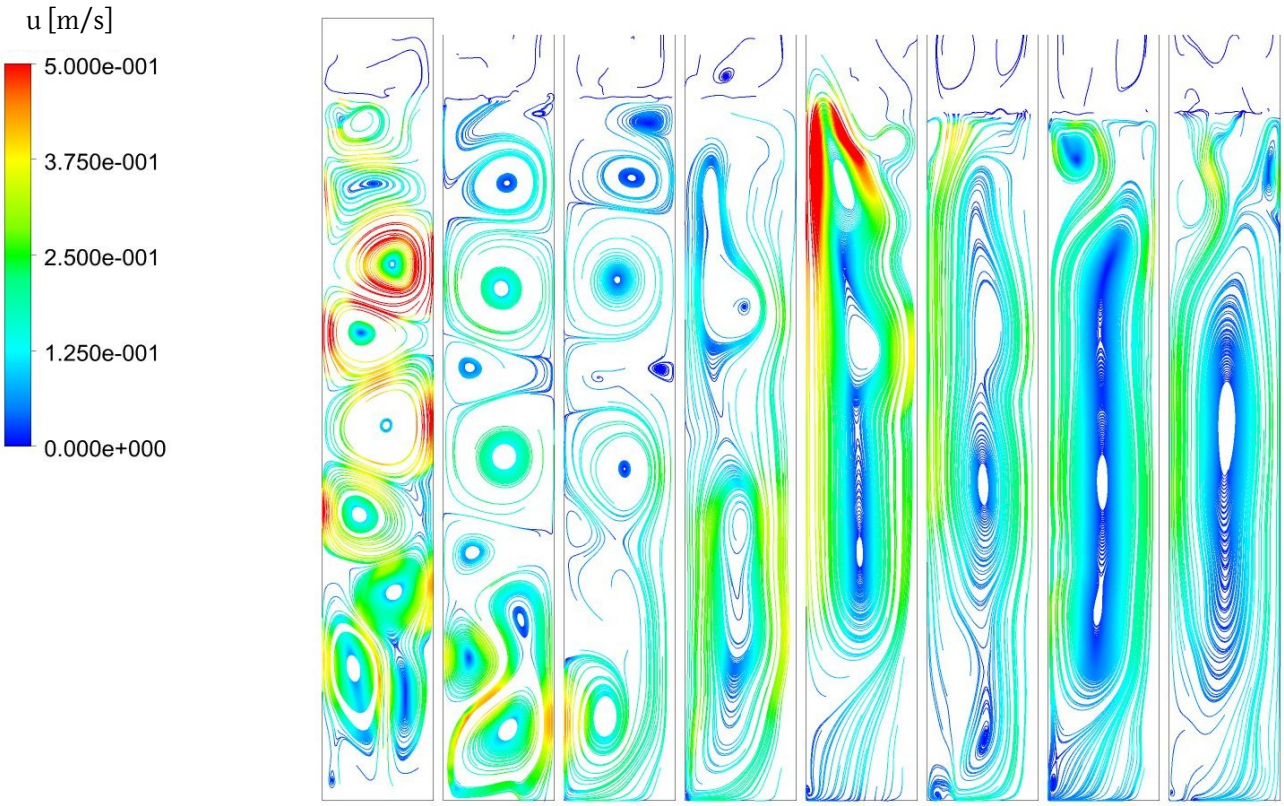

Fig. 5.22: Convection pattern from 5s to 40s in 5s intervals

The heat losses are now in the range of 1000 W which is about ¼ of the heat input (see Fig. 5.23). In comparison the heat losses were twenty times lower than the heat input in the 2D simulations. It is therefore because of these losses that the convections pattern is changed.

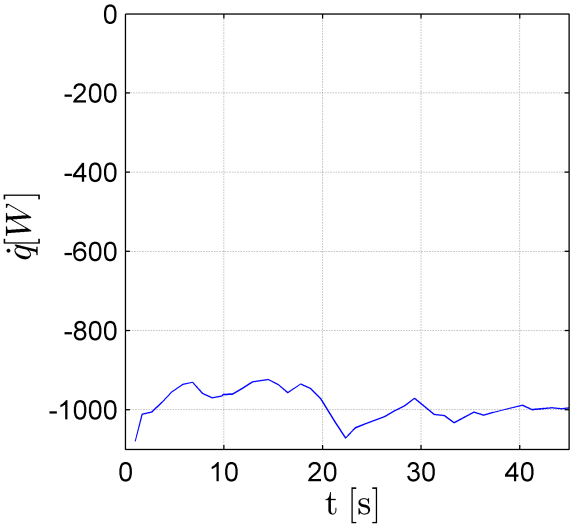

Fig. 5.23: Heat losses in the 3D simulation

The values for the bubble number density, average bubble diameter and vapour fraction are volume averaged. It can be seen, that the 3D calculation shows lower vapour fractions which are very realistic when compared to the experimental data. The values are always below $\alpha = 10\%$ and therefore no concerns arise about coalescence or break-up of bubbles. The volume averaging in the 2D simulations earlier does overestimate the vapour fraction. The bubble diameter varies inside the full range from $d_b = 0.1$ mm up to $d_b = 50$ mm. The peak values are achieved only in short periods of time during re-occuring Geysering events, which are now represented. The bubble number density does as well change in between $n = 75000\ m^{-3}$ and $n = 183270\ m^{-3}$. All these values are summarised in Tab. 5.1.

Tab. 5.1: Minimum, maximum and mean values of d_b, α and n in the 3D flow simulation

		Pos 1	Pos 2	Pos 3	Pos 4	Pos 5
$d_{b,min}$	[mm]	0.1	0.1	0.1	0.1	0.1
$d_{b,max}$	[mm]	50	50	1.6	1.1	1.7
$d_{b,mean}$	[mm]	0.8	1.3	0.2	0.2	0.3
α_{min}	[-]	10^{-9}	10^{-9}	10^{-9}	10^{-9}	10^{-9}
α_{max}	[-]	0.0705	0.0829	0.0287	0.0103	0.0440
α_{mean}	[-]	0.0005	0.0009	0.0005	0.0005	0.0034
n_{min}	[1/m³]	75000	75000	75000	75000	75000
n_{max}	[1/m³]	75010	75100	76510	91740	183270
n_{mean}	[1/m³]	75000	75002	75019	75214	77411

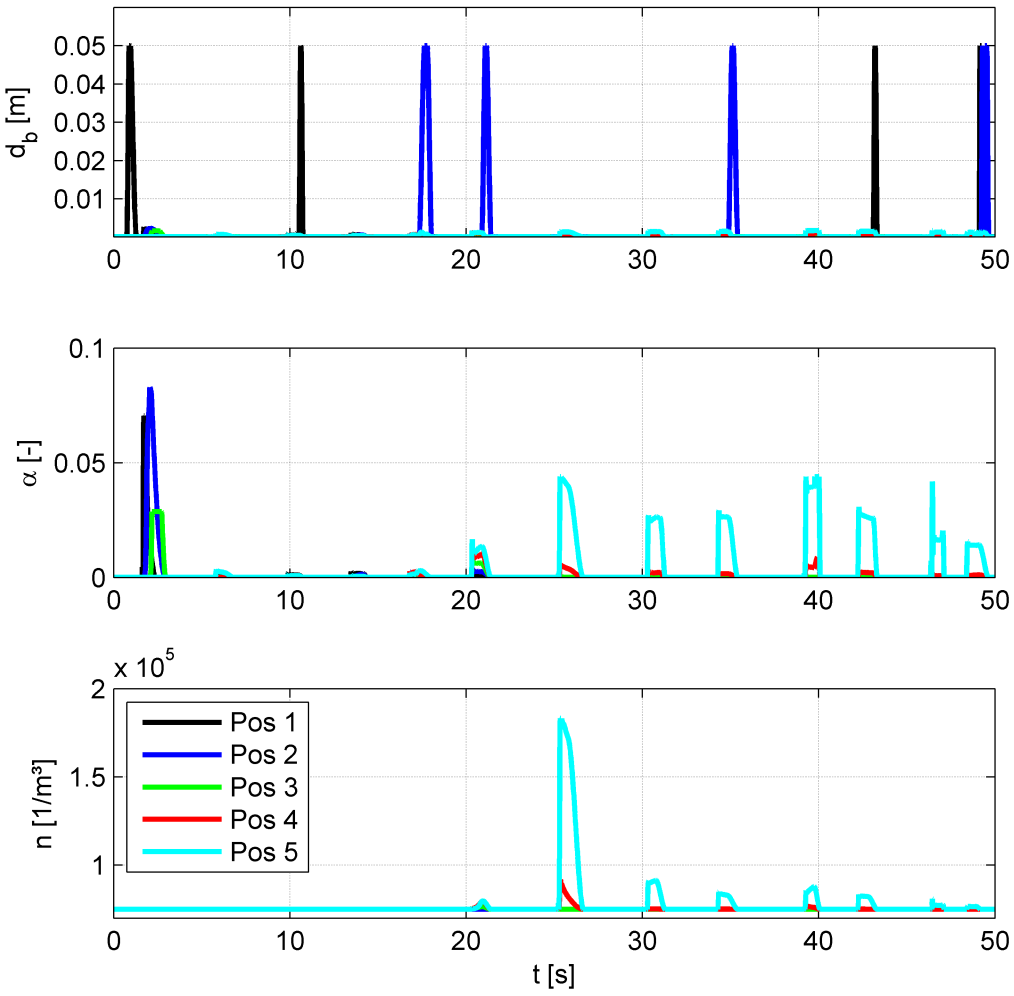

Fig. 5.24: Vapour and bubble quantities of the full 3D flow simulation

Altogether in this flow simulation twelve peaks of the vapour fraction can be counted in the 50 s of calculation when the first peak is dis-considered. The time gaps are not regular, but the intervals do vary only a little. These are shorter intervals of $\Delta t \approx 3.85 \pm 1$ s, than in the experimental set-up the intervals were $\Delta t \approx 137 \pm 101$ s.

The effect of increases in the bubble number density n suppressing an increase in bubble diameter d_b is visible at $t \approx 25$ s. The bubble size increases only up to about d_b =1 mm because of the simultaneous increase of the bubble number density n although the vapour fraction reaches a maximum. During the first five peaks there was no simultaneous bubble number density increase, and there, with comparable vapour fractions, the bubble diameter reached the maximum value of d_b = 50 mm three times. It becomes clear that the geysering events differ in intensity when the maximum vapour fraction is considered (see Fig. 5.25).

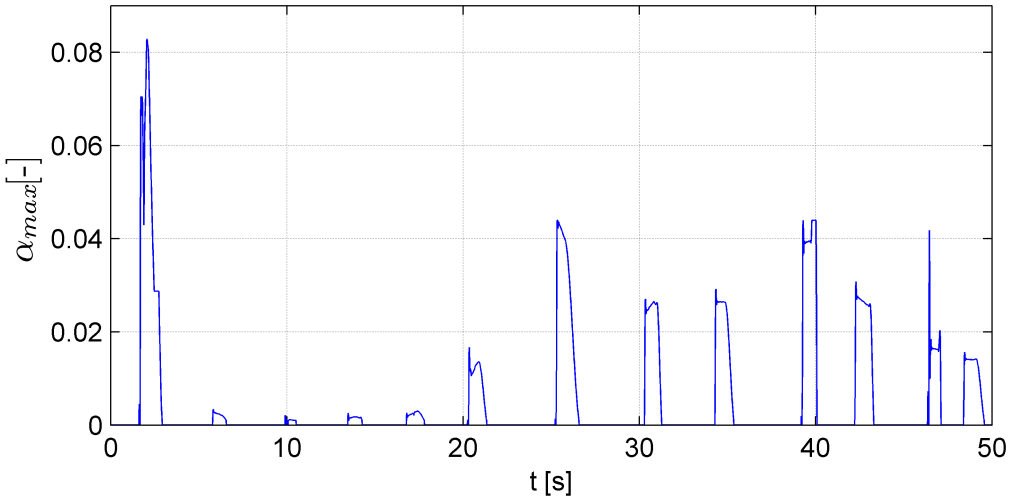

Fig. 5.25: Maximum vapour fraction during the flow simulation

The maximum vapour fractions directly correlate to the increases in the bubble number density in all cases except of the first Geyser, which is caused by the initialisation. That result is expected as only with higher vapour fraction the upward motion is strong enough to cause super-heating, which causes the increases in the bubble number density.

For illustration two image series showing the vapour fraction are shown in Fig. 5.26 and Fig. 5.27. The vapour fraction is shown from the centre plane to the outer wall in equidistant planes. The image series in Fig. 5.26 shows a geysering event as it is expected with this initialisation. It can be seen that there a trailing plume of bubbles instigates the instabilities by supplying additional vapour and pulling hot liquid upwards. This instability corresponds to the peak at about 3 s in Fig. 5.25.

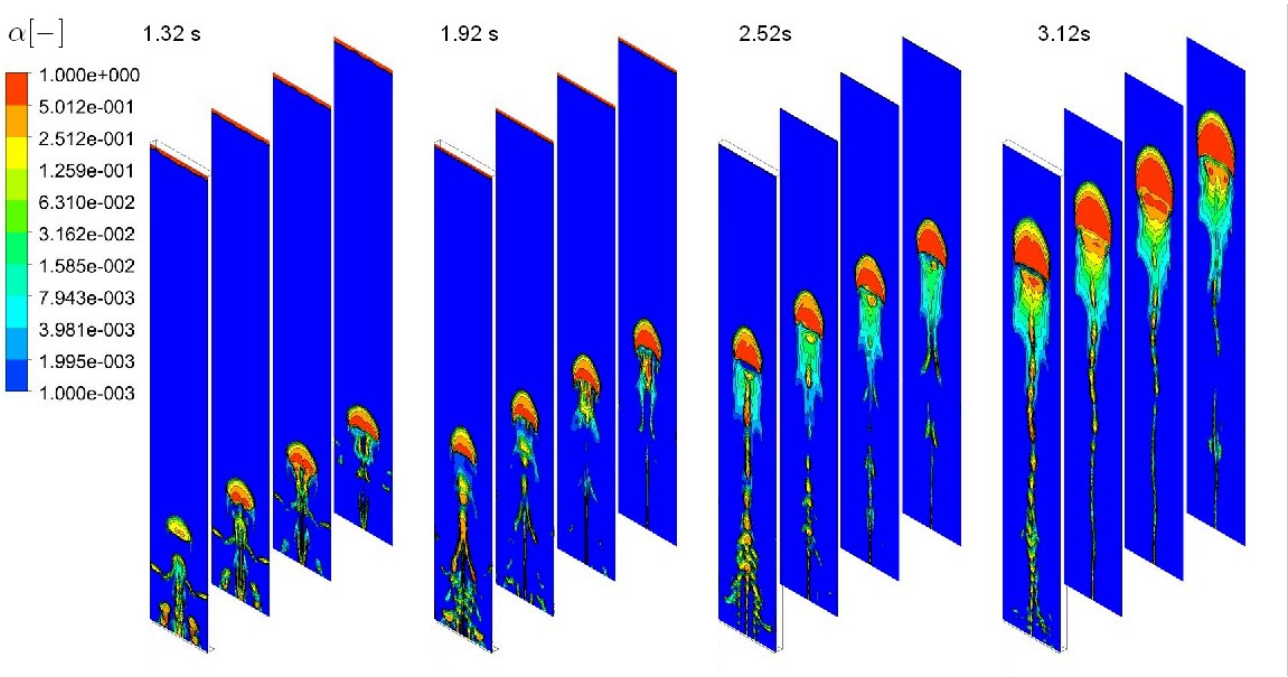

Fig. 5.26: Simulated initial geysering event in the 3D simulation set-up

In Fig. 5.27 a more calm situation is shown during which spontaneously two vapour plumes are evaporated in the bulk volume. These two plumes correspond to the peak at about 20 s in Fig. 5.25.

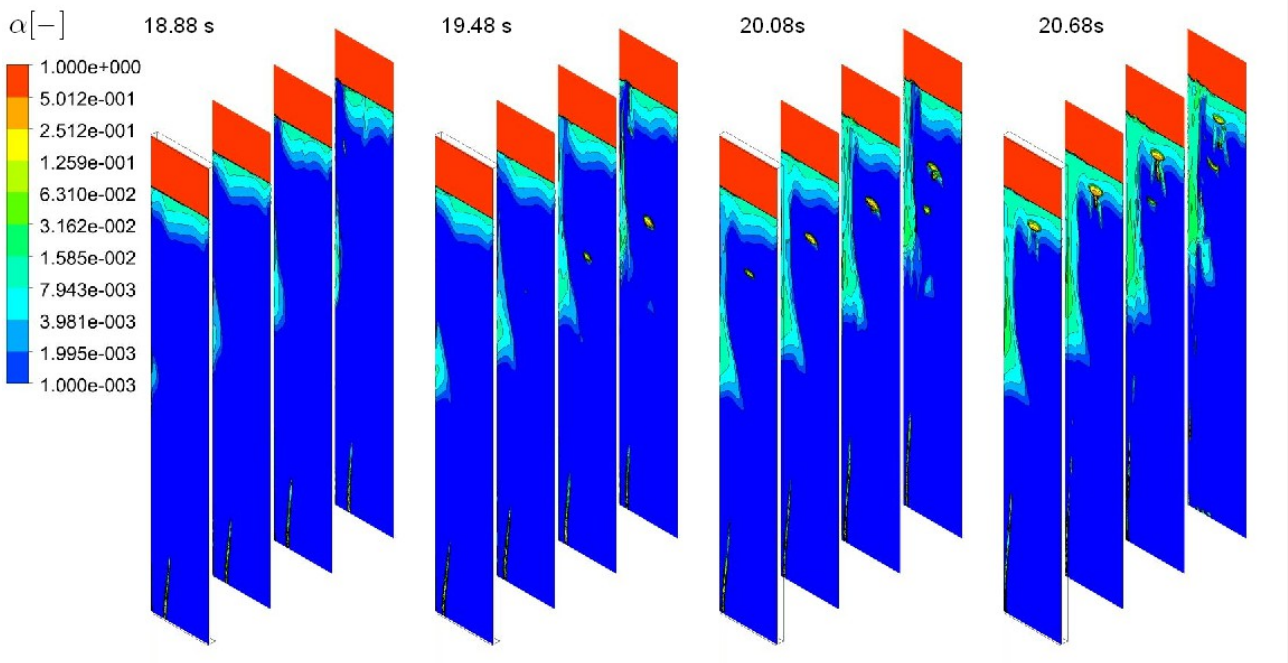

Fig. 5.27: Spontaneous vapour production in the bulk volume during the 3D simulation

5.6 Summary of the computational results

The growth/shrink mechanism and the sudden increase in bubble number density were identified as main mechanisms during the previously shown experiments. Based on this a mechanistic modelling was proposed in chapter 4.3. The computational results, that were obtained by using the presented boiling model, which has been implemented into CFX and running with an Euler-Euler two phase formulation, are able to reproduce the observed mechanisms well. This has been shown by:

- Initial fluctuation of the bubbles' diameter showing the growth/shrink mechanism
- Upon the presence of a hot path monotonous bubble growth
- Geysering event caused by grown bubble drag on the liquid

The experimentally ascertained parameters for the used boiling model did show good agreement with both the bubble sizes and the sudden increase in bubble number density. Further variations of the parameters show that the correct estimation of the parameter *a* should be oriented towards representing the correct average bubble diameter. The sensitivity is relatively low though, as the mean bubble number density as well as the highest expectation value estimated by assuming a log-normal bubble number density distribution show good agreement. The second parameter *b* is well estimated by the expected super-heating inside the liquid. This was successfully measured by the temperature drops that lowered the liquid temperature during geysering instabilities. These temperature drops are represented very similarly in the computational results. The vapour fraction calculation suffers from a dependency on the grid resolution as the heat transfer increases with finer meshing which was determined in the grid study.

The model is, as it was presented in eq. (4.11) eq. (4.12), consists of a function for the bubble number density

$$n = a + e^{b(\bar{T}_l - T_{sat})}$$

and the increased internal bubble pressure.

$$T_{sat} = \frac{B}{A - \log_{10}((p_{amb} + p_{YL})/100[Pa])} - C$$

The parameters that were determined in the experiment and verified by simulations for the test set-up are presented in Tab. 5.2.

Tab. 5.2: Determined model parameters

Parameter	
a	75000
b	7,08

Concerning the flow pattern, the natural convection cannot be captured properly using a 2D cut-out section of the experimental set-up. This is mainly because of no or the too low heat losses at the side-walls and thereby insufficient cooling. This can be seen by the fact that the vapour that is created at the heated surface after some time is always able to directly reach the water surface. Another indicator for the insufficient heat loss is that the lowest liquid water temperature is higher than in the experiment. This way a two-phase convection pattern instead of a mixed convection pattern is present. Thereby a stable double vortex is created with a centred down-flow and up-flow at the side-walls. In consequence, the long-term behaviour is not comparable to what has been observed in the experiment. A decrease of the heat input only temporarily yielded a mixed convection pattern.

The 3D simulation represents the natural convection pattern more realistically. In consequence repeating Geysering events can be identified. The quantities bubble diameter, vapour fraction and bubble number density are represented better than before. The time intervals of the Geyser events are much shorter than the experimentally observed Geysers.

6 Summary and Conclusions

Bulk boiling describes the evaporation of liquid inside the volume. Contrary to the expression pool boiling that is used for boiling processes at heated surfaces in water pools, bulk boiling shall denote boiling processes outside the vicinity of heated surfaces. Bulk boiling is of safety relevance, i.e. in spent fuel pools, but is not yet described satisfactory. The fuel pool cooling system needs active components that are not available in case of a full station blackout As a full station blackout, so far, is a beyond design basis accident (BDBA) which has been out of the safety considerations of nuclear power plants. The accident in March 2011 caused by an earthquake and a tsunami in the Fukushima Daiichi nuclear power plant changed that mindset. The prediction of the boil-off behaviour and in this context the possibility of instabilities like geysering stemming from the evolution of the vapour fractions geometrical shape is of safety relevance.

As passive safety systems are favoured in future reactor types, natural convection as well as two-phase convection has become a focus of interest. Other recent works concerning passive containment cooling systems consider the overall cool-ability of gravity driven systems. In such systems the system is at low pressures and the core is surrounded by boiling water. Whilst boiling instabilities inside a closed reactor pressure vessel may be of no concern the evaporated steam is injected into water pools in which the steam condensates. The effectiveness of such loops determines pressure inside the containment [19][20].

A preceding work by T. Giese [21] has investigated a drainage pipe from the upper reactor cavity of a German nuclear power plant (Neckarwestheim) that is connected to the cooling sump. During a Loss of Cooling Accident (LOCA) evaporated steam is condensed in the containment and the saturated water gathers in the upper reactor cavity. The creation of vapour causes blockage inside the piping. The results of computational fluid dynamics (CFD) calculations that were conducted during Gieses' work were dependent on user input, namely the imposed vapour bubble diameter. So the work by Giese demonstrates, that blockages caused by vapour generation needs to be considered in the piping system.

In summary, bulk boiling is present when liquid becomes super-heated by decreasing pressure. This process can occur very fast and affect large portions of the liquid which is why it can greatly affect the flow, especially during instabilities. Mixing processes as well as convection are consequences of vapour generation inside a volume and may effect the heat transfer mechanisms. Other relevant effects may be instabilities like geysering or flashing and piping blockage that may cause security/safety concerns for facilities. CFD calculations do have the potential to become an general safety analysis tool because the development aims for general

application and therefore increases the safety of existing and future nuclear power plants.

The experiment built and investigated in this work consists of a slender and high water column that is heated with constant temperature at the bottom area. The heater's temperature is above the saturation temperature and a sub-cooled boiling regime is present close to the the heated surface. After the heat-up period a quasi-steady state develops and is investigated. The quasi-steady state is thereby defined by a stable average temperature at all measurement points. The measurements include thermocouples and resistance thermal sensors inside the column, as well as pressure transducers.

Because of the unstable layering natural convection develops inside the container. This convection causes hot portions of water to be shifted upwards. At the same time micro-bubbles of incondensable gases, that were created by the sub-cooled boiling at the heater surface, rise as well. The saturation temperature of the water decreases towards the water surface because of the hydrostatic pressure distribution. Hence the rising hot water plumes become super-heated inside the volume and the micro-bubbles start to grow with evaporation.

The water container is built with large area glass plates at the front and back side. This way observation of the processes is done visually. The bubble behaviour inside the water column is recorded with a digital video camera. The image data is evaluated with suited image processing techniques. This way the bubbles have been detected and their properties are investigated. The bubble sizes are distributed exponentially or if the probability density is considered small bubbles are much more likely to occur. The roundness of the bubbles does deviate from perfect spheres but it is indicated that the deviations are small enough not to be considered further. As the topic is dilute bubbly flow, the vapour fractions are low enough so that the bubble diameter is low as well.

During experiments instabilities occurred, which are commonly known as geysering. Thereby vapour is created inside the volume spontaneously and the induced upward motion does not stop but is fuelled by the hot water that is pulled in the wake of the bubble plume. The instabilities are irregular and cool the water down. The water cool-down is a measure for the previously present super-heating inside the liquid water.

The observed effects were modelled in a way that the developed model is suited to be integrated into simulations using computational fluid dynamics. The base of development was chosen to use the constant bubble number density approach. The developed model expands this concept to a variable bubble number density approach. Two main aspects are emphasised, these are a variable bubble number density and the so-called growth/shrink mechanism. The transient bubble

number density changes over several orders of magnitude, but mostly ranges around a median value. The explanation of the changes are local differences in super-heating that activate a repository of micro-bubbles. The second aspect of the growth/shrink mechanism is due to the micro-bubbles increased internal pressure at mechanical equilibrium. That causes the micro-bubbles to be able to convect into super-heated liquid regions, where they start growing. Their growth, however, not only cools down the liquid, but their own saturation temperature is decreased resulting in lower surface tension forces. This is why the grown bubbles are able to outpace their original surrounding liquid until they become sub-cooled again. The micro-bubbles consist of non-condensible gases and continue to convect further.

The simulation set-up has the same geometrical size as the experiment, but is reduced to a slim 2D slice to reduce the calculation times. It is shown that the model can be calibrated using experimental data. This has been established after five calculations that systematically determined the correlation between measured and calculated key values. The progress of knowledge is shown in Tab. 6.1.

Tab. 6.1: Validation steps for simulations with modelled bubble diameter

No.	*a*	*b*	Conclusion	Comment
01	16680	7.08	Bubble number density changes low, average diameters too high, vapour fraction OK	*a* is determined from the arithmetic average bubble number density and *b* from the detected local super-heating
02	16680	10.64	Bubble number density changes, bubble diameter and vapour fractions very high	*b* is varied arbitrarily
03	16680	3.54	Bubble diameters and vapour fractions OK, but close to no bubble number density changes	*b* is varied arbitrarily
04	75000	7.08	Bubble number density changes, bubble diameter and vapour fractions OK, but long-term stationary behaviour unrealistic	*a* is determined from the highest expectation value of the log-normal number density distribution
05	75000	7.08	Bubble number density changes, bubble diameter and vapour fractions OK, but long-term stationary behaviour unrealistic	Set-up modified with heat losses at the side-walls, which is supposed to influence the flow pattern
6	75000	7.08	Bubble number density changes, bubble diameter and vapour fractions OK, initially more realistic, long-term stationary behaviour unrealistic	Set-up modified with heat losses and lower heat-input at the side-walls, which is supposed to influence the flow pattern

In the 3D flow simulation the validated model shows even better representation of the bubble number density, the bubble diameter and the vapour fraction than in the 2D simulation. Especially the natural convection pattern is more realistic and therefore even re-occurring events of Geysering events are realised. The frequency of these Geysering events is not comparable though. It becomes clear that a minimum amount of vapour is necessary for super-heating, because then the upward motion is strong enough to cause an increase in the bubble number density.

The model does effectively represent the relevant mechanisms that were observed in the experiment and can be integrated easily into available simulation systems. The parameters of the model are calibrated for the set-up. Both are of descriptive nature, as the parameter a determines the right representation of the average bubble diameters and b depends on the expected super-heating inside the fluid volume. Both can be estimated from experimental investigations of a respective problems. Usage of the model will determine a reasonable range of the parameters a and b and further decrease the dependence on user input. The user input, however, is still necessary but the descriptive nature of the model facilitates the process.

Bibliography

[1] VDI-Wärmeatlas, Springer, Berlin Heidelberg, 2006, ISBN 978-3-540-25503-1

[2] Herwig, H., Kautz, C.H., Technische Thermodynamik, Pearson Studium, München, 2007

[3] Ahmad, M., Casey, M. and Sürken, N., Experimental assessment of droplet impact erosion resistance of steam turbine blade materials, Wear, pp. 1605 - 1618, 2009

[4] Massoud, M., Engineering Thermofluids, Spinger, Berlin Heidelberg, 2005

[5] Sanaye, S. and Hajabdollahi, H., Multi-objective optimization of shell and tube heat exchangers, Applied Thermal Engineering, pp. 1937 - 1945, 2010

[6] Deev, V.I., Oo, H.L., Kharitonov, V.S., Kutsenko, K.V. and Lavrukhin, A.A., Critical heat flux modeling in water pool boiling during power transients, International Journal of Heat and Mass Transfer, pp. 3780 - 3787, 2007

[7] Lamarsh, J.R. and Barrata, A.J., Introduction to Nuclear Engineering, Prentice-Hall, Inc., Upper Saddle River, New Jersey 07458, 2001

[8] Nukiyama, S., The maximum and minimum values of the heat Q transmitted from metal to boiling water under atmospheric pressure, J. Jap. Soc. Mech. Eng. 37 (1934) 367–374, engl. Translation in Int. J. Heat Mass Transfer 9 (1966), pp. 1419–1433, 1934 (1966)

[9] Qi, Y., Klausner, J.F. and Mei, R., Role of surface structure in heterogeneous nucleation, International Journal of Heat and Mass Transfer, pp. 3097 - 3107, 2004

[10] Hibiki, T. and Ishii, M., Active nucleation site density in boiling systems, International Journal of Heat and Mass Transfer, pp. 2587-2601, 2002

[11] Das, M.K. and Kishor, N., Adaptive fuzzy moedl identification to predict the heat transfer coefficient in pool boiling of distilled water, Expert Systems with Applications, pp. 1142 - 1154, 2009

[12] Wölk, J., Strey, R., Heath, C. H. and Wyslouzil, B. E., Empirical function for homogeneous water nucleation rates, Journal of Chemical Physics, pp. 4954-4960, 2002

[13] Miller, R. C., Anderson, R. J., Kassner, Jr., J. L. and Hagen, D. E., Homogeneous Nucleation Rate Measurements for Water over a Wide Range of Temperature and Nucleation Rate, Journal of Chemical Physics, pp. 3204-3211, 1983

[14] Kerminen, V.-M. and Kulmala, M., Analytical formulae connecting the "real" and the "apparent" nucleation rate and the nuclei number concentration for atmospheric nucleation events, Aerosol Science, pp. 609 - 622, 2002

[15] Lu, X., Watson, A., Gorin, A.V. and Deans, J., Experimental investigation and numerical modelling of transient two-phase flow in a geysering geothermal well, Geothermics, pp. 409 - 427, 2006

[16] Chexal, B., Pal Katra, S., Horowitz, J.S. and Healzer, J.M., Boiling water reactor fuel heatup during loss of coolant while refueling, Nuclear Engineering and Design, pp. 121 - 126, 1993

[17] Leyer, S., Maisberger, F., Herbst, V., Doll, M., Wich, M. and Wagner, T., Status of the full scale component testing of the KERENA Emergency Condenser and Containment Cooling Condenser, Proceedings of the ICAPP '10,June 13-17,San Diego, CA, USA,2010

[18] Krepper, E., Koncar, B. and Egorov, Y., CFD modelling of subcooled boiling - Concept, validation and application to fuel assembly design, , pp. 716 - 731, 2007

[19] Paladino, D., Auban, O., Huggenberger, M. and Dreier, J., A PANDA integral test on the effect of light gas on a Passive Containment Cooling System (PCCS), Nuclear Engineering and Design, pp. 4551 - 4561, 2011

[20] Paladino, D. and Dreier, J., Passive Containment Cooling System (PCCS) , Nuclear Engineering and Design, pp. 212 - 220, 2012

[21] Giese, T., Numerische und experimentelle Untersuchung von gravitationsgetriebenen Zweiphasenströmungen durch Rohrleitungen, Dissertation, Institut für Kernenergetik und Energiesysteme, Universität Stuttgart, 2003

[22] Chabot, J., Farag, H., and de Lasa, H., Fluid dynamics in bubble columns at elevated temperature modelling and investigation with refractive fiber optic sensors, Chemical Engineering Journal, pp. 105-113, 1998

[23] Chaumat, H., Billet-Duquenne, A.M., Augier, F., Mathieu, C., and Delmas, H., On the reliability of an optical fibre probe in bubble column under industrial relevant operating conditions, Experimental Thermal and Fluid Science, pp. 495-504, 2007

[24] Prasser, H.-M., Scholz, D., and Zippe, C., Bubble size measurement using wire-mesh sensors, Flow Measurement and Instrumentation, pp. 299-312, 2001

[25] Prasser., H.-M., Misawa, M., and Tiseanu, I., Comparison between wire-mesh sensor and ultra-fast X-ray tomograph for an air-water flow in a vertical pipe, Flow Measurement and Instrumentation, pp. 73-83, 2005

[26] Pietruske, H., and Prasser, H.-M., Wire-mesh sensors for high-resolving two-phase flow studies at high pressures and temperatures, Flow Measurement and Instrumentation, pp. 87-94, 2007

[27] Stürzel, T., Bieberle, M., Laurien, E., Hampel, U., Barthel, F., Menz, H.-J., and Mayer, H.-G., Experimental facility for two- and three-dimensional ultrafast electron beam x-ray computed tomography, Review of Scientific Instruments, pp. , 2011

[28] Manera, A., Ozar, B., Paranjape, S., Ishii, M., and Prasser, H.-M., Comparison between wire-mesh sensors and conductive needle-probes for measurements of two-phase flow parameters, Nuclear Engineering and Design, pp. 1718-1724, 2009

[29] Gerardi, C., Buongiorno, J., Hu, L.-W., and McKrell, T., Study of bubble growth in water pool boiling through synchronized, infrared thermometry and high-speed video, International Journal of Heat and Mass Transfer, pp. 4185-4192,

[30] Rong, S., Ye, M., Mamoru, I. and Michitsugu, M., Photographic study of bubble behaviours forced convection subcooled boiling, International Journal of Heat and Mass Transfer, pp. 3659-3667, 2004

[31] Zaruba, A., Krepper, E., Prasser, H. M. and Reddy Vanga, B. N., Experimental Study on Bubble Motion in a Rectangular Bubble Column using High-Speed Video Observations, Flow Measurement and Instrumentation, pp. 277-287, 2005

[32] Mishima, K., and Hibiki, T., Development of high-frame-rate neutron radiography and quantitative measurement method for multiphase flow research, Nuclear Engineering and Design, pp. 183-201, 1198

[33] Luke, A., and Cheng, D.-C., High speed video recording of bubble formation with pool boiling, International Journal of Thermal Sciences, pp. 310-320, 2006

[34] Maurus, R., Ilchenko, V., and Sattelmayer, T., Automated high-speed video analysis of the bubble dynamics in subcooled flow boiling, International Journal of Heat and Fluid Flow, pp. 149-158, 2004

[35] Guo, F., Yang, Y., Chen, B., and Guo, L., A novel multi-scale edge detection technique based on wavelet analysis with application in multiphase flows, Powder Technology, pp. 171-177, 2010

[36] Canny, J., A Computational Approach to Edge Detection, IEEE Transactions on Pattern Analysis and Machine Intelligence, pp. , 1986

[37] Daubner, M., Janssens-Meanhout, G., Knebel J.U., Technische Beschreibung der Testanlage SUCOT zur Untersuchung einer Wasser/Wasserdampf Zweiphasenströmung, FZKA 6683, 2002

[38] Okawa, T., Yamagoe, Y. and Ahmadi, R., Void Fraction Evolution in Subcooled Flow Boiling under Low-Pressure and Low-Flowrate Condition, The 14th Topical Meeting on Nuclear Reactor Thermohydraulics, NURETH 14,,Ontario, Canada,2011

[39] Volmer, M. and Weber, A., Keimbildung in übersättigten Gebilden, Zeitschrift für physikalische Chemie, pp. 277-301, 1926

[40] Farkas, L., Keimbildungsgeschwindigkeit in übersättigten Dämpfen, Zeitschrift für physikalische Chemie, pp. 236-242, 1927

[41] Becker, R. and Döring, W., Kinetische Behandlung der Keimbildung in übersättigten Dämpfen, Annalen der Physik, pp. 719-752, 1935

[42] Volmer, M., Kinetik der Phasenbildung, Theodor Steinkopf, Dresden/Leipzig, 1939

[43] Zeldovich, J.B., Theory of new phase formation: cavitation, Journal of experimental and theoretical physics (USSR), pp. 525-538, 1942

[44] ter Horst, Bedeaux and Kjelstrup, The role of temperature in nucleation processes, J. Chem. Phys., pp. 054703, 2011

[45] Skripov, V. P., Metastable Liquids, J. Wiley, New York, 1974

[46] Kashchiev, D., Nucleation, Butterworth-Heinemann, Oxford [et al], 2000

[47] Blander, M., Hengstenberg, D. and Katz, J. L., Bubble Nucleation in n-Pentane, n-Hexane, n-Pentane + Hexadecane Mixtures, and Water, Journal of Physical Chemistry, pp. 3613-3619, 1971

[48] Viisanen, Y., Strey, R. and Reiss, H., Homogeneous Nucleation Rates for Water, Journal of Chemical Physics, pp. 4680-4692, 1993

[49] Ishii, M., Thermo-Fluid Dynamics Theory of Two-Phase Flow, Eyrolles, Paris, 1975

[50] Nigmatulin, R.I., Spatial Averaging in the Mechanics of Heterogeneous and Dispersed Systems, Int. J. Multiphase Flow, pp. 353-385, 1979

[51] Drew, D.A., Mathematical Modeling of Two-Phase Flows, Ann. Rev. Fluid Mech., pp. 261-291, 1983

[52] Sokolichin, A., Eigenberger, G., Lapin, A., and Lübbert, A., Dynamic numerical simulation of gas-liquid two-phase flows - Euler/Euler versus Euler/Lagrange, Chemical Engineering Science, pp. 611-626, 1997

[53] Farzpourmachiani, A. Shams, M., Shadaram, A. and Azidehak, F., Eulerian-Lagrangian 3-D simulations of unsteady two-phase gas-liquid flow in a rectangular column by considering bubble interactions, International Journal of Non-Linear Mechanics, pp. 1049 - 1056, 2011

[54] Kumzerova, E. Y. and Schmidt, A. A., Numerical Simulation of Effect of Bubble Nucleation on Flashing Flow Structure, ,,Yokohama, Japan,2004

[55] Heusch, M., Thermodynamische Untersuchungen der Kavitation in Bremsflüssigkeiten und deren numerische Simulation, Dissertation, , , 2006

[56] Laurien, E., Influence of the Model Bubble Diameter on Three-Dimensional Numerical Simulations of Thermal Cavitation in Pipe Elbows, ,,,2004

[57] Asher, M.I. et al., Parameter Sensitivity Study of Boiling and Two-Phase Flow Models in Computational Thermal Hydraulics, The 14th International Topical Meeting on Nuclear Reactor Thermohydraulics, NURETH-14,September 25-30,Toronto, Ontario, Canada,2011

[58] Tolubinsky, V.I. and Konstanczuk, D.M., Vapour Bubbles Growth Rate and Heat Transfer Intensity at Subcooled Water Boiling, Proc. 4th International Heat Transfer Conference, Vol.5,,,1970

[59] Tu, J.Y. and Yeoh G.H., On numerical modelling of low-pressure subcooled boiling flows, , pp. 1197 - 1209, 2002

[60] Anglart, H. and Nylund, O., CFD application to prediction of void distribution in two-phase bubbly flows in rod bundles, , pp. 81-98, 1996

[61] Zeitoun, O. and Shoukri, M., Bubble behavior and mean diameter in subcooled flow boiling, , pp. 110-116, 1996

[62] Yeoh, G.H., Tu J.Y. and Li, Y., On void fraction distribution during two-phase boiling flow instability, , pp. 413 - 417, 2004

[63] Van Sint Annaland, M., N.G. Deen and Kuipers, J.A.M., Multi-Level Modelling of Dispersed Gas-Liquid Multi-Phase Flows in: Sommerfeld, M.(eds.), Bubbly Flows, Springer, Berlin Heidelberg New York, pp. 139 - 157, 2004

[64] Bothe, D. et al., Direct numerical simulation of mass transfer between rising gas bubbles and water in: Sommerfeld, M.(eds.), Bubbly Flows, Springer, Berlin Heidelberg New York, pp. 159 - 174, 2004

[65] Krepper, E., Lucas, D., Frank, T., Prasser, H.-M. and Zwart, Ph.J., The inhomogeneous MUSIG model for the simulation of polydispersed flows, Nuclear Engineering and Design, pp. 1690 - 1702, 2008

[66] Krepper, E., Beyer, M., Lucas, D. and Schmidtke, M., A population balance approach considering heat and mass transfer - Experiments and CFD simulations, Nuclear Engineering and Design, pp. 2889 - 2897, 2011

[67] Hibiki, T. and Ishii, M., Development of one-group interfacial area transport equation in bubbly flow systems, International Journal of Heat and Mass Transfer, pp. 2351 - 2372, 2002

[68] Morel, Ch., Ruyer, P., Seiler, N. and Laviéville, J.M., Comparison of several models for multi-size bubbly flows on an adiabatic experiment, International Journal of Multiphase Flow, pp. 25 - 39, 2010

[69] Mitrovic, J. and Stephan, K., Gleichgewichtsradien von Dampfblasen und Flüssigkeitstropfen, Wärme- und Stoffübertragung, pp. 171-176, 1980

[70] Ranz, W. E., Marshall, W. R., Evaporation from Drops, Chemical Engineering Process, pp. 141-146; 173-180, 1952

[71] Hughmark, G.A., Mass and heat transfer from rigid spheres, AIChE Journal, pp. 1219-1221, 1967

[72] Ansys CFX-Solver Modeling Guide Release. 12, Ansys, Inc., Southpointe, 275 Technology Drive, Canonsburg, PA 15317, USA, 2009

[73] Ansari, M.R. and Nimvari, M.E., Bubble viscosity effect on internal circulation within the bubble rising due to buoyancy using the level set method, Annals of Nuclear Energy, pp. 2770 - 2778, 2011

[74] Gaudlitz, D., Numerische Untersuchung des Aufstiegsverhaltens von Gasblasen in Flüssigkeiten, Dissertation, , , 2008

[75] Chen, R.H., Tian, W.X., Su, S.H., Qiu, S.Z., Ishiwatari, Y. and Oka, Y., Numerical investigation on coalescence of bubble pairs rising in a stagnant fluid, , pp. 5055-5063, 2011

[76] Ramirez-Munoz, J., Salinas-Rodriguez, E., Soria, A. and Gama-Goicochea, A., Hydrodynamic interaction on large-Reynolds-number aligned bubbles: Drag effects, , pp. 2371-2377, 2011

[77] Roghair, I., Lau, Y.M., Deen, N.G., Slagter, H.M., Baltussen, M.W., Van Sint Annaland, M. and Kuipers, J.A.M., On the drag force of bubbles in bubble swarms at intermediate and high Reynolds numbers, , pp. 3204-3211, 2011

[78] Lau, Y.M., Roghair, I., Deen, N.G., van Sint Annaland, M. and Kuipers, J.A.M., Numerical investigation of the drag closure for bubbles in bubble swarms, , pp. 3309-3316, 2011

[79] Göz, M.F., Sommerfeld, M., Analysis of bubble interactions in bidisperse bubble swarms by direct numerical simulation in: Sommerfeld, M.(eds.), Bubbly Flows, Springer, Berlin Heidelberg New York, pp. 175 - 190, 2004

[80] Lehr, F. and Mewes, D., A transport equation for the interfacial area in bubble columns using a population balance approach in: Sommerfeld, M.(eds.), Bubbly Flows, Springer, Berlin Heidelberg New York, pp. 203 - 216, 2004

[81] Rodriguez, I., Castro, J., Perez-Sagarra, C.D. and Aliva, A., Unsteady numerical simulation of the cooling process of vertical storage tanks under laminar natural convection, , pp. 708 - 721, 2009

[82] Gahndi, M.S., Sathe, M.J., Joshi, J.B. and Vijayan, P.K., Two phase natural convection: CFD Simulations and PIV measurements, , pp. 3152 - 3171, 2011

[83] Espinosa-Paredes, G., Verma, S.P., Vasquez-Rodriguez, A. and Nunez-Carrera, A., Mass flow rate sensivity and uncertainty analysis in natural circulation boiling water reactor core from Monte Carlo simulations, Nuclear Engineering and Design, pp. 1050 - 1062, 2010

[84] Kozmenkov, Y., Rohde, U. and Manera, A., Validation of the RELAP5 code for the modeling of flashing-induced instabilities under natural-circulation conditions using experimental data from the CIRCUS test facility, Nuclear Engineering and Design, pp. 168 - 175, 2012

[85] Shin, B. S., and Chang, S.H., Experimental study on the effect of angles and positions of mixing vanes on CHF in a 2x2 rod bundle with working fluid R-134a, Nuclear Engineering and Design, pp. 1749-1759, 2005

[86] Shin, B.S., and Chang, S.H., CHF experiment and CFD analysis in a 2x3 rod bundle with mixing vane, Nuclear Engineering and Design, pp. 899-912, 2009

[87] Le Corre, J.-M., Yao, S.-C., and Amon, C.H., A mechanistic model of critical heat flux under subcooled flow boiling conditions for application to one- and three-dimensional computer codes, Nuclear Engineering and Design, pp. 235-244, 2010

[88] Le Corre, J.-M., Yao, S.-C., and Amon, C.H., Two-phase flow regimes and mechanisms of critical heat flux under subcooled flow boiling conditions, Nuclear Engineering and Design, pp. 245-251, 2010

[89] Chandraker, D.K., Vijayan, P.K., Saha, D., and Sinha, R.K., Investigation on the characteristic of CHF in various flow pattern regimes based on look-up table data, Nuclear Engineering and Design, pp. 170-177, 2008

[90] C.E. Brennen, Cavitation and Bubble Dynamics, Oxford University Press, New York, Oxford, 1995

[91] Peterson, F.B., Danel, F., Keller, A.P., and Lecoffre, Y., Comparative measurements of bubble and particulate spectra by three optical methods, ,,,1975

[92] Katz, J., Determination of solid nuclei and bubble distributions in water by holography, Eng. and Appl. Sci. Div. Rep., Cal. Inst. of Tech., No. 183-3, 1978

[93] Gates, E.M., and Bacon, J., Determination of cavitation nuclei distribution by holography, J. Ship Res., pp. 29-31, 1978

[94] Properetti, A. and Plesset, M.S., Vapour-bubble growth in a superheated liquid, J. Fluid. Mech., pp. 349-368, 1978

[95] Norm DIN EN 60751

[96] Agilent 34970A/34972A Data Acquisition/Switch Unit User's Guide, Agilent Technologies, Inc., 900 S. Taft Ave.Loveland, CO 80537 USA, 2009 - 2012

[97] Norm IEC 584-3

[98] MATLAB R2009a Image Processing Toolbox User's Guide, The MathWorks, Inc., 3 Apple Hill DriveNatick, MA 01760-2098, 2009

[99] Soille, P., Morphological Image Analysis - Principles and Applications - Second Edition, Springer-Verlag, Berlin Heidelberg New York, 2004

[100] Russ, J.C., The Image Processing Handbook, CRC Press LLC, Boca Raton London New York Washington, D.C., 2002

[101] Clift, R., Grace, J. R. and Weber, M. E., Bubbles, drops, and particles, Acad. Press, New York, 1978

[102] Nyquist, H., Certain Topics in Telegraph Transmission Theory, AIEE Trans., pp. 617-644, 1928

[103] Laurien, E. and Oertel, H., Numerische Strömungsmechanik, Vieweg+Teubner Verlag / Springer Fachmedien Wiesbaden GmbH, Wiesbaden, 2011

[104] Pellicer, J., Garcia-Morales, V., and Hernandez, M.J., On the demonstration of the Young-Laplace equation in introductory physics courses, Phys. Educ., pp. , 2000

[105] Menter, F., CFD Best Practice Guidelines for CFD Code Validation for Reactor-Safety Applications, ECORA Contract No FIKS-CT, pp. Evol - Ecora - D 01, 2001

Appendix A

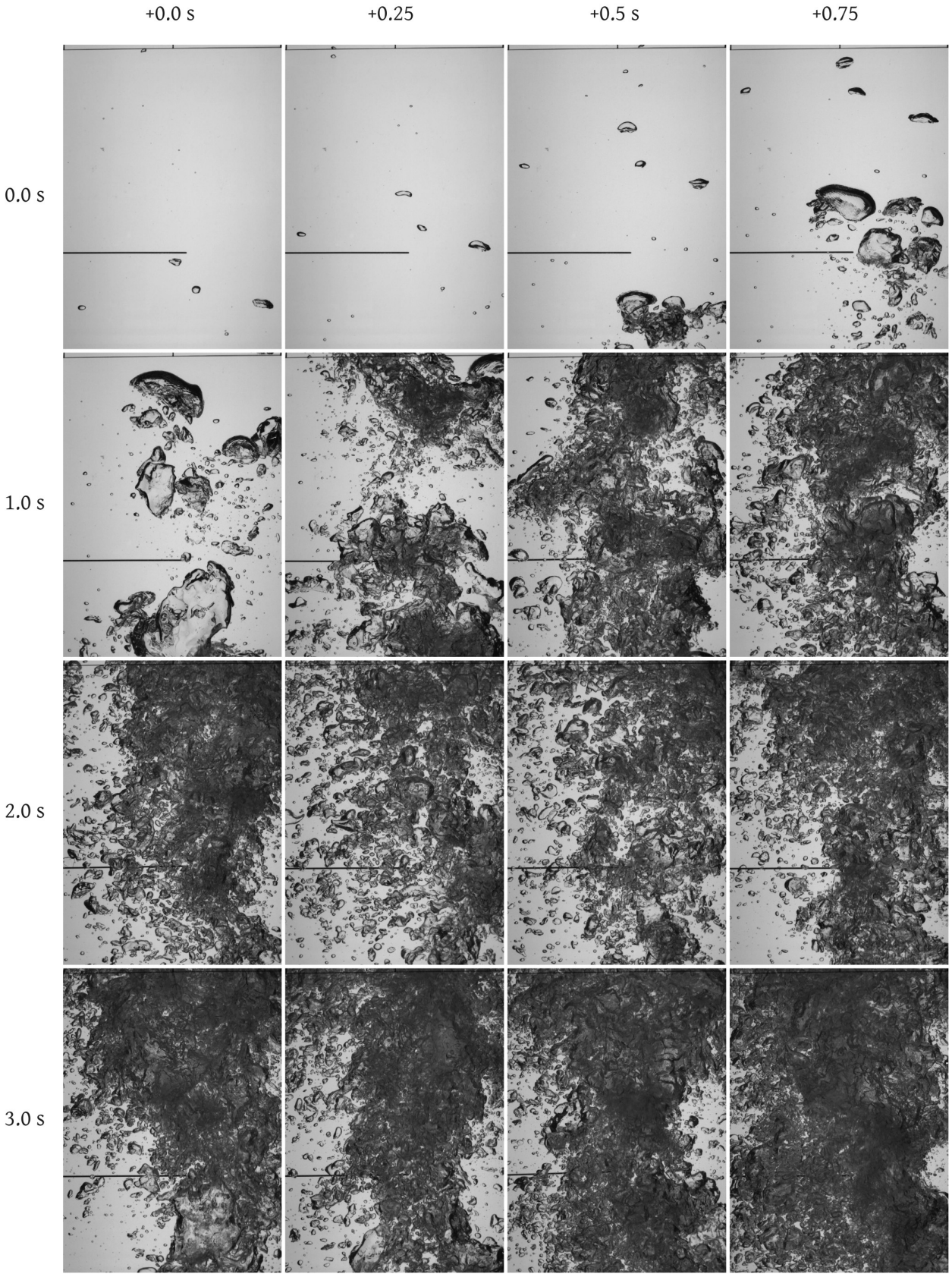

Fig. 6.1: Detailed image series of a geysering event (part 1)

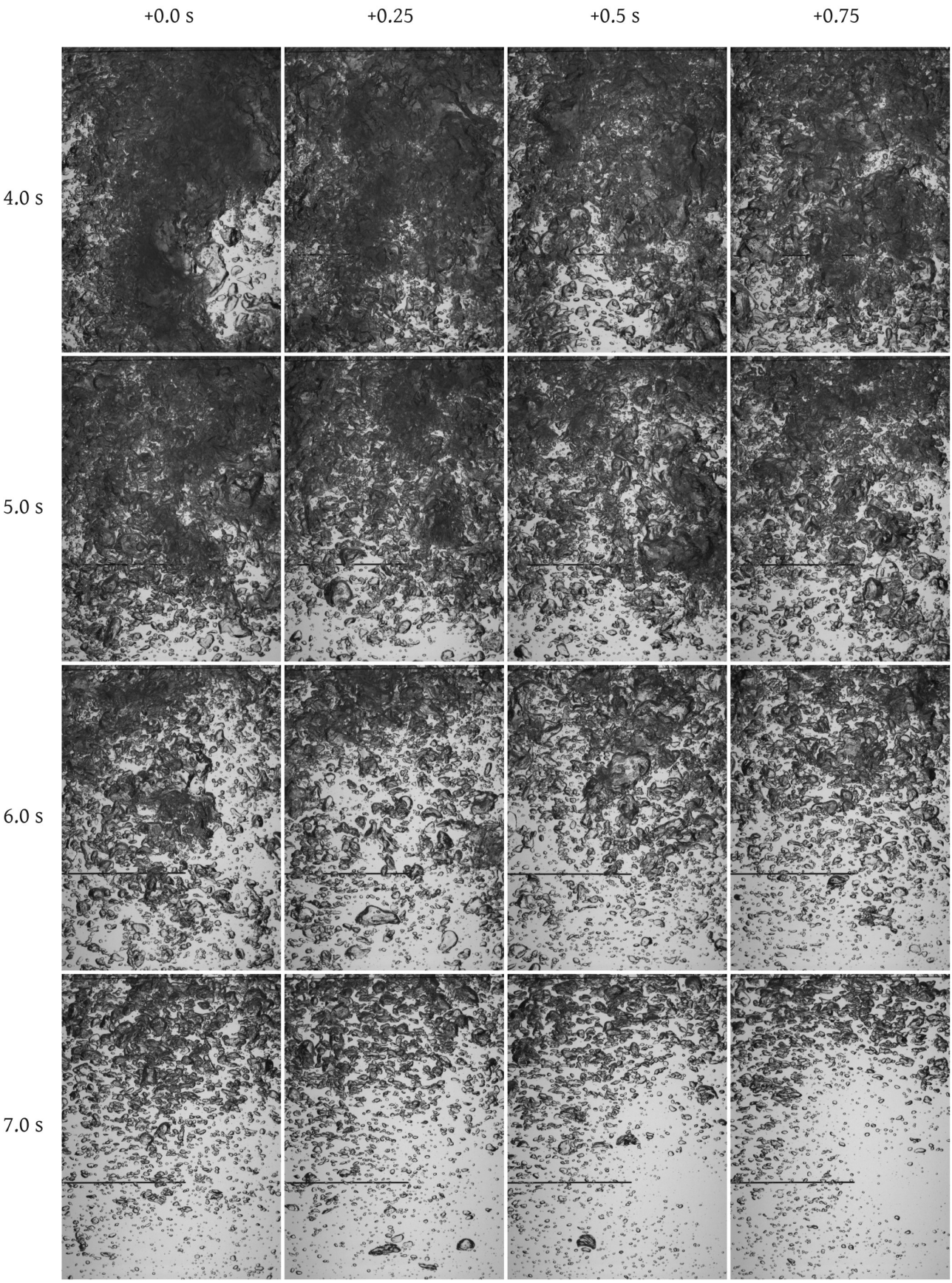

Fig. 6.2: Detailed image series of a geysering event (part 2)